An Investigation of 2D/1D Approximations to the 3D Boltzmann Transport Equation

by

Blake W. Kelley

A dissertation submitted in partial fulfillment
of the requirements for the degree of
Doctor of Philosophy
(Nuclear Engineering and Radiological Sciences and Scientific Computing)
in the University of Michigan
2015

Doctoral Committee:

Professor Thomas J. Downar, Co-Chair
Professor Edward W. Larsen, Co-Chair
Professor William R. Martin
Professor John C. Schotland

For my wife, Maddie Kelley, for her endless patience and support

For my mother, Roxanne Kelley, for her encouragement through all my life

For my father, Tim Kelley, whose pride is felt even after his passing

Acknowledgments

First and foremost, I would like to thank Prof. Edward Larsen and Prof. Thomas Downar for their support and guidance throughout the process of earning my PhD. Both academically and personally, they have been there for me every step of the way. I would also like to thank the other members of the MPACT development team, in particular, Dr. Ben Collins, Dan Jabaay, Dr. Brendan Kochunas, and Dr. Shane Stimpson; their work in this code made my work possible. Finally, I would like to acknowledge the CASL program for the funding provided for my graduate education and this work.

Table of Contents

List of Figures

List of Tables

Abstract

A new class of "2D/1D" approximations is proposed for the 3D linear Boltzmann equation. These approximate equations preserve the exact transport physics in the radial directions x and y and employ approximate diffusion physics in the axial direction z. Thus, the 2D/1D equations are more accurate approximations of the 3D Boltzmann equation than the conventional 3D diffusion equation. The 2D/1D equations can be systematically discretized, to yield accurate simulation methods for 3D reactor core problems. The resulting solutions are more accurate than 3D diffusion solutions, and less expensive to generate than standard 3D transport solutions. In this work, we (i) introduce several new "2D/1D equations" as accurate approximations to the 3D Boltzmann transport equation, (ii) show that the 2D/1D equations have certain desirable properties, (iii) systematically discretize the equations, and (iv) derive a stable iteration scheme for solving the discrete system of equations. Additionally, we give numerical results that confirm the theoretical predictions of accuracy and iterative stability.

Chapter 1

Introduction and History

The term "2D/1D" has been used to describe recently-developed computational methods for solving 3D whole-core neutronics problems in which the (1D) axial and (2D) radial derivative terms are approximated differently. These methods were originally proposed and implemented by two groups in Korea during 2002-2007 [1–11]. One group, located at KAIST (N.Z. Cho, G.S. Lee, C.J. Park, and colleagues), developed the "2D/1D Fusion" method for the CRX code [1, 3–5, 8, 9]. In this method, the 3D Boltzmann transport equation is solved by discretizing the radial derivative terms on a "fine" radial grid and the axial derivative term on a "coarse" radial grid. The other group, located at at KAERI (J.Y. Cho, H.G. Joo, K.S. Kim, and S.Q. Zee and colleagues), developed a different "planar MOC solution-based 3D heterogeneous core method" for the DeCART code [2, 6, 10, 11]. This method also discretizes the axial derivative term using a "coarse" radial grid, but most importantly, it simplifies this term in a way that (i) is accurate for problems in which the axial leakage can be represented by Fick's Law, and (ii) offers major advantages for parallel-architecture computers. In some publications, the KAERI method was simply called "2D/1D" [6]. In this work, we refer to the KAIST method in CRX by its original "2D/1D Fusion" name, and we refer to the KAERI method in DeCART by its abbreviated "2D/1D" name. The purpose of this work is to outline a systematic mathematical theory for the 2D/1D methodology developed at KAERI for DeCART.

DeCART (Deterministic Core Analysis Based on Ray Tracing) was originally developed under an I-NERI project between KAERI and ANL. An early version of DeCART was acquired by the University of Michigan (UM), where it has been extensively used in the DOE CASL project. This version has certain deficiencies – in particular, a failure to converge for small axial cell widths Δ_z. In more recent versions of DeCART, the staff at KAERI and ANL have "suppressed" these instabilities. However, in these revisions, the cause of the original iterative instabilities and other basic questions were not answered.

The use of (the UM version of) DeCART demonstrated that for problems in which DeCART converged, it had major computational advantages over other 3D Discrete Ordinates (DO) or Method of Characteristics (MOC) codes. Unfortunately, the failure of DeCART to converge for small Δ_z and the lack of a mathematical foundation for the 2D/1D methodology were major concerns. Nonetheless, discussions took place at UM on the desirability of developing a new 3D reactor physics code that would employ a more robust (but then nonexistent) 2D/1D methodology. To accomplish this, we decided to try to develop a mathematical foundation for the 2D/1D methodology in DeCART – in order to better understand this methodology, and to suggest systematic ways to improve it. The theoretical work has so far been completed for monoenergetic problems in classically "diffusive" media. Our numerical results cover a wider and more interesting range of lattice problems. We have implemented and tested the 2D/1D method in the new MPACT (Michigan Parallel Characteristics Transport Code) code [12].

Our goal in this work is to demonstrate that stable and accurate 2D/1D methods similar to the DeCART method can be systematically derived from a new second-order, integrodifferential "2D/1D equation." The proposed 2D/1D equation and the classic 3D diffusion equation have a similar status: both approximate (simplify) the 3D linear Boltzmann equation. The 2D/1D equation is (i) less expensive to solve than the 3D transport equation, (ii) more complicated and expensive to solve than the 3D diffusion equation, and (iii) well-approximates the 3D Boltzmann equation over a much larger range of problems than the diffusion equation. Specifically: *the 2D/1D equation preserves exact transport physics in the radial directions (x and y),*

but it uses approximate diffusion physics in the axial direction z.

We systematically discretize the 2D/1D equation to obtain a system of discrete equations whose solution converges to the exact 2D/1D solution as the grid (of all independent variables) becomes increasingly fine. We also derive iterative methods for solving the discrete system and analyze these methods by Fourier analysis techniques. This analysis makes it possible to predict the performance of an iterative method before it is implemented, and to avoid iteration methods that are unstable.

In this work, we (i) introduce several new "2D/1D equations" as accurate approximations to the 3D Boltzmann transport equation, (ii) systematically discretize these equation in a straightforward manner, (iii) develop a simple stable iteration strategy for solving the discretized equations, and (iv) apply acceleration to more rapidly converge the solution. Additionally, we provide numerical evidence showing that for geometrically simple 3D problems, the theoretical predictions of (v) the accuracy of the simplest 2D/1D solutions, and (vi) the stability of the "source iteration with under-relaxation" and "CMFD with under-relaxation" iterative methods are valid. More specifically, we show the following:

- Numerical solutions of the 2D/1D equation exist and can be obtained iteratively, in accordance with the theory.
- For 3D problems that are "classically diffusive" (optically thick and highly scattering), the 2D/1D and diffusion solutions both well-approximate the transport solution.
- For problems which are diffusive axially, but not radially, the 2D/1D solutions are more accurate (closer to the solution of the Boltzmann equation) than the standard diffusion solution.
- The "source iteration with under-relaxation" and 'CMFD with under-relaxation" iteration schemes for solving the 2D/1D equation is experimentally stable, and the performance (spectral radius) of this scheme is accurately predicted by the Fourier analysis.

The remainder of this thesis is organized as follows. In Chapter 2, we give a basic

description of solution methods for the 3D Boltzmann equation.

In Chapter 3, we propose several 2D/1D equations that approximate the linear Boltzmann equation in a manner consistent with the spirit of the method in DeCART, and we show some basic properties of these 2D/1D equations. Also, we systematically discretize the 2D/1D equation, and we propose unaccelerated and accelerated iteration methods to solve the discrete equations. This method is related to the original iterative method in DeCART, but the new method has a modification that renders it stable. We additionally describe the use of shape functions to further improve the accuracy of the method.

In Chapter 4, we apply Fourier analysis to predict the convergence behavior of the new iteration schemes. We confirm these predictions with numerical experiments. We also describe a set of problems on which the methods were implemented to test their accuracy. The solutions produced by the 2D/1D method are compared to 3D MOC and 3D diffusion solutions for their accuracy. Finally, we describe a set of problems to evaluate the improved accuracy from the use of shape functions.

In Chapter 5, we apply the 2D/1D method to some more realistic benchmark problems — namely, the C5G7 3D extended problems and the first of the Takeda benchmarks. Additionally, we apply the method to the CASL AMA 3A milestone problem to observe the effects of realistic anisotropic scattering.

In Chapter 6, we provide conclusions regarding the numerical accuracy and the numerical performance of the method. We also discuss future work for the improvement of the method through (i) better diffusion coefficients, (ii) shape functions, (iii) alternate axial methods, and (iv) alternate leakage splitting.

Chapter 2

Background

The derivation of the 2D/1D equation begins with the linear 3D Boltzmann transport equation formulated on a "cylindrical" system V, consisting of points $\mathbf{r} = (x, y, z)$ with the *radial* variables $(x, y) \in R$ (a convex 2D region), and the *axial* variable z in the interval $0 \leq z \leq Z$. (Aside from being convex, R is arbitrary.)

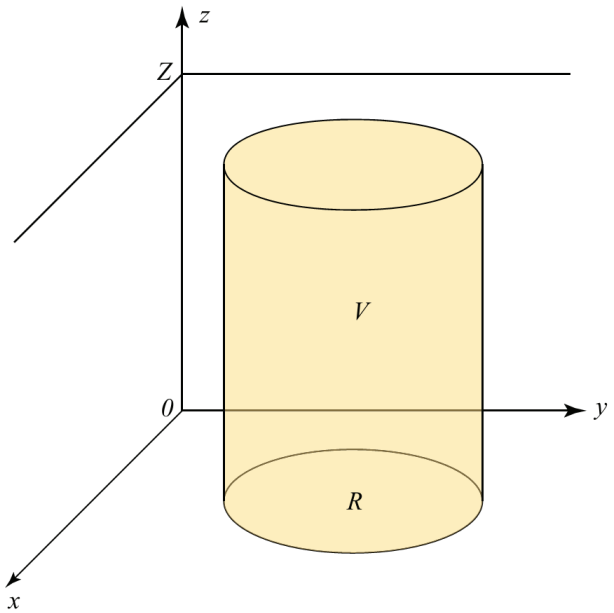

Figure 1: The Cylindrical System V

The approximations that we will introduce to derive the 2D/1D equation only affect the axial streaming term; therefore, for simplicity, we assume monoenergetic transport. Using the notation for the unit angle vector:

$$\mathbf{\Omega} = (\Omega_x, \Omega_y, \Omega_z) = (\sqrt{1-\mu^2}\cos\alpha, \sqrt{1-\mu^2}\sin\alpha, \mu) \ , \tag{2.1}$$

we have the fixed-source monoenergetic transport equation:

$$\mathbf{\Omega}\cdot\boldsymbol{\nabla}\psi(\mathbf{r},\mathbf{\Omega}) + \Sigma_t(\mathbf{r})\psi(\mathbf{r},\mathbf{\Omega}) = S(\mathbf{r},\mathbf{\Omega}) \ , \quad \mathbf{r}\in V \ , \ \mathbf{\Omega}\in 4\pi \ , \tag{2.2a}$$

with the vacuum boundary condition:

$$\psi(\mathbf{r},\mathbf{\Omega}) = 0 \ , \quad \mathbf{r}\in\partial V \ , \ \mathbf{\Omega}\cdot\boldsymbol{n} < 0 \ . \tag{2.2b}$$

The source terms

$$S(\mathbf{r},\mathbf{\Omega}) = S_s(\mathbf{r},\mathbf{\Omega}) + S_f(\mathbf{r},\mathbf{\Omega}) \ , \tag{2.3}$$

consist of the scattering source,

$$S_s(\mathbf{r},\mathbf{\Omega}) = \int\limits_{4\pi} \Sigma_s(\mathbf{r},\mathbf{\Omega}\cdot\mathbf{\Omega}')\psi(\mathbf{r},\mathbf{\Omega}')d\Omega' \ , \tag{2.4}$$

and the fixed-source,

$$S_f(\mathbf{r},\mathbf{\Omega}) = Q(\mathbf{r},\mathbf{\Omega}) \ , \tag{2.5}$$

or the fission source (in an inner iteration of an eigenvalue problem),

$$S_f(\mathbf{r},\mathbf{\Omega}) = \frac{\nu\Sigma_f(\mathbf{r})}{4\pi k_{eff}} \int\limits_{4\pi} \psi(\mathbf{r},\mathbf{\Omega}')d\Omega' \ . \tag{2.6}$$

Alternative boundary conditions could be either an external source, or a spectral albedo source

$$\psi(\mathbf{r},\mathbf{\Omega}) = \psi_{\mathrm{b}}(\mathbf{\Omega}) = \beta\psi(\mathbf{r},\mathbf{\Omega}') \ , \ \mathbf{\Omega}' = \mathbf{\Omega} - 2(\mathbf{\Omega}\cdot\boldsymbol{n})\boldsymbol{n} \ . \tag{2.7}$$

If $\beta = 0$ this is a vacuum boundary condition, while if $\beta = 1$, it is a reflecting

boundary condition.

2.1 Anisotropic Scattering

By applying a Legendre expansion to the scattering kernel,

$$\Sigma_s(\mathbf{r}, \mathbf{\Omega} \cdot \mathbf{\Omega}') = \sum_{n=0}^{N_S} \frac{2n+1}{4\pi} \Sigma_{s,n}(\mathbf{r}) P_n(\mathbf{\Omega} \cdot \mathbf{\Omega}') \ ,$$

we can write Eq. (2.4) as:

$$S_s(\mathbf{r}, \mathbf{\Omega}) = \sum_{n=0}^{N_S} \frac{2n+1}{4\pi} \Sigma_{s,n}(\mathbf{r}) \int_{4\pi} P_n(\mathbf{\Omega} \cdot \mathbf{\Omega}') \psi(\mathbf{r}, \mathbf{\Omega}') d\Omega' \ . \tag{2.8}$$

Finally, we can use the spherical harmonic addition theorem,

$$P_n(\mathbf{\Omega} \cdot \mathbf{\Omega}') = \frac{4\pi}{2n+1} Y_{n,m}(\mathbf{\Omega}) Y_{n,m}(\mathbf{\Omega}') \ ,$$

to obtain:

$$S_s(\mathbf{r}, \mathbf{\Omega}) = \sum_{n=0}^{N_S} \Sigma_{s,n}(\mathbf{r}) \sum_{m=-n}^{n} Y_{n,m}(\mathbf{\Omega}) \int_{4\pi} Y_{n,m}(\mathbf{\Omega}') \psi(\mathbf{r}, \mathbf{\Omega}') d\Omega' \ . \tag{2.9}$$

Here, $Y_{n,m}(\mathbf{\Omega})$ are the real-valued spherical harmonics:

$$Y_{n,m}(\mathbf{\Omega}) = \sqrt{\frac{2n+1}{4\pi} \frac{(n-m)!}{(n+m)!}} P_{n,m}(\mu) \varphi_m(\alpha) \ , \tag{2.10a}$$

$$\varphi_m(\alpha) = \begin{cases} \sqrt{2} \sin(m\alpha) \ , & m < 0 \\ 1 \ , & m = 0 \\ \sqrt{2} \cos(m\alpha) \ , & m > 0 \end{cases} \ , \tag{2.10b}$$

and, $P_{n,m}(\mu)$ are the associated Legendre polynomials:

$$P_{n,m}(\mu) = \frac{\sqrt{(1-\mu^2)^m}}{2^n n!} \frac{d^{n+m}}{d\mu^{n+m}} (\mu^2 - 1)^n \ . \tag{2.11}$$

2.2 The Method of Characteristics

A prevalent method of solving the transport PDE is the Method of Characteristics. Introduced over four decades ago [13], [14], it has become a common method for solving lattice problems and reactor physics problems. We use the Method of Characteristics to solve the 2D transport portion of the 2D/1D method. In this method, the transport PDE is converted to an ODE by replacing the directional derivative of the streaming term with an ordinary derivative:

$$\begin{aligned} \mathbf{\Omega} = \frac{\partial \mathbf{r}}{\partial s} \quad &\rightarrow \quad \mathbf{r} = \mathbf{r}_0 + s\mathbf{\Omega} \ , \\ \mathbf{\Omega} \cdot \boldsymbol{\nabla} \psi(\mathbf{r}, \mathbf{\Omega}) &= \frac{\partial}{\partial s} \psi(\mathbf{r}, \mathbf{\Omega}) \ , \\ \frac{\partial}{\partial s} \psi(\mathbf{r}, \mathbf{\Omega}) + \Sigma_t(\mathbf{r}) \psi(\mathbf{r}, \mathbf{\Omega}) &= S(\mathbf{r}, \mathbf{\Omega}) \ . \end{aligned}$$

A finite number of directions are chosen as the angular quadrature over which the directions are traversed. This transport equation can then be solved analytically with the use of an integrating factor:

$$\frac{\partial}{\partial s} I(\mathbf{r}) = \Sigma_t(\mathbf{r}) I(\mathbf{r}) \ ;$$

we solve this ODE for the integrating factor,

$$I(\mathbf{r}) = \exp\left(\int_0^s \Sigma_t(\mathbf{r}_0 + s'\mathbf{\Omega}) ds' \right) \ .$$

With this, we can write the transport ODE as:

$$\frac{\partial}{\partial s}\big(I(\mathbf{r})\psi(\mathbf{r},\mathbf{\Omega})\big) = I(\mathbf{r})S(\mathbf{r},\mathbf{\Omega}) \ ,$$

Integrating this rearranged transport equation over some length s results in:

$$\begin{aligned}\psi(\mathbf{r}_0 + s\mathbf{\Omega},\mathbf{\Omega}) = \psi(\mathbf{r}_0,\mathbf{\Omega})e^{-\int_0^s \Sigma_t(\mathbf{r}_0+s'\mathbf{\Omega})ds'} \\ + e^{-\int_0^s \Sigma_t(\mathbf{r}_0+s'\mathbf{\Omega})ds'} \int_0^s S(\mathbf{r}_0 + s\mathbf{\Omega},\mathbf{\Omega})e^{\int_0^{s'} \Sigma_t(\mathbf{r}_0+s''\mathbf{\Omega})ds''}ds' \ .\end{aligned} \tag{2.12}$$

By assuming the spatial shape of the source S (e.g. constant) over the domain of integration, Eq. (2.12) can be evaluated explicitly. To produce the MOC numerical solution scheme, we couple this with a discretized version of the transport ODE,

$$\frac{\psi(\mathbf{r}_0 + s_i\mathbf{\Omega},\mathbf{\Omega}) - \psi(\mathbf{r}_0,\mathbf{\Omega})}{s_i} + \Sigma_{t,i}\psi_i(\mathbf{\Omega}) = S_i(\mathbf{\Omega}) \ , \tag{2.13}$$

where $\Sigma_{t,i}$,$\psi_i(\mathbf{\Omega})$, and $S_i(\mathbf{\Omega})$ are the average collision cross section, angular flux, and source, respectively, along ray i. In order to complete this method, the domain needs to be decomposed into such "flat source regions" as seen below in Figure 2.

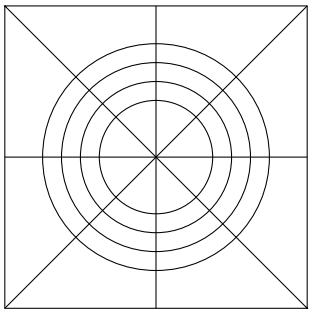

Figure 2: An Example of Flat Source Regions on a Pin Cell

Additionally, as the characteristic equation (Eq. (2.12)) is formed along a line, many such rays must be used to traverse the problem domain. For a given direction within an angular quadrature, parallel rays are placed over the domain. Each ray is used to represent the solution over a section of the problem, based on the spacing

between the rays. In Figure 3, we show multiple rays traversing a flat source region.

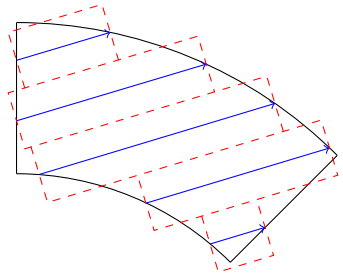

Figure 3: An Example of Rays Traversing a Flat Source Region

Each ray is shown enclosed within a region, which is used to area weight the flat source region angular flux. The length of this region is the ray length s_i, and the width is the ray spacing Δr_i. The flat source region average angular flux is then,

$$\psi_j(\mathbf{\Omega}) = \frac{\sum_{i \in j} s_i \Delta r_i \psi_i(\mathbf{\Omega})}{\sum_{i \in j} s_i \Delta r_i} \ . \tag{2.14}$$

The scalar flux for this region is,

$$\phi_j = \int_{4\pi} \psi_j(\mathbf{\Omega}) d\Omega \ . \tag{2.15}$$

As the ray separation distance decreases, the error that occurs due to the area integration of the angular flux vanishes. Therefore, it is necessary to use numerous rays in order to see good accuracy when using the Method of Characteristics.

2.3 Nodal Diffusion

The nodal diffusion methods are commonly used for the solution of 3D diffusion problems [15]. They can be applied to multiple dimensions in a manner similar to ADI or with CMFD acceleration. We use nodal diffusion methods as an improvement over finite difference methods to solve the 1D diffusion equation of the 2D/1D method. In

our work, nodal methods are applied to the 1D diffusion equation.

$$-\frac{d}{dz}\left(D(z)\frac{d\phi}{dz}\right)+\Sigma_r(z)\phi(z)=S(z)\ . \tag{2.16}$$

The right hand term $S(z)$ is the combination of the fixed source, fission source (in multiplying media), in-scatter source (in multi-group problems), and transverse leakage (in multi-dimension problems). All nodal methods begin with a change of variable applied to the diffusion coefficient to isolate nodal regions. First we define a local spatial variable:

$$\xi(z)=2\frac{z-z_j}{\Delta_j}\ \text{ when }\ z_{j-1/2}\le z\le z_{j+1/2}\ , \tag{2.17a}$$

where

$$2z_j=z_{j+1/2}+z_{j-1/2}\ , \tag{2.17b}$$

and

$$\Delta_j=z_{j+1/2}-z_{j-1/2}\ . \tag{2.17c}$$

Next, we make a change of variables on the scalar flux and source terms:

$$\phi(z)dz=\phi_j(\xi)d\xi\ , \tag{2.17d}$$

$$S(z)dz=S_j(\xi)d\xi\ . \tag{2.17e}$$

On each of these nodes, the cross sections are assumed constant, so that the only spatial variation is due to the scalar flux and source. With this approximation, the diffusion equation becomes:

$$-\Sigma_{D,j}\phi_j''(\xi)+\Sigma_{r,j}\phi_j(\xi)=S_j(\xi)\ , \tag{2.18a}$$

where

$$\Sigma_{D,j} = \frac{4D_j}{\Delta_j^2} \ , \tag{2.18b}$$

and

$$\beta_j = \frac{2D_j}{\Delta_j} \ . \tag{2.18c}$$

Boundary conditions for the nodal methods are determined from diffusion boundary conditions. Fick's law is used to determine the current from the scalar flux:

$$J(z) = -D(z)\frac{d\phi}{dz} \ ,$$

or

$$J_j(\xi) = \beta_j \phi_j'(\xi) \ . \tag{2.19}$$

If we have a reflecting boundary condition at the bottom of the problem, we have:

$$J_0(-1) = \beta_0 \phi_j'(-1) = 0 \ . \tag{2.20}$$

If we have a vacuum boundary condition at the top of the problem, we have:

$$\phi_J(1) - 2J_J(1) = 4J^-_{J+1/2} = 0 \ ,$$

or

$$\phi_J(1) + 2\phi_J'(1) = 0 \ . \tag{2.21}$$

2.3.1 Nodal Approximation

In both the NEM (Nodal Expansion Method) and SANM (Semi-Analytical Nodal Method), the scalar flux and source are approximated on the node with a finite order sum of Legendre polynomials (and solutions to the homogeneous problem with SANM). In both approximations, a Legendre polynomial expansion is applied to the

source:

$$S_j(\xi) = \sum_{n=0}^{4} S_{n,j} P_n(\xi) \ . \tag{2.22}$$

The NEM approximation is given by:

$$\phi_j(\xi) \approx \sum_{n=0}^{4} \phi_{n,j} P_n(\xi) \ . \tag{2.23}$$

The SANM approximation is given by:

$$\phi_j(\xi) \approx A_j \sinh(\kappa_j \xi) + B_j \cosh(\kappa_j \xi) + \sum_{n=0}^{4} \phi_{n,j} P_n(\xi) \ , \tag{2.24a}$$

$$\kappa_j = \sqrt{\frac{\Sigma_{r,j}}{\Sigma_{D,j}}} \ . \tag{2.24b}$$

Applying either of these approximations to the diffusion equation, Eq. (2.18a) yields

$$-\Sigma_{D,j} \sum_{n=0}^{4} \phi_{n,j} P_n''(\xi) + \Sigma_{r,j} \sum_{n=0}^{4} \phi_{n,j} P_n(\xi) = \sum_{l=0}^{4} S_{n,j} P_n(\xi) \ . \tag{2.25}$$

We do not solve this equation in this form, but we take five relevant moments of this equation, $\int_{-1}^{1} d\xi P_m(\xi)$ for $m = 0, ..., 4$. The results of these moments are:

$$\Sigma_{r,j}\phi_{0,j} - 3\Sigma_{D,j}\phi_{2,j} - 10\Sigma_{D,j}\phi_{4,j} = S_{0,j} \ , \tag{2.26a}$$

$$\Sigma_{r,j}\phi_{1,j} - 15\Sigma_{D,j}\phi_{3,j} = S_{1,j} \ , \tag{2.26b}$$

$$\Sigma_{r,j}\phi_{2,j} - 35\Sigma_{D,j}\phi_{4,j} = S_{2,j} \ , \tag{2.26c}$$

$$\Sigma_{r,j}\phi_{3,j} = S_{3,j} \ , \tag{2.26d}$$

$$\Sigma_{r,j}\phi_{4,j} = S_{4,j} \ . \tag{2.26e}$$

If the NEM approximation is used, only the first three of these moments are used. If the SANM approximation is used, all five of these moments are used, and they can

easily be inverted to solve for the scalar flux moments:

$$\phi_{0,j} = \frac{1}{\Sigma_{r,j}}\left(S_{0,j} + 3\frac{S_{2,j}}{\kappa_j^2} + 10\frac{S_{4,j}}{\kappa_j^2} + 105\frac{S_{4,j}}{\kappa_j^4} \right) , \tag{2.27a}$$

$$\phi_{1,j} = \frac{1}{\Sigma_{r,j}}\left(S_{1,j} + 15\frac{S_{3,j}}{\kappa_j^2} \right) , \tag{2.27b}$$

$$\phi_{2,j} = \frac{1}{\Sigma_{r,j}}\left(S_{2,j} + 35\frac{S_{4,j}}{\kappa_j^2} \right) , \tag{2.27c}$$

$$\phi_{3,j} = \frac{S_{3,j}}{\Sigma_{r,j}} , \tag{2.27d}$$

$$\phi_{4,j} = \frac{S_{4,j}}{\Sigma_{r,j}} . \tag{2.27e}$$

2.3.2 Single Node Method

In the 1-node method, inbound partial currents are used as boundary conditions for the node, and the node average scalar flux and outward partial currents are calculated; this can be used to form a complete iteration scheme, but can be improved with a low order update, such as CMFD [16]. The partial current node boundary conditions are:

$$\phi(z) - 2J(z) = 4J^-(z) ,$$
$$\phi(z) + 2J(z) = 4J^+(z) ,$$

or

$$\phi_j(1) + 2\beta_j\phi_j'(1) = 4J^-_{j+1/2} , \tag{2.28a}$$

$$\phi_j(-1) - 2\beta_j\phi_j'(-1) = 4J^+_{j-1/2} . \tag{2.28b}$$

Applying either the NEM or SANM approximation yields an iterative system of equations.

One-Node NEM

Applying the NEM approximation to the node boundary conditions shown before yields two equations towards the five unknowns in the node:

$$\sum_{n=0}^{4} \phi_{n,j}^{(\ell+1)} + \beta_j \sum_{n=0}^{4} n(n+1)\phi_{n,j}^{(\ell+1)} = 4J_{j+1/2}^{-,(\ell)} \,, \tag{2.29a}$$

$$\sum_{n=0}^{4} \phi_{n,j}^{(\ell+1)}(-1)^n + \beta_j \sum_{n=0}^{4} n(n+1)\phi_{n,j}^{(\ell+1)}(-1)^n = 4J_{j-1/2}^{+,(\ell)} \,. \tag{2.29b}$$

The remaining three equations are the taken from Equations (2.26a-c),

$$\Sigma_{r,j}\phi_{0,j}^{(\ell+1)} - 3\Sigma_{D,j}\phi_{2,j}^{(\ell+1)} - 10\Sigma_{D,j}\phi_{4,j}^{(\ell+1)} = S_{0,j}^{(\ell)} \,, \tag{2.29c}$$

$$\Sigma_{r,j}\phi_{1,j}^{(\ell+1)} - 15\Sigma_{D,j}\phi_{3,j}^{(\ell+1)} = S_{1,j}^{(\ell)} \,, \tag{2.29d}$$

$$\Sigma_{r,j}\phi_{2,j}^{(\ell+1)} - 35\Sigma_{D,j}\phi_{4,j}^{(\ell+1)} = S_{2,j}^{(\ell)} \,. \tag{2.29e}$$

The updated node edge partial currents are,

$$J_{j+1/2}^{+,(\ell+1)} = \frac{1}{4}\sum_{n=0}^{4} \phi_{n,j}^{(\ell+1)} - \frac{\Delta_j \Sigma_{D,j}}{4} \sum_{n=0}^{4} \phi_{n,j}^{(\ell+1)} \frac{n(n+1)}{2} \,, \tag{2.29f}$$

and

$$J_{j-1/2}^{-,(\ell+1)} = \frac{1}{4}\sum_{n=0}^{4} \phi_{n,j}^{(\ell+1)}(-1)^n - \frac{\Delta_j \Sigma_{D,j}}{4} \sum_{n=0}^{4} \phi_{n,j}^{(\ell+1)}(-1)^n \frac{n(n+1)}{2} \,. \tag{2.29g}$$

The node average scalar flux is then given by:

$$\bar{\phi}_j = \frac{1}{\Delta_j} \int_{k-1/2}^{k+1/2} \phi(z)dz = \frac{1}{2} \int_{-1}^{1} \phi_j(\xi)d\xi = \phi_{0,j} \,. \tag{2.30}$$

Together, these equations form an iterative system of equations.

One-Node SANM

Applying the SANM approximation to the node boundary conditions yields two equations towards the seven unknowns in the node:

$$\begin{aligned}\big(\sinh(\kappa_j) + 2\beta_j\kappa_j\cosh(\kappa_j)\big)A_j^{(\ell+1)} \\ + \big(\cosh(\kappa_j) + 2\beta_j\kappa_j\sinh(\kappa_j)\big)B_j^{(\ell+1)} \\ = 4J_{j+1/2}^{-,(\ell)} - \sum_{n=0}^{4}\big(1+\beta_j n(n+1)\big)\phi_{n,j}^{(\ell+1)}\ ,\end{aligned} \tag{2.31a}$$

$$\begin{aligned}\big(-\sinh(\kappa_j) + 2\beta_j\kappa_j\cosh(\kappa_j)\big)A_j^{(\ell+1)} \\ + \big(\cosh(\kappa_j) - 2\beta_j\kappa_j\sinh(\kappa_j)\big)B_j^{(\ell+1)} \\ = 4J_{j-1/2}^{+,(\ell)} - \sum_{n=0}^{4}(-1)^n\big(1+\beta_j n(n+1)\big)\phi_{n,j}^{(\ell+1)}\ .\end{aligned} \tag{2.31b}$$

The remaining five equations are the taken from Equations (2.27),

$$\phi_{0,j}^{(\ell+1)} = \frac{1}{\Sigma_{r,j}}\left(S_{0,j}^{(\ell)} + 3\frac{S_{2,j}^{(\ell)}}{\kappa_j^2} + 10\frac{S_{4,j}^{(\ell)}}{\kappa_j^2} + 105\frac{S_{4,j}^{(\ell)}}{\kappa_j^4}\right)\ , \tag{2.31c}$$

$$\phi_{1,j}^{(\ell+1)} = \frac{1}{\Sigma_{r,j}}\left(S_{1,j}^{(\ell)} + 15\frac{S_{3,j}^{(\ell)}}{\kappa_j^2}\right)\ , \tag{2.31d}$$

$$\phi_{2,j}^{(\ell+1)} = \frac{1}{\Sigma_{r,j}}\left(S_{2,j}^{(\ell)} + 35\frac{S_{4,j}^{(\ell)}}{\kappa_j^2}\right)\ , \tag{2.31e}$$

$$\phi_{3,j}^{(\ell+1)} = \frac{S_{3,j}^{(\ell)}}{\Sigma_{r,j}}\ , \tag{2.31f}$$

$$\phi_{4,j}^{(\ell+1)} = \frac{S_{4,j}^{(\ell)}}{\Sigma_{r,j}}\ . \tag{2.31g}$$

The updated node edge partial currents are,

$$J_{j+1/2}^{+,(\ell+1)} = \frac{1}{4}\Bigg(\big(\sinh(\kappa_j) + 2\beta_j\kappa_j\cosh(\kappa_j)\big)A_j^{(\ell+1)} + \big(\cosh(\kappa_j) + 2\beta_j\kappa_j\sinh(\kappa_j)\big)B_j^{(\ell+1)} + \sum_{n=0}^{4}\big(1-\beta_j n(n+1)\big)\phi_{n,j}^{(\ell+1)}\Bigg) , \tag{2.31h}$$

and

$$J_{j-1/2}^{-,(\ell+1)} = \frac{1}{4}\Bigg(\big(-\sinh(\kappa_j) + 2\beta_j\kappa_j\cosh(\kappa_j)\big)A_j^{(\ell+1)} + \big(\cosh(\kappa_j) - 2\beta_j\kappa_j\sinh(\kappa_j)\big)B_j^{(\ell+1)} + \sum_{n=0}^{4}(-1)^n\big(1-\beta_j n(n+1)\big)\phi_{n,j}^{(\ell+1)}\Bigg) . \tag{2.31i}$$

The node average scalar flux is then given by:

$$\bar{\phi}_j = \frac{1}{\Delta_j}\int_{k-1/2}^{k+1/2}\phi(z)dz = \frac{1}{2}\int_{-1}^{1}\phi_j(\xi)d\xi = \frac{\sinh(\kappa_j)}{\kappa_j}B_j + \phi_{0,j} . \tag{2.32}$$

Together, these equations form an iterative system of equations.

2.3.3 Double Node Method

In the 2-node method, the node average scalar fluxes are held constant and a flux continuity and current continuity are enforced on the boundary between two nodes; the iteration scheme ultimately produces updates for the current between each node. This method then requires a low order update (CMFD) to complete the iteration and update the node average scalar flux. The inter-node boundary conditions are:

$$\phi_{j+1}(-1) = \phi_j(1) , \tag{2.33a}$$

$$\Delta_{j+1}\Sigma_{D,j+1}\phi'_{j+1}(-1) = \Delta_j\Sigma_{D,j}\phi'_j(1) \ . \tag{2.33b}$$

Two-Node NEM

Applying the NEM approximation to the inter-node boundary conditions shown above yields two equations towards the eight unknowns in the two nodes; from continuity of flux, we obtain:

$$\bar{\phi}_j^{(\ell)} + \sum_{n=1}^{4} \phi_{n,j}^{(\ell+1)} = \bar{\phi}_{j+1}^{(\ell)} + \sum_{n=1}^{4} \phi_{n,j+1}^{(\ell+1)}(-1)^n \ . \tag{2.34}$$

From continuity of current, we obtain:

$$\beta_j \sum_{n=1}^{4} n(n+1)\phi_{n,j}^{(\ell+1)} = \beta_{j+1} \sum_{n=1}^{4} n(n+1)\phi_{n,j+1}^{(\ell+1)}(-1)^n \ . \tag{2.35}$$

The remaining six equations are the taken from Equations (2.26a-c); for the bottom node, we have:

$$-3\Sigma_{D,j}\phi_{2,j}^{(\ell+1)} - 10\Sigma_{D,j}\phi_{4,j}^{(\ell+1)} = S_{0,j}^{(\ell)} - \Sigma_{r,j}\bar{\phi}_j^{(\ell)} \ , \tag{2.36a}$$

$$\Sigma_{r,j}\phi_{1,j}^{(\ell+1)} - 15\Sigma_{D,j}\phi_{3,j}^{(\ell+1)} = S_{1,j}^{(\ell)} \ , \tag{2.36b}$$

$$\Sigma_{r,j}\phi_{2,j}^{(\ell+1)} - 35\Sigma_{D,j}\phi_{4,j}^{(\ell+1)} = S_{2,j}^{(\ell)} \ . \tag{2.36c}$$

For the top node, we have:

$$-3\Sigma_{D,j+1}\phi_{2,j+1}^{(\ell+1)} - 10\Sigma_{D,j+1}\phi_{4,j+1}^{(\ell+1)} = S_{0,j+1}^{(\ell)} - \Sigma_{r,j+1}\bar{\phi}_{j+1}^{(\ell)} \ , \tag{2.36d}$$

$$\Sigma_{r,j+1}\phi_{1,j+1}^{(\ell+1)} - 15\Sigma_{D,j+1}\phi_{3,j+1}^{(\ell+1)} = S_{1,j+1}^{(\ell)} \ , \tag{2.36e}$$

$$\Sigma_{r,j+1}\phi_{2,j+1}^{(\ell+1)} - 35\Sigma_{D,j+1}\phi_{4,j+1}^{(\ell+1)} = S_{2,j+1}^{(\ell)} \ . \tag{2.36f}$$

The updated inter-node current is,

$$J_{j+1/2}^{(\ell+1/2)} = -\beta_j\big(\phi_{1,j}^{(\ell+1/2)} + 3\phi_{2,j}^{(\ell+1/2)} + 6\phi_{3,j}^{(\ell+1/2)} + 10\phi_{4,j}^{(\ell+1/2)}\big) \ . \tag{2.36g}$$

By coupling this with a low order update, we have a complete iterative system of equations.

Two-Node SANM

Applying the SANM approximation to the node interface boundary conditions yields two equations towards the fourteen unknowns in the two nodes; from continuity of flux, we obtain:

$$\begin{aligned}\sinh(\kappa_j)A_j^{(\ell+1/2)} + \sinh(\kappa_{j+1})A_{j+1}^{(\ell+1/2)} \\ = \cosh(\kappa_{j+1})B_{j+1}^{(\ell+1/2)} - \cosh(\kappa_j)B_j^{(\ell+1/2)} \\ + \sum_{n=0}^{4}\left((-1)^n\phi_{n,j+1}^{(\ell+1/2)} - \phi_{n,j}^{(\ell+1/2)}\right).\end{aligned} \tag{2.37}$$

From continuity of current, we obtain:

$$\begin{aligned}-\beta_j\kappa_j\cosh(\kappa_j)A_j^{(\ell+1/2)} + \beta_{j+1}\kappa_{j+1}\cosh(\kappa_{j+1})A_{j+1}^{(\ell+1/2)} \\ =\beta_{j+1}\kappa_{j+1}\sinh(\kappa_{j+1})B_{j+1}^{(\ell+1/2)} + \beta_j\kappa_j\sinh(\kappa_j)B_j^{(\ell+1/2)} \\ + \sum_{n=0}^{4}\frac{n(n+1)}{2}\left((-1)^n\beta_{j+1}\phi_{n,j+1}^{(\ell+1/2)} + \beta_j\phi_{n,j}^{(\ell+1/2)}\right).\end{aligned} \tag{2.38}$$

Ten of the remaining equations are the taken from Equations (2.27); for the bottom node, we have:

$$\phi_{0,j}^{(\ell+1/2)} = \frac{1}{\Sigma_{r,j}}\left(S_{0,j}^{(\ell)} + 3\frac{S_{2,j}^{(\ell)}}{\kappa_j^2} + 10\frac{S_{4,j}^{(\ell)}}{\kappa_j^2} + 105\frac{S_{4,j}^{(\ell)}}{\kappa_j^4}\right), \tag{2.39}$$

$$\phi_{1,j}^{(\ell+1/2)} = \frac{1}{\Sigma_{r,j}}\left(S_{1,j}^{(\ell)} + 15\frac{S_{3,j}^{(\ell)}}{\kappa_j^2}\right), \tag{2.40}$$

$$\phi_{2,j}^{(\ell+1/2)} = \frac{1}{\Sigma_{r,j}}\left(S_{2,j}^{(\ell)} + 35\frac{S_{4,j}^{(\ell)}}{\kappa_j^2}\right), \tag{2.41}$$

$$\phi_{3,j}^{(\ell+1/2)} = \frac{S_{3,j}^{(\ell)}}{\Sigma_{r,j}}, \tag{2.42}$$

$$\phi_{4,j}^{(\ell+1/2)} = \frac{S_{4,j}^{(\ell)}}{\Sigma_{r,j}} \,. \tag{2.43}$$

For the top node, we have:

$$\phi_{0,j+1}^{(\ell+1/2)} = \frac{1}{\Sigma_{r,j+1}} \left(S_{0,j+1}^{(\ell)} + 3\frac{S_{2,j+1}^{(\ell)}}{\kappa_{j+1}^2} + 10\frac{S_{4,j+1}^{(\ell)}}{\kappa_{j+1}^2} + 105\frac{S_{4,j+1}^{(\ell)}}{\kappa_{j+1}^4} \right) , \tag{2.44}$$

$$\phi_{1,j+1}^{(\ell+1/2)} = \frac{1}{\Sigma_{r,j+1}} \left(S_{1,j+1}^{(\ell)} + 15\frac{S_{3,j+1}^{(\ell)}}{\kappa_{j+1}^2} \right) , \tag{2.45}$$

$$\phi_{2,j+1}^{(\ell+1/2)} = \frac{1}{\Sigma_{r,j+1}} \left(S_{2,j+1}^{(\ell)} + 35\frac{S_{4,j+1}^{(\ell)}}{\kappa_{j+1}^2} \right) , \tag{2.46}$$

$$\phi_{3,j+1}^{(\ell+1/2)} = \frac{S_{3,j+1}^{(\ell)}}{\Sigma_{r,j+1}} \,, \tag{2.47}$$

$$\phi_{4,j+1}^{(\ell+1/2)} = \frac{S_{4,j+1}^{(\ell)}}{\Sigma_{r,j+1}} \,. \tag{2.48}$$

The other two equations are taken from Eq. (2.32); using this node average flux relation, we obtain:

$$B_j^{(\ell+1/2)} = \frac{\kappa_j \left(\bar{\phi}_j^{(\ell)} - \phi_{0,j}^{(\ell+1/2)} \right)}{\sinh(\kappa_j)} \,, \tag{2.49a}$$

and

$$B_{j+1}^{(\ell+1/2)} = \frac{\kappa_{j+1} \left(\bar{\phi}_{j+1}^{(\ell)} - \phi_{0,j+1}^{(\ell+1/2)} \right)}{\sinh(\kappa_{j+1})} \,. \tag{2.49b}$$

The updated inter-node current is,

$$\begin{aligned} J_{j+1/2}^{(\ell+1/2)} = &- \beta_j \kappa_j \Big(\cosh(\kappa_j) A_j^{(\ell+1/2)} + \sinh(\kappa_j) B_j^{(\ell+1/2)} \Big) \\ &- \beta_j \sum_{n=0}^{4} \frac{n(n+1)}{2} \phi_{n,j}^{(\ell+1/2)} \,. \end{aligned} \tag{2.49c}$$

By coupling this with a low order update, we have a complete iterative system of equations.

2.4 Chapter Summary

In this chapter, we have discussed the existing transport solution methods that are utilized in the 2D/1D method. We use the 2D Method of Characteristics and either 1D finite difference or 1D nodal methods to solve the 2D/1D equation. In the next chapter we discuss (i) various 2D/1D approximations, (ii) properties of the 2D/1D equation, and (iii) the iterative methods that we consider to solve the 2D/1D equation.

Chapter 3

Derivation

In typical light water reactors, the cross sections are highly complicated functions of the radial variables x and y, but are relatively simple (almost constant) functions of the axial variable z. *This suggests that the z-dependence of ψ is weak, and that the axial leakage term $\mu\partial\psi/\partial z$ in Eq. (2.2a) can be approximated advantageously, with a minimal loss of accuracy.* Thus, we write Eq. (2.2a) as:

$$\sqrt{1-\mu^2}\boldsymbol{\Omega}_r \cdot \boldsymbol{\nabla}_r \psi(\mathbf{r},\boldsymbol{\Omega}) + \Sigma_t(\mathbf{r})\psi(\mathbf{r},\boldsymbol{\Omega}) = S(\mathbf{r},\boldsymbol{\Omega}) - L_z(\mathbf{r},\boldsymbol{\Omega}) \ , \tag{3.1a}$$

$$\boldsymbol{\Omega}_r = (\cos\alpha, \sin\alpha) \ , \ \boldsymbol{\nabla}_r = (\partial/\partial x, \partial/\partial y) \ ,$$

$$L_z(\mathbf{r},\boldsymbol{\Omega}) = \mu\frac{\partial}{\partial z}\psi(\mathbf{r},\boldsymbol{\Omega}) \ , \tag{3.1b}$$

and we consider various approximations to L_z.

NB: The MOC integral kernel, Eq. (2.12), was defined for three-dimensional sweeps. The approximations that we will make to L_z allow us to perform *two* dimensional MOC calculations. This results in a significant improvement in computational efficiency while still allowing us to solve three dimensional problems. The 2D MOC kernel posseses the same form as the 3D kernel, but with Σ_t becoming $\Sigma_t/\sqrt{1-\mu^2}$ and S becoming $(S-L_z)/\sqrt{1-\mu^2}$.

3.1 2D/1D Approximation Hierarchy

Two spherical harmonic expansions can be made of Eq. (3.1b). The first is obtained by using a spherical harmonic expansion of the angular flux:

$$L_z(\mathbf{r},\mathbf{\Omega}) = \frac{\partial}{\partial z}\sum_{n=0}^{\infty}\sum_{m=-n}^{n}\mu Y_{n,m}(\mathbf{\Omega})\int_{4\pi} Y_{n,m}(\mathbf{\Omega}')\psi(\mathbf{r},\mathbf{\Omega}')d\Omega' \; ; \tag{3.2a}$$

alternatively, the expansion can be made on the product of the polar cosine and the angular flux:

$$L_z(\mathbf{r},\mathbf{\Omega}) = \frac{\partial}{\partial z}\sum_{n=0}^{\infty}\sum_{m=-n}^{n} Y_{n,m}(\mathbf{\Omega})\int_{4\pi} \mu' Y_{n,m}(\mathbf{\Omega}')\psi(\mathbf{r},\mathbf{\Omega}')d\Omega' \; . \tag{3.2b}$$

The first of these expansions is akin to the standard application of the spherical harmonic functions to the solution of transport equations, whereas the second explicity captures the moments of L_z. In order to preserve particle balance, any approximations to L_z must preserve its isotropic moment:

$$\int_{4\pi} L_z(\mathbf{r},\mathbf{\Omega})d\Omega = \frac{\partial}{\partial z}\int_{4\pi}\mu\psi(\mathbf{r},\mathbf{\Omega})d\Omega = \frac{\partial}{\partial z}J_z(\mathbf{r}) \; . \tag{3.3}$$

In both forms of Eq. (3.2), the term $\mu Y_{n,m}(\mathbf{\Omega})$ appears. The influence of this term can be better understood using the recurrence relation of the associated Legendre polynomials:

$$(n+1-m)P_{n+1,m}(\mu) = \mu(2n+1)P_{n,m}(\mu) - (n+m)P_{n-1,m}(\mu) \; . \tag{3.4}$$

This can be rearranged to isolate $\mu P_{n,m}$ as:

$$\mu P_{n,m}(\mu) = \frac{n+1-m}{2n+1}P_{n+1,m}(\mu) + \frac{n+m}{2n+1}P_{n-1,m}(\mu) \; .$$

Using the definition of the spherical harmonics in Eq. (2.10a):

$$\begin{aligned}
\mu Y_{n,m}(\mathbf{\Omega}) &= \sqrt{\frac{2n+1}{4\pi}\frac{(n-m)!}{(n+m)!}}\mu P_{n,m}(\mu)\varphi_m(\alpha) \\
&= \sqrt{\frac{2n+1}{4\pi}\frac{(n-m)!}{(n+m)!}}\left(\frac{n+1-m}{2n+1}P_{n+1,m}(\mu) + \frac{n+m}{2n+1}P_{n-1,m}(\mu)\right)\varphi_m(\alpha) \\
= \sqrt{\frac{2(n+1)+1}{4\pi}\frac{(n+1-m)!}{(n+1+m)!}}&\sqrt{\frac{2n+1}{2n+3}\frac{n+1+m}{n+1-m}}\frac{n+1-m}{2n+1}P_{n+1,m}(\mu)\varphi_m(\alpha) \\
+ \sqrt{\frac{2(n-1)+1}{4\pi}\frac{(n-1-m)!}{(n-1+m)!}}&\sqrt{\frac{2n+1}{2n-1}\frac{n-m}{n+m}}\frac{n+m}{2n+1}P_{n-1,m}(\mu)\varphi_m(\alpha) \\
&= \sqrt{\frac{n+1+m}{2n+3}\frac{n+1-m}{2n+1}}Y_{n+1,m}(\mathbf{\Omega}) + \sqrt{\frac{n+m}{2n+1}\frac{n-m}{2n-1}}Y_{n-1,m}(\mathbf{\Omega}) \\
\mu Y_{n,m}(\mathbf{\Omega}) &= \sqrt{\frac{(n+1)^2-m^2}{4(n+1)^2-1}}Y_{n+1,m}(\mathbf{\Omega}) + \sqrt{\frac{n^2-m^2}{4n^2-1}}Y_{n-1,m}(\mathbf{\Omega})\ .
\end{aligned}$$

This result shows how the axial streaming term causes moments of the angular flux to be broadcast to other moments of the source.

The expansions presented in Eq. (3.2) can be truncated at various values of $n = N_L$ to obtain different approximations; while higher order truncations are of interest, only zeroth and first order truncations have thus far been considered. If Eq. (3.2a) is truncated at $N_L = 1$ and rearranged, the standard P_1 approximation is obtained for the angular flux:

$$L_z(\mathbf{r},\mathbf{\Omega}) \approx \frac{\partial}{\partial z}\frac{\mu}{4\pi}\left(\phi(\mathbf{r}) + 3\mathbf{\Omega}\cdot\mathbf{J}(\mathbf{r})\right)\ , \tag{3.5a}$$

where:

$$\begin{aligned}
\phi(\mathbf{r}) &= \int_{4\pi}\psi(\mathbf{r},\mathbf{\Omega})d\Omega\ , \\
\mathbf{J}(\mathbf{r}) = (J_x, J_y, J_z) &= \int_{4\pi}\mathbf{\Omega}\psi(\mathbf{r},\mathbf{\Omega})d\Omega\ .
\end{aligned}$$

In a simpler approximation, the radial current terms in Eq. (3.5a) are discarded,

yielding the "diffusion leakage":

$$L_z(\mathbf{r}, \mathbf{\Omega}) \approx \frac{\mu}{4\pi} \frac{\partial}{\partial z} \left(\phi + 3\mu J_z(\mathbf{r})\right) \ . \tag{3.5b}$$

A further simpler approximation, the "quadratic leakage", can be obtained by neglecting the odd polar cosine moment:

$$L_z(\mathbf{r}, \mathbf{\Omega}) \approx \frac{3\mu^2}{4\pi} \frac{\partial}{\partial z} J_z(\mathbf{r}) \ . \tag{3.5c}$$

If the approximation Eq. 3.2b is truncated at $N_L = 1$ and only zonal harmonics are retained, a "linear leakage" approximation is obtained:

$$L_z(\mathbf{r}, \mathbf{\Omega}) \approx \frac{1}{4\pi} \frac{\partial}{\partial z} \left(J_z(\mathbf{r}) + \mu\phi(\mathbf{r})\right) \ . \tag{3.6a}$$

If only the zeroth order term of Eq. 3.2b is retained, an "isotropic leakage" is obtained:

$$L_z(\mathbf{r}, \mathbf{\Omega}) \approx \frac{1}{4\pi} \frac{\partial}{\partial z} J_z(\mathbf{r}) \ . \tag{3.6b}$$

Fick's law is used in the quadratic and isotropic leakage approximations to approximate the axial current, as the 2D transport sweep cannot solely generate odd polar cosine moments without an odd polar cosine driving source:

$$J_z(\mathbf{r}) \approx -D \frac{\partial}{\partial z} \phi(\mathbf{r}) \ . \tag{3.7}$$

In the approximations using Fick's law, D is the diffusion coefficient and in homogeneous media, $D = 1/3\Sigma_t$. The progression from Eq. (3.5a) to (3.6b) becomes increasingly simple and (presumably) less accurate. In this work, we consider this spectrum of approximations, Eq. (3.5 – 3.6). The vacuum boundary conditions for Eq. (3.1) remain the standard transport vacuum boundary condition on the "sides" of ∂V:

$$\psi(\mathbf{r}, \mathbf{\Omega}) = 0 \ , \quad (x, y) \in \partial R \ , \ 0 < z < Z \ , \ \mathbf{\Omega} \cdot \boldsymbol{n} < 0 \ , \tag{3.8a}$$

but become P_1 boundary conditions on the "top" and "bottom" of V, with diffusion

boundary conditions occurring if Fick's law is used. The P_1 boundary conditions are:

$$\phi(x,y,0) + 2J_z(x,y,0) = 0 \ , \quad (x,y) \in R \ , \tag{3.8b}$$

$$\phi(x,y,Z) - 2J_z(x,y,Z) = 0 \ , \quad (x,y) \in R \ . \tag{3.8c}$$

The integrodifferential 2D/1D Eq. (3.1) approximates the linear Boltzmann equation only in its axial derivative term; this equation is first or second order depending on the explicit use of Fick's law for some leakage approximations. The radial derivative terms in Eq. (3.1) are not approximated, and—unlike the standard diffusion equation—the angular variable is not eliminated from the 2D/1D equation.

3.1.1 Considerations of the 2D Transport Equation

In the simulation of nuclear reactors, generally only power and reaction rates (therefore the scalar flux) are of interest. By using the 2D Boltzmann transport equation, the polar symmetry of the transport operator can result in different leakage approximations producing the same scalar flux if care is not taken. Consider the streaming and collision operator of the 2D Boltzmann transport equation:

$$\mathfrak{L}_{\mu,\alpha}\psi(\mathbf{r},\mathbf{\Omega}) = \sqrt{1-\mu^2}\left(\cos\alpha\frac{\partial}{\partial x} + \sin\alpha\frac{\partial}{\partial y}\right)\psi(\mathbf{r},\mathbf{\Omega}) + \Sigma_t(\mathbf{r})\psi(\mathbf{r},\mathbf{\Omega}) \ . \tag{3.9}$$

The 2D/1D transport equation (see Eq. 3.1) can now be rewritten as:

$$\mathfrak{L}_{\mu,\alpha}\psi(\mathbf{r},\mathbf{\Omega}) = S(\mathbf{r},\mathbf{\Omega}) - L_z(\mathbf{r},\mathbf{\Omega}) \ . \tag{3.10}$$

We solve this equation for the angular flux and then integrate to obtain the scalar flux:

$$\psi(\mathbf{r},\mathbf{\Omega}) = \mathfrak{L}^{-1}_{\mu,\alpha}\left\{S(\mathbf{r},\mathbf{\Omega}) - L_z(\mathbf{r},\mathbf{\Omega})\right\} \ ,$$

$$\phi(\mathbf{r},\mathbf{\Omega}) = \int\limits_{4\pi} \mathfrak{L}^{-1}_{\mu,\alpha}\left\{S(\mathbf{r},\mathbf{\Omega}) - L_z(\mathbf{r},\mathbf{\Omega})\right\} d\Omega \ .$$

The transport operator $\mathfrak{L}_{\mu,\alpha}$ is clearly symmetric in μ; therefore, in the equation for the scalar flux, any odd moments in μ of the integrand are eliminated. For the P_1, diffusion, and quadratic leakage approximations, we obtain:

$$\phi(\mathbf{r},\mathbf{\Omega}) = \int_{4\pi} \mathfrak{L}^{-1}_{\mu,\alpha} \left\{ S(\mathbf{r},\mathbf{\Omega}) - \frac{3\mu^2}{4\pi}\frac{\partial}{\partial z} J_z(\mathbf{r}) \right\} d\Omega \ .$$

For the linear and isotropic leakage approximations, we obtain:

$$\phi(\mathbf{r},\mathbf{\Omega}) = \int_{4\pi} \mathfrak{L}^{-1}_{\mu,\alpha} \left\{ S(\mathbf{r},\mathbf{\Omega}) - \frac{1}{4\pi}\frac{\partial}{\partial z} J_z(\mathbf{r}) \right\} d\Omega \ .$$

In both of these forms, even with arbitrary anisotropic scattering, the only odd polar cosine moment that the scalar flux is coupled to is the current in the axial leakage term. If we use Fick's law to approximate the current using the scalar flux, we break this final coupling and completely decouple the scalar flux from the polar cosine odd moments of the angular flux. Thus, if the polar cosine odd moments of the angular flux are to be effectively incorporated into an axial leakage approximation, other calculations are necessary that avoid the use of Fick's law.

3.1.2 Choosing the Diffusion Coefficient

For diffusive homogeneous medium problems, the diffusion coefficient can be confidently chosen as $D = 1/3\Sigma_{tr}$, where $\Sigma_{tr} = \Sigma_t - \Sigma_{s,1}$; however, for reactor cores, in which ψ is a strong function of x, y, and $\mathbf{\Omega}$, classic diffusion theory is not valid, and a more sophisticated approximation to the axial leakage term becomes necessary for optimum accuracy. An asymptotic theory has been developed that provides the logic needed to specify D on a heterogeneous lattice problem [18, 19]. More simply, the diffusion coefficient can be estimated as an Eddington factor–the ratio

$$D = \frac{\int_{4\pi} \mu^2 \psi(\mathbf{r},\mathbf{\Omega}) d\Omega}{\Sigma_t \int_{4\pi} \psi(\mathbf{r},\mathbf{\Omega}) d\Omega}. \tag{3.11}$$

Alternatively, the diffusion coefficient on a discretized problem can be chosen to exactly preserve the transport behavior of a continuous homogeneous 1D transport equation. We will discuss how this could be done for different region types in the following subsections. These approximations would still rely on a simple flux-weighted averaging method for homogenizing the lattice structure, but would introduce more transport physics into the diffusion coefficient than the standard choice.

Shielding

It is possible to formulate a *discrete* diffusion coefficient so that—with no error—a numerical solution will decay exponentially at a specified rate. This would be appropriate in a reflector region of realistic reactor problem and in control rod, absorber rod, and water rod regions. We derive this by starting with a continuous transport equation with an ansatz for the solution and apply the result to a discrete diffusion equation.

Continuous Transport Solution We consider the following 1-D shielding problem:

$$\mu\frac{\partial\psi}{\partial z}+\Sigma_t\psi=\frac{\Sigma_s}{2}\int_{-1}^{1}\psi d\mu' \qquad 0<z<\infty\ , \tag{3.12a}$$

$$\psi(0,\mu)=\psi^b(\mu) \qquad \mu>0\ . \tag{3.12b}$$

We assume the solution has the form

$$\psi(z,\mu)=f(\mu)e^{-\Sigma_t\kappa z}\ . \tag{3.13}$$

Inserting the ansatz into the original problem, we obtain

$$\Sigma_t(1-\kappa\mu)f(\mu)=\frac{\Sigma_s}{2}\int_{-1}^{1}f(\mu')d\mu'\ . \tag{3.14}$$

Dividing this equation by $1-\kappa\mu$, integrating this equation over all angles $\int_{-1}^{1} d\mu$, and defining the scattering ratio as $c = {}^{\Sigma_s}/_{\Sigma_t}$, yields the dispersion relation:

$$\begin{aligned} 1 &= \frac{c}{2}\int_{-1}^{1} \frac{d\mu}{1-\kappa\mu} \\ &= \frac{c}{2}\int_{-1}^{1} \frac{1+\kappa\mu}{1-(\kappa\mu)^2} d\mu \\ &= c\int_{0}^{1} \frac{d\mu}{1-(\kappa\mu)^2} \\ &= \frac{c}{\kappa}\int_{0}^{\kappa} \frac{d\mu'}{1-\mu'^2} \ , \end{aligned}$$

or

$$\frac{\kappa}{c} = \tanh^{-1}\kappa \ . \tag{3.15}$$

Although this relation cannot be solved explicitly, Newton's iteration can successfully be applied to solve it iteratively. Many iterative forms are possible; but, for the most fast and stable version that we found, we seek the zero of:

$$g(\kappa) = \kappa - \tanh\left({}^{\kappa}/_{c}\right) \ .$$

The derivative of this function is:

$$g'(\kappa) = 1 - \frac{\operatorname{sech}^2\left({}^{\kappa}/_{c}\right)^2}{c} \ ,$$

Applying Newton's iteration, we obtain:

$$\begin{aligned} \kappa_{n+1} &= \kappa_n - \frac{g(\kappa_n)}{g'(\kappa_n)} \ , \\ &= \kappa_n - c\frac{\kappa_n - \tanh\left({}^{\kappa_n}/_{c}\right)}{c - \operatorname{sech}^2\left({}^{\kappa_n}/_{c}\right)} \ . \end{aligned} \tag{3.16}$$

The initial guess can be well approximated (within 1% for $c \leq 0.96$) with the empirical relation,

$$\kappa_0 = \left(1 - c^P\right)^R , \tag{3.17}$$

where

$$P = 3.43965192818363 ,$$
$$R = 0.534370910533648 .$$

For every $0 < c < 1$, $\exists$ exactly one $\pm$ pair of κ satisfying Eq. (3.15). Suppose $\kappa > 0$ is the positive solution. Then, for $z \gg 1$,

$$\psi(z, \mu) \approx C_0 f(\mu) e^{-\Sigma_t \kappa z} , \tag{3.18a}$$

and

$$\phi(z) \approx C_1 e^{-\Sigma_t \kappa z} . \tag{3.18b}$$

Discrete Diffusion Solution By formulating a diffusion problem on a grid, we can find a diffusion coefficient that causes the numerical diffusion solution to decay exactly as Eq. (3.18b),

$$-\frac{D}{\Delta_z^2}\left(\phi_{k+1} - 2\phi_k + \phi_{k-1}\right) + \Sigma_a \phi_k = 0 .$$

Applying the scalar flux ansatz from Eq. (3.18b), we obtain the desired diffusion coefficient,

$$-\frac{D}{\Delta_z^2}\left(e^{-\Sigma_t \Delta_z \kappa} - 2 + e^{\Sigma_t \Delta_z \kappa}\right) + \Sigma_a = 0 ,$$

or

$$\frac{2D}{\Delta_z^2}\left(\cosh\left(\Sigma_t \Delta_z \kappa\right) - 1\right) = \Sigma_a .$$

Solving for D, we get:

$$D = \frac{\Sigma_a \Delta_z^2}{2\big(\cosh\left(\Sigma_t \Delta_z \kappa\right) - 1\big)} \ . \tag{3.19}$$

Buckling

It is possible to formulate a *discrete* diffusion coefficient so that—with no error—a numerical solution will preserve a specified buckling. This would be appropriate in the fuel region of a realistic reactor problem. We derive this by starting with a continuous transport equation with an ansatz for the solution and apply the result to a discrete diffusion equation.

Continuous Transport Solution Consider the following eigenvalue problem:

$$\mu \frac{\partial \psi}{\partial z} + \Sigma_t \psi = \frac{1}{2}\big(\Sigma_s + \lambda \nu \Sigma_f\big) \int_{-1}^{1} \psi d\mu' \qquad -Z < z < Z \ , \tag{3.20a}$$

$$\psi(-Z, \mu) = 0 \qquad \mu > 0 \ , \tag{3.20b}$$

$$\psi(Z, \mu) = 0 \qquad \mu < 0 \ . \tag{3.20c}$$

We assume the solution has the form

$$\psi(z, \mu) = f(\mu) e^{i \Sigma_t \kappa z} \ . \tag{3.21}$$

Inserting the ansatz into Eq. (3.20a), we obtain

$$\Sigma_t (1 + i\kappa\mu) f(\mu) = \frac{1}{2}\big(\Sigma_s + \lambda \nu \Sigma_f\big) \int_{-1}^{1} f(\mu') d\mu' \ . \tag{3.22}$$

Dividing this equation by $1 + i\kappa\mu$, integrating this equation over all angles $\int_{-1}^{1} d\mu$ yields the dispersion relation:

$$\begin{aligned} 1 &= \frac{\Sigma_s + \lambda\nu\Sigma_f}{2\Sigma_t} \int_{-1}^{1} \frac{d\mu}{1 + i\kappa\mu} \\ &= \frac{\Sigma_s + \lambda\nu\Sigma_f}{2\Sigma_t} \int_{-1}^{1} \frac{1 - i\kappa\mu}{1 + (\kappa\mu)^2} d\mu \\ &= \frac{\Sigma_s + \lambda\nu\Sigma_f}{\Sigma_t} \int_{0}^{1} \frac{d\mu}{1 + (\kappa\mu)^2} \\ &= \frac{\Sigma_s + \lambda\nu\Sigma_f}{\Sigma_t} \int_{0}^{\kappa} \frac{d\mu'}{1 + \mu'^2} \ , \end{aligned}$$

or

$$\frac{\kappa\Sigma_t}{\Sigma_s + \lambda\nu\Sigma_f} = \tan^{-1}\kappa \ . \tag{3.23}$$

For every $0 < {\Sigma_t}/{\Sigma_s + \lambda\nu\Sigma_f} < 1$, $\exists$ exactly one $\pm$ pair of κ satisfying this equation. Suppose $\kappa > 0$ is the positive solution. Then, for $z \gg 1$,

$$\psi(z, \mu) \approx C_0 f(\mu) e^{i\Sigma_t \kappa z} \ , \tag{3.24a}$$

and

$$\phi(z) \approx C_1 e^{i\Sigma_t \kappa z} \ . \tag{3.24b}$$

Discrete Diffusion Solution By formulating a diffusion problem on a grid, we can find a diffusion coefficient that causes the solution to buckle exactly as Eq.

(3.24b),

$$-\frac{D}{\Delta_z^2}\big(\phi_{k+1} - 2\phi_k + \phi_{k-1}\big) + \big(\Sigma_a - \lambda\nu\Sigma_f\big)\phi_k = 0 \ .$$

Applying the scalar flux ansatz from Eq. (3.24b), we obtain the desired diffusion coefficient,

$$-\frac{D}{\Delta_z^2}\big(e^{i\Sigma_t\Delta_z\kappa} - 2 + e^{-i\Sigma_t\Delta_z\kappa}\big) + \Sigma_a - \lambda\nu\Sigma_f = 0 \ ,$$

or

$$\frac{2D}{\Delta_z^2}\big(1 - \cos\left(\Sigma_t\Delta_z\kappa\right)\big) = \lambda\nu\Sigma_f - \Sigma_a \ .$$

Solving for D, we get:

$$D = \frac{\big(\lambda\nu\Sigma_f - \Sigma_a\big)\Delta_z^2}{4\sin^2\left(\Sigma_t\Delta_z\kappa/2\right)} \ . \tag{3.25}$$

In this thesis, we use the $D = 1/3\Sigma_t$, but these and possibly other definitions of D are possible and could be explored in future work.

3.2 Properties of the 2D/1D Approximation

Here we discuss some basic properties of the 2D/1D Eq. (3.1).

1. *Conjecture: The 2D/1D equation with vacuum boundary conditions [Eqs. (3.1) and (3.8)] has a positive solution.* Eq. (3.1) is an unfamiliar (second-order integrodifferential) equation which, to our knowledge, has not been studied previously. Our work has shown experimentally that positive solution exist for discrete versions of Eqs. (3.1) and (3.8) for many problems. Unfortunately, proving the stated conjecture for the continuous 2D/1D equation is beyond our capability at this time. To proceed, we assume that the conjecture is true for our problems of interest, but concede that negative solutions may exist given the

form of Eq. (3.1)

2. *If the 2D/1D equation with vacuum boundary conditions has a solution, it is unique.* To prove this statement, let us assume there are two different solutions to this equation $\psi_1(\mathbf{r},\mathbf{\Omega})$ and $\psi_2(\mathbf{r},\mathbf{\Omega})$. Taking the difference between these two equations and setting $\psi_D(\mathbf{r},\mathbf{\Omega}) = \psi_1(\mathbf{r},\mathbf{\Omega}) - \psi_2(\mathbf{r},\mathbf{\Omega})$ results in the equation:

$$\begin{gathered}\mathbf{\Omega}_r \cdot \boldsymbol{\nabla}_r \psi_D(\mathbf{r},\mathbf{\Omega})\sqrt{1-\mu^2} + L_z(\mathbf{r},\mathbf{\Omega}) + \Sigma_t(\mathbf{r})\psi_D(\mathbf{r},\mathbf{\Omega}) = S_s(\mathbf{r},\mathbf{\Omega}) \ , \\ \psi_D(\mathbf{r},\mathbf{\Omega}) = 0 \ , \quad (x,y) \in \partial R \ , \ 0 < z < Z \ , \ \mathbf{\Omega}\cdot\boldsymbol{n} < 0 \ .\end{gathered}$$

Multiplying this equation by $\psi_D(\mathbf{r},\mathbf{\Omega})$ and integrating over the phase space results in:

$$\begin{aligned}\iint\limits_{4\pi\times V} \psi_D(\mathbf{r},\mathbf{\Omega})\mathbf{\Omega}_r \cdot \boldsymbol{\nabla}_r \psi_D(\mathbf{r},\mathbf{\Omega})\sqrt{1-\mu^2}\,d\Omega dV + \iint\limits_{4\pi\times V} \psi_D(\mathbf{r},\mathbf{\Omega}) L_z(\mathbf{r},\mathbf{\Omega}) d\Omega dv \\ + \int\limits_V \Sigma_t(\mathbf{r}) \int\limits_{4\pi} \psi_D^2(\mathbf{r},\mathbf{\Omega}) d\Omega dV = \iint\limits_{4\pi\times V} \psi_D(\mathbf{r},\mathbf{\Omega}) S_s(\mathbf{r},\mathbf{\Omega}) d\Omega dV \ .\end{aligned} \tag{3.26}$$

To handle the scattering source kernel, consider the nonnegative integral:

$$\begin{aligned}0 &\le \iint\limits_{4\pi\times 4\pi} \Sigma_s(\mathbf{r},\mathbf{\Omega}\cdot\mathbf{\Omega}') \left(\psi_D(\mathbf{r},\mathbf{\Omega}) - \psi_D(\mathbf{r},\mathbf{\Omega}')\right)^2 d\Omega' d\Omega \ , \\ &= \iint\limits_{4\pi\times 4\pi} \Sigma_s(\mathbf{r},\mathbf{\Omega}\cdot\mathbf{\Omega}') \left(\psi_D^2(\mathbf{r},\mathbf{\Omega}) - 2\psi_D(\mathbf{r},\mathbf{\Omega})\psi_D(\mathbf{r},\mathbf{\Omega}') + \psi_D^2(\mathbf{r},\mathbf{\Omega}')\right) d\Omega' d\Omega \ ,\end{aligned}$$

or

$$\begin{aligned}\Sigma_{s0}(\mathbf{r}) \int\limits_{4\pi} \psi_D^2(\mathbf{r},\mathbf{\Omega}) d\Omega &\ge \iint\limits_{4\pi\times 4\pi} \Sigma_s(\mathbf{r},\mathbf{\Omega}\cdot\mathbf{\Omega}') \psi_D(\mathbf{r},\mathbf{\Omega})\psi_D(\mathbf{r},\mathbf{\Omega}') d\Omega' d\Omega \ , \\ &= \int\limits_{4\pi} \psi_D(\mathbf{r},\mathbf{\Omega}) S_s(\mathbf{r},\mathbf{\Omega}) d\Omega \ ,\end{aligned}$$

where

$$S_s(\mathbf{r},\mathbf{\Omega}) = \int\limits_{4\pi} \Sigma_s(\mathbf{r},\mathbf{\Omega}\cdot\mathbf{\Omega}')\psi_D(\mathbf{r},\mathbf{\Omega}')d\Omega' \ .$$

Applying this to Eq. (3.26), we get:

$$\iint\limits_{4\pi\times V} \psi_D(\mathbf{r},\mathbf{\Omega})\mathbf{\Omega}_r\cdot\boldsymbol{\nabla}_r\psi_D(\mathbf{r},\mathbf{\Omega})\sqrt{1-\mu^2}d\Omega dV + \iint\limits_{4\pi\times V} \psi_D(\mathbf{r},\mathbf{\Omega})L_z(\mathbf{r},\mathbf{\Omega})d\Omega dv$$
$$+ \int\limits_V \Sigma_t(\mathbf{r}) \int\limits_{4\pi} \psi_D^2(\mathbf{r},\mathbf{\Omega})d\Omega dV \leq \int\limits_V \Sigma_{s0}(\mathbf{r}) \int\limits_{4\pi} \psi_D^2(\mathbf{r},\mathbf{\Omega})d\Omega \ ,$$

or

$$\iint\limits_{4\pi\times V} \psi_D(\mathbf{r},\mathbf{\Omega})\mathbf{\Omega}_r\cdot\boldsymbol{\nabla}_r\psi_D(\mathbf{r},\mathbf{\Omega})\sqrt{1-\mu^2}d\Omega dV + \iint\limits_{4\pi\times V} \psi_D(\mathbf{r},\mathbf{\Omega})L_z(\mathbf{r},\mathbf{\Omega})d\Omega dv$$
$$+ \int\limits_V (\Sigma_t(\mathbf{r}) - \Sigma_{s0}(\mathbf{r})) \int\limits_{4\pi} \psi_D^2(\mathbf{r},\mathbf{\Omega})d\Omega dV \leq 0 \ .$$

Now we consider the first integral of Eq. (3.26):

$$\iint\limits_{4\pi\times V} \psi_D(\mathbf{r},\mathbf{\Omega})\mathbf{\Omega}_r\cdot\boldsymbol{\nabla}_r\psi_D(\mathbf{r},\mathbf{\Omega})\sqrt{1-\mu^2}d\Omega dV \ .$$

By rearranging the angular flux gradient and applying the divergence theorem, we find that it is equivalent to

$$\iint\limits_{4\pi\times\delta R\times Z} \frac{\mathbf{\Omega}_r\cdot\mathbf{n}_r}{2}\psi_D^2(\mathbf{r},\mathbf{\Omega})\sqrt{1-\mu^2}d\Omega dA dz \ .$$

From the boundary condition $\psi_D(\mathbf{r},\mathbf{\Omega}) = 0$ when $\mathbf{\Omega}\cdot\mathbf{n} < 0$, therefore, it is clear that this integral is nonnegative. Next, we consider the second integral of Eq.

(3.26):

$$\iint\limits_{4\pi\times V} \psi_D(\mathbf{r},\mathbf{\Omega})L_z(\mathbf{r},\mathbf{\Omega})d\Omega dV \ .$$

It is easier to show the nonnegativity of this integral for some leakage approximations than others. The linear approximation given by Eq. (3.6a) is a straightforward example:

$$\begin{aligned}\iint\limits_{4\pi\times V} \psi_D(\mathbf{r},\mathbf{\Omega})L_z(\mathbf{r},\mathbf{\Omega})d\Omega dV &= \frac{1}{4\pi}\iint\limits_{4\pi\times V} \psi_D(\mathbf{r},\mathbf{\Omega})\frac{\partial}{\partial z}\left(J_z(\mathbf{r})+\mu\phi(\mathbf{r})\right)d\Omega dV \\ &= \frac{1}{4\pi}\int\limits_V \phi(\mathbf{r})\frac{\partial}{\partial z}J_z(\mathbf{r}) + J_z(\mathbf{r})\frac{\partial}{\partial z}\phi(\mathbf{r})dV \\ &= \frac{1}{4\pi}\int\limits_V \frac{\partial}{\partial z}\left(J_z(\mathbf{r})\phi(\mathbf{r})\right)dV \\ &= \frac{1}{4\pi}\int\limits_R J_z(x,y,Z)\phi(x,y,Z) - J_z(x,y,0)\phi(x,y,0)dA \ .\end{aligned}$$

By applying the boundary conditions of Eq. (3.8b-3.8c), we obtain:

$$\iint\limits_{4\pi\times V} \psi_D(\mathbf{r},\mathbf{\Omega})L_z(\mathbf{r},\mathbf{\Omega})d\Omega dV = \frac{1}{2\pi}\int\limits_R \big(J_z(x,y,Z)\big)^2 + \big(J_z(x,y,0)\big)^2 dA \ . \quad (3.27)$$

This integral is clearly nonnegative; combining these results, we obtain:

$$\begin{aligned}\iint\limits_{4\pi\times\delta R\times Z} &\frac{\mathbf{\Omega}_r\cdot\mathbf{n}_r}{2}\psi_D^2(\mathbf{r},\mathbf{\Omega})\sqrt{1-\mu^2}d\Omega dA dz \\ &+\frac{1}{2\pi}\int\limits_R \big(J_z(x,y,Z)\big)^2 + \big(J_z(x,y,0)\big)^2 dA \\ &+\int\limits_V \left(\Sigma_t(\mathbf{r})-\Sigma_{s0}(\mathbf{r})\right)\int\limits_{4\pi}\psi_D^2(\mathbf{r},\mathbf{\Omega})d\Omega dV \le 0 \ .\end{aligned}$$

Thus, if $\Sigma_t(\mathbf{r}) \ge \Sigma_{s0}(\mathbf{r})$, then $\psi_D(\mathbf{r},\mathbf{\Omega}) = 0$, and the solutions are unique. □

3. *The 2D/1D equation preserves 2D radial transport.* If any problem is considered in which the cross sections and source are independent of z, and the boundary conditions (3.8b) and (3.8c) are replaced by reflecting boundary conditions:

$$J_z(x,y,0) = 0 = J_z(x,y,Z) \ , \quad (x,y) \in R \ ,$$

then ψ is independent of z. In this case, the 2D/1D Eq. (3.1) directly reduces to the 2D Boltzmann equation. Thus, for problems with no axial dependence, the 2D/1D equation and the 2D Boltzmann equation are identical.

4. *The 2D/1D equation preserves 1D axial diffusion.* If any problem is considered in which the cross sections and source are independent of x and y, and the boundary condition (3.8a) is replaced by a reflecting boundary condition, then ψ is independent of x and y. In this case, Eqs. (3.1), (3.8b), and (3.8c) reduce to:

$$L_z(z,\mathbf{\Omega}) + \Sigma_t(z)\psi(z,\mathbf{\Omega}) = S(z,\mathbf{\Omega}) \ , \tag{3.28a}$$

$$\phi(0) + 2J_z(0) = 0 \ , \tag{3.28b}$$

$$\phi(Z) - 2J_z(Z) = 0 \ . \tag{3.28c}$$

Operating on Eq. (3.28a) by $\int(\cdot)d\Omega$, we immediately get

$$\frac{\partial}{\partial z}J_z(z) + \Sigma_t(z)\phi(z) = S_0(z) \ . \tag{3.29}$$

Thus — if either a Fick's law approximation or a transverse leakage that includes the $\mu\phi$ moment is used — for problems with no radial dependence, the 2D/1D equation reduces to the standard 1D axial diffusion equation.

5. *The 2D/1D equation preserves the standard 3D P_1 approximation.* Operating on Eq. (3.1) by

$$\int(\cdot)\,d\Omega \ , \quad \int \Omega_x(\cdot)\,d\Omega \ , \quad \int \Omega_y(\cdot)\,d\Omega \ , \quad \text{and} \quad \int \Omega_z(\cdot)\,d\Omega \ ,$$

we obtain:

$$\frac{\partial}{\partial x}J_x(\mathbf{r}) + \frac{\partial}{\partial y}J_y(\mathbf{r}) + \frac{\partial}{\partial z}J_z(\mathbf{r}) + \Sigma_t(\mathbf{r})\phi(\mathbf{r}) = S_{0,0}(\mathbf{r}) \;, \tag{3.30a}$$

$$\begin{aligned}\frac{\partial}{\partial x}\int \Omega_x^2\psi(\mathbf{r},\boldsymbol{\Omega})d\Omega + \frac{\partial}{\partial y}\int \Omega_x\Omega_y\psi(\mathbf{r},\boldsymbol{\Omega})d\Omega \\ + \int \Omega_x L_z(\mathbf{r},\boldsymbol{\Omega})d\Omega + \Sigma_t(\mathbf{r})J_x(\mathbf{r}) = 0 \;,\end{aligned} \tag{3.30b}$$

$$\begin{aligned}\frac{\partial}{\partial x}\int \Omega_x\Omega_y\psi(\mathbf{r},\boldsymbol{\Omega})\,d\Omega + \frac{\partial}{\partial y}\int \Omega_y^2\psi(\mathbf{r},\boldsymbol{\Omega})\,d\Omega \\ + \int \Omega_y L_z(\mathbf{r},\boldsymbol{\Omega})d\Omega + \Sigma_t(\mathbf{r})J_y(\mathbf{r}) = 0 \;,\end{aligned} \tag{3.30c}$$

$$\begin{aligned}\frac{\partial}{\partial x}\int \Omega_x\Omega_z\psi(\mathbf{r},\boldsymbol{\Omega})\,d\Omega + \frac{\partial}{\partial y}\int \Omega_y\Omega_z\psi(\mathbf{r},\boldsymbol{\Omega})\,d\Omega \\ + \int \Omega_z L_z(\mathbf{r},\boldsymbol{\Omega})d\Omega + \Sigma_t(\mathbf{r})J_y(\mathbf{r}) = 0 \;.\end{aligned} \tag{3.30d}$$

Assuming the standard P_1 approximation for ψ:

$$\psi(\mathbf{r},\boldsymbol{\Omega}) \approx \frac{1}{4\pi}\big(\phi(\mathbf{r}) + 3\boldsymbol{\Omega}\cdot\mathbf{J}(\mathbf{r})\big) \;,$$

Given that all the various approximations that we make to L_z (Eqs. (3.5-3.6)) are anti-symmetric in Ω_x and Ω_y, Eqs. (3.30b) and (3.30c) reduce to

$$\frac{\partial}{\partial x}\frac{\phi}{3} + \Sigma_t J_x = 0 \;, \tag{3.31a}$$

$$\frac{\partial}{\partial y}\frac{\phi}{3} + \Sigma_t J_y = 0 \;. \tag{3.31b}$$

If a Fick's law approximation in the transverse leakage approximation, Eq. (3.30d) is unnecessary. If a transverse leakage that includes the $\mu\phi$ moment is used, Eq. (3.30d) reduces to

$$\frac{\partial}{\partial z}\frac{\phi}{3} + \Sigma_t J_z = 0 \;. \tag{3.31c}$$

For both cases, using Eqs. (3.31a) and (3.31b) to eliminate J_x and J_y from Eq. (3.30a) and either a Fick's law based transverse leakage approximation or Eq.

(3.31c) to eliminate J_z, we obtain the standard diffusion equation. For some higher order leakage approximations (not investigated here), a higher order P_N solution can be preserved rather than diffusion.

The above results show that the 2D/1D equation (i) preserves the correct transport physics in the radial variables x and y, and (ii) uses diffusion physics in the axial variable z, in such a way that (iii) the standard 3D (x, y, z) diffusion approximation is preserved. (Applying the standard asymptotic analysis to Eq. (3.1) also yields the standard diffusion equation.)

These favorable results hold for the "simplest" 2D/1D equation, derived earlier from Eqs. (3.1) and (3.6b). The same results also hold for more complicated 2D/1D equations, obtained using any of equations (3.5) or (3.6) .

3.3 Discretization of the 2D/1D Approximation

An axial discretization for the 2D/1D Eq. (3.1) can be derived by integrating the equation over axial "slices" $z_{k-1/2} < z < z_{k+1/2}$ of width $\Delta_k = z_{k+1/2} - z_{k-1/2}$. Assuming that the cross sections are independent of z on each slice, we define the angular and scalar fluxes:

$$\psi_k(x, y, \mathbf{\Omega}) = \frac{1}{\Delta_k} \int_{z_{k-1/2}}^{z_{k+1/2}} \psi(\mathbf{r}, \mathbf{\Omega}) dz \ , \tag{3.32a}$$

$$\phi_k(x, y) = \frac{1}{\Delta_k} \int_{z_{k-1/2}}^{z_{k+1/2}} \phi(\mathbf{r}) dz = \int \psi_k(x, y, \mathbf{\Omega}) d\Omega \ . \tag{3.32b}$$

The discretization of the axial leakage term clearly depends on the choice of approximation. We define the discretized leakage as:

$$L_{z,k}(x, y, \mathbf{\Omega}) = \frac{1}{\Delta_k} \int_{z_{k-1/2}}^{z_{k+1/2}} L_z(\mathbf{r}, \mathbf{\Omega}) dz = \frac{L_{z,k+1/2}(x, y, \mathbf{\Omega}) - L_{z,k-1/2}(x, y, \mathbf{\Omega})}{\Delta_z} \ , \tag{3.32c}$$

where the exact values of $L_{z,k+1/2}(x,y,\mathbf{\Omega})$ are:

$$L_{z,k+1/2}(x,y,\mathbf{\Omega}) = \mu\psi_{k+1/2}(x,y,\mathbf{\Omega}) \ .$$

The discretized forms of the various approximations to the axial leakage are then:

- The P_1 approximation:

$$L_{z,k+1/2}(x,y,\mathbf{\Omega}) \approx \frac{\mu}{4\pi}\left(\phi_{k+1/2}(x,y) + 3\mathbf{\Omega}\cdot\mathbf{J}_{k+1/2}(x,y)\right) \ . \tag{3.32d}$$

- The diffusion approximation:

$$L_{z,k+1/2}(x,y,\mathbf{\Omega}) \approx \frac{\mu}{4\pi}\left(\phi_{k+1/2}(x,y) + 3\mu J_{z,k+1/2}(x,y)\right) \ . \tag{3.32e}$$

- The quadratic approximation:

$$L_{z,k+1/2}(x,y,\mathbf{\Omega}) \approx \frac{3\mu^2}{4\pi} J_{z,k+1/2}(x,y) \ . \tag{3.32f}$$

- The linear approximation:

$$L_{z,k+1/2}(x,y,\mathbf{\Omega}) \approx \frac{1}{4\pi}\left(J_{z,k+1/2}(x,y) + \mu\phi_{k+1/2}(x,y)\right) \ . \tag{3.32g}$$

- The isotropic approximation:

$$L_{z,k+1/2}(x,y,\mathbf{\Omega}) \approx \frac{J_{z,k+1/2}(x,y)}{4\pi} \ . \tag{3.32h}$$

When these approximations are used with Fick's Law, a finite difference approximation can be used to discretize the derivative of the scalar flux:

$$\begin{aligned} J_{z,k+1/2}(x,y) &\approx -D_{k+1/2}(x,y)\frac{\partial}{\partial z}\phi_{k+1/2}(x,y) \\ J_{z,k+1/2}(x,y) &\approx -D_{k+1/2}(x,y)\frac{\phi_{k+1}(x,y) - \phi_k(x,y)}{\Delta_{k+1/2}} \ , \end{aligned} \tag{3.33a}$$

where:

$$D_{k+1/2}(x,y) = \frac{\Delta_k + \Delta_{k+1}}{\frac{\Delta_k}{D_k} + \frac{\Delta_{k+1}}{D_{k+1}}} \quad , \quad \Delta_{k+1/2} = \frac{1}{2}(\Delta_k + \Delta_{k+1}) \; . \tag{3.33b}$$

Likewise, the scalar flux on the surfaces $\phi_{k+1/2}$ — and cross currents on the surfaces $J_{x,k+1/2}, J_{y,k+1/2}$, for the P_1 approximation — are calculated by a finite difference approximation:

$$\phi_{k+1/2}(x,y) \approx \frac{\phi_{k+1}(x,y)\Delta_{k+1} + \phi_k(x,y)\Delta_k}{\Delta_{k+1} + \Delta_k} \; , \tag{3.33c}$$

$$J_{xy,k+1/2}(x,y) \approx \frac{J_{xy,k+1}(x,y)\Delta_{k+1} + J_{xy,k}(x,y)\Delta_k}{\Delta_{k+1} + \Delta_k} \; . \tag{3.33d}$$

With these definitions, the axially-discretized 2D/1D equation becomes:

$$\left(\Omega_x \frac{\partial}{\partial x} + \Omega_y \frac{\partial}{\partial y} + \Sigma_{t,k}(x,y)\right)\psi_k(x,y,\mathbf{\Omega}) = S_k(x,y,\mathbf{\Omega}) - L_{z,k}(x,y,\mathbf{\Omega}) \; . \tag{3.34}$$

For each $1 \le k \le K$, this is a 2-D transport equation, which is coupled in a simple way (requiring minimal storage and passage of information) to the neighboring slices $k-1$ and $k+1$. The special cases $k = 1$ and K are handled using the boundary conditions (3.8b) and (3.8c) in the standard manner. For example, for $k = K$, Eq. (3.8c) can be written

$$\phi_{K+1/2}(x,y) - 2J_{z,K+1/2}(x,y) = 0 \; .$$

This result, when using Fick's law, is coupled with

$$\begin{aligned} J_{z,K+1/2} &= -\frac{D_K}{\Delta_K/2}\big(\phi_{K+1/2}(x,y) - \phi_K(x,y)\big) \\ &= -\frac{D_{K+1/2}}{\Delta_{K+1/2}}\big(\phi_{K+1}(x,y) - \phi_K(x,y)\big) \; , \end{aligned}$$

to give:

$$-\frac{D_{K+1/2}(x,y)}{\Delta_{K+1/2}}\big(\phi_{K+1}(x,y)-\phi_K(x,y)\big)=\left(\frac{2D_K(x,y)}{\Delta_K+4D_K(x,y)}\right)\phi_K(x,y)\ . \quad (3.35)$$

This result enables the term containing ϕ_{K+1}, in Eq. (3.33a) with $k = K$, to be replaced by an equivalent term containing only D_K, Δ_K, and ϕ_K.

In our numerical simulations, we employed the 2D Method-of-Characteristics (MOC) [17] to discretize the radial and angular variables in Eq. (3.34). The only feature of these discretizations requiring comment is that in DeCART and MPACT, the axial leakage terms Eq. (3.32c) are discretized on a *coarse* radial grid, while the remaining terms are discretized on a *fine* radial grid. Typically, a coarse spatial cell consists of a pin cell (which is about one mean free path in width), and the fine spatial cells resolve the inner structure of a pin cell (and are small fractions of a mean free path in width). In practice, the radially discretized terms in the axial leakage of Eq. (3.33a) are volume-averaged over a coarse cell, and the axial diffusion coefficients $D_{k\pm1/2}$ are homogenized over a coarse cell.

The restriction of the axial leakage terms to coarse mesh scalar fluxes implies that the resulting 2D/1D equation can be parallelized, in such a way that each processor performs sweeps on one slice, and only minimal information (coarse grid scalar fluxes) needs to be passed between processors. (If spatially fine-grid or angularly fine-grid information had to be transmitted between processors, the method would have much less parallel efficiency.)

For highly-scattering homogeneous medium problems in which classic diffusion theory is valid, the axial diffusion coefficients do not need to be radially homogenized, and the prescription $D = 1/3\Sigma_t$ in Eq. (3.33b) is valid. This prescription is used both under valid circumstances in Chapter 4 and approximating circumstances in Chapter 5, and discussed in these numerical results.

3.3.1 Applying a Shape Function

In a heterogeneous lattice problem, the grid upon which the radial transport is solved will resolve the fine structure of the system, whereas the axial diffusion term will apply to larger homogenized regions of the system. Thus, a mapping is required to go from the coarse mesh quantities to the fine mesh. The simplest choice (although incorrect) is a flat mapping, where no shape is given. A more accurate shape can again be derived from the asymptotic theory of Trahan and Larsen [18,19]. An intermediate approximation can be obtained as follows. We consider the axial leakage term before it is approximated:

$$L_z(\mathbf{r},\mathbf{\Omega}) = \mu\frac{\partial}{\partial z}\psi(\mathbf{r},\mathbf{\Omega}) \ .$$

The angular flux within this derivative possesses its complete radial description; as stated above, the axial leakage is treated on a coarser grid. Applying a coarse grid to the problem, $x_j - \Delta_x/2 < x < x_j + \Delta_x/2$ and $y_j - \Delta_y/2 < y < y_j + \Delta_y/2$, then we can define a spatially coarse grid angular flux:

$$\psi_{i,j}(z,\mathbf{\Omega}) = \frac{\iint_{R_{i,j}} \psi(\mathbf{r},\mathbf{\Omega})dxdy}{\iint_{R_{i,j}} dxdy} \ .$$

This can then be used in the leakage description:

$$L_z(\mathbf{r},\mathbf{\Omega}) = \mu\frac{\partial}{\partial z}\left(\psi_{i,j}(z,\mathbf{\Omega})\frac{\psi(\mathbf{r},\mathbf{\Omega})}{\psi_{i,j}(z,\mathbf{\Omega})}\right) \ .$$

This ratio of the fine to coarse radial cell angular flux is the shape function of interest. We denote this as:

$$V_{i,j}(\mathbf{r},\mathbf{\Omega}) = \frac{\psi(\mathbf{r},\mathbf{\Omega})}{\psi_{i,j}(z,\mathbf{\Omega})} \ .$$

Two approximations can be made to this shape function: (i) a spatial approximation in the z-direction and (ii) an angular approximation. If we integrate this axially

to get the discretized leakage, we obtain:

$$L_{z,k}(x,y,\mathbf{\Omega}) = \mu \frac{\psi_{i,j,k+1/2}(x,y,\mathbf{\Omega})V_{i,j,k+1/2}(x,y,\mathbf{\Omega}) - \psi_{i,j,k-1/2}(x,y,\mathbf{\Omega})V_{i,j,k-1/2}(x,y,\mathbf{\Omega})}{\Delta_k} ,$$
$$V_{i,j,k+1/2}(x,y,\mathbf{\Omega}) = \frac{\psi_{k+1/2}(x,y,\mathbf{\Omega})}{\psi_{i,j,k+1/2}(\mathbf{\Omega})} .$$

Alternatively, we can assume that the shapes functions at the top and bottom of the plane are well approximated by a plane average shape function:

$$L_{z,k}(x,y,\mathbf{\Omega}) = \mu \frac{\psi_{i,j,k+1/2}(x,y,\mathbf{\Omega}) - \psi_{i,j,k-1/2}(x,y,\mathbf{\Omega})}{\Delta_k} V_{i,j,k}(x,y,\mathbf{\Omega}) ,$$
$$V_{i,j,k}(x,y,\mathbf{\Omega}) = \frac{\psi_k(x,y,\mathbf{\Omega})}{\psi_{i,j,k}(\mathbf{\Omega})} .$$

This is the kind of axial approximation that we use in this work. There are many possible angular approximations that we can make of the shape function; for example a smaller subset of discrete angles could be used, or spherical harmonic expansions could be made of the coarse and fine grid angular flux in the numerator and denominator. In this work, we consider the simplest (isotropic) approximation:

$$V_{i,j,k}(x,y,\mathbf{\Omega}) \approx \frac{\phi_k(x,y)}{\phi_{i,j,k}} .$$

3.4 Iterative Solution Methods for the 2D/1D Approximation

It is possible to conceive of many different iteration schemes for the 2D/1D equation. Here, we consider the simple "source iteration" scheme in which the RHS is updated after each transport sweep. Another straightforward method employs the well known CMFD acceleration scheme [16] and gives improved convergence rates. Both of these methods are considered below.

3.4.1 Source Iteration of the 2D/1D Approximation

Next, we consider what is likely the simplest possible iteration scheme for solving Eq. (3.34) that can be made stable for all $\Delta_z > 0$. We consider a simple 2D sweep on each slice to update the scalar flux:

$$\left(\Omega_x \frac{\partial}{\partial x} + \Omega_y \frac{\partial}{\partial y} + \Sigma_{t,k}(x,y)\right) \psi_k^{(\ell+1/2)}(x,y,\mathbf{\Omega}) = S_k^{(\ell)}(x,y,\mathbf{\Omega}) - L_{z,k}^{(\ell)}(x,y,\mathbf{\Omega}) \;, \tag{3.36a}$$

$$\phi_k^{(\ell+1/2)}(x,y) = \int \psi_k^{(\ell+1/2)}(x,y,\mathbf{\Omega}')d\Omega' \;, \tag{3.36b}$$

followed by a (nonstandard) relaxation step to define the end-of-iteration scalar flux:

$$\phi_k^{(\ell+1)}(x,y) = \theta\phi_k^{(\ell+1/2)}(x,y) + (1-\theta)\phi_k^{(\ell)}(x,y) \;. \tag{3.36c}$$

The source term $S_k^{(\ell+1)}(x,y,\mathbf{\Omega})$ and the axial leakage term $L_{z,k}^{(\ell+1)}(x,y,\mathbf{\Omega})$ for the next iteration are defined as they would for their non-iterative counterparts, but with the scalar flux replaced by the end-of-iteration scalar flux $\phi_k^{(\ell+1)}(x,y)$. In analyzing this method, we do not treat Eq. (3.36) with any angular or radial spatial discretizations; our experience is that although these choices affect the accuracy of the discrete solution, they do not significantly affect the iterative performance in converging to this solution. The relaxation parameter θ in Eq. (3.36c) is to be determined; if $\theta = 1$, the method defined by Eqs. (3.36) is basically Source Iteration (and is very similar, if not identical, to the original iteration method encoded in DeCART). We note that in each iteration, the numerical solutions in slice k are directly coupled only to the numerical solutions in the neighboring slices $k+1$ and $k-1$. Therefore, many iterations may be required for the numerical fluxes in all the axial slices $1 \leq k \leq K$ to sufficiently "communicate."

3.4.2 CMFD Acceleration of the 2D/1D Approximation

We apply CMFD acceleration to the 2D/1D approximation to both (i) more rapidly converge the transport solution, and (ii) couple the axial planes to more than their nearest neighbor by solving an axial diffusion equation (embedded within the CMFD method). This iterative scheme begins in the same manner as source iteration with both a transport sweep, Eq. (3.36a), and an angular integral of the angular flux to obtain the scalar flux, Eq. (3.36b); however, some steps are inserted before the relaxation step. First, we define the post-sweep radial currents:

$$J_x^{(\ell+1/2)}(x,y) = \int\limits_{4\pi} \Omega_x \psi_k^{(\ell+1/2)}(x,y,\mathbf{\Omega}) d\Omega \ , \tag{3.37a}$$

$$J_y^{(\ell+1/2)}(x,y) = \int\limits_{4\pi} \Omega_y \psi_k^{(\ell+1/2)}(x,y,\mathbf{\Omega}) d\Omega \ . \tag{3.37b}$$

Also, we define the non-linear, current consistency terms:

$$\hat{D}_{x,k}^{(\ell+1/2)}(x,y) = \frac{J_{x,k}^{(\ell+1/2)}(x,y) + D_k(x,y)\frac{\partial}{\partial x}\phi_k^{(\ell+1/2)}}{\phi_k^{(\ell+1/2)}} \ , \tag{3.37c}$$

$$\hat{D}_{y,k}^{(\ell+1/2)}(x,y) = \frac{J_{y,k}^{(\ell+1/2)}(x,y) + D_k(x,y)\frac{\partial}{\partial y}\phi_k^{(\ell+1/2)}}{\phi_k^{(\ell+1/2)}} \ . \tag{3.37d}$$

Using these definitions, we can define the relation between the updated radial current and updated scalar flux:

$$J_{x,k}^{(\ell+3/4)}(x,y) = \left(-D_k(x,y)\frac{\partial}{\partial x} + \hat{D}_{x,k}^{(\ell+1/2)}(x,y)\right)\phi_k^{(\ell+3/4)} \ , \tag{3.37e}$$

$$J_{y,k}^{(\ell+3/4)}(x,y) = \left(-D_k(x,y)\frac{\partial}{\partial y} + \hat{D}_{y,k}^{(\ell+1/2)}(x,y)\right)\phi_k^{(\ell+3/4)} \ . \tag{3.37f}$$

If we are using a finite difference axial approximation, we define the relation between the update axial current and scalar flux,

$$J_{z,k+1/2}^{(\ell+3/4)}(x,y) = -D_{k+1/2}(x,y)\frac{\phi_{k+1}^{(\ell+3/4)}(x,y) - \phi_k^{(\ell+3/4)}(x,y)}{\Delta_{k+1/2}} \ . \tag{3.37g}$$

We will define the axial current update when using nodal methods in the next section. To complete the CMFD acceleration, we define the update balance equation:

$$\frac{\partial}{\partial x}J_{x,k}^{(\ell+3/4)}(x,y)+\frac{\partial}{\partial y}J_{y,k}^{(\ell+3/4)}(x,y)+\frac{J_{z,k+1/2}^{(\ell+3/4)}(x,y)-J_{z,k-1/2}^{(\ell+3/4)}(x,y)}{\Delta_k} \tag{3.37h}$$

$$+\Sigma_{a0,k}(x,y)\phi_k^{(\ell+3/4)}(x,y)=S_{f0,k}(x,y)\ , \tag{3.37i}$$

where,

$$\Sigma_{a0,k}(x,y)=\Sigma_{t,k}(x,y)-\Sigma_{s0,k}(x,y)\ ,$$

$$S_{f0,k}(x,y)=\frac{1}{\Delta_k}\int_{z_{k-1/2}}^{z_{k+1/2}}\int_{4\pi}S_f(\mathbf{r},\mathbf{\Omega})d\Omega dz\ .$$

Finally, to complete the overall iterative scheme, we define the post CMFD relaxation:

$$\phi_k^{(\ell+1)}(x,y)=\theta\phi_k^{(\ell+3/4)}(x,y)+(1-\theta)\phi_k^{(\ell)}(x,y)\ . \tag{3.37j}$$

Radially, the CMFD acceleration preserves the relations between the radial currents and the scalar flux produced by the transport equation; whereas axially, it calculates values for the axial current using Fick's law. The (nonstandard) relaxation step is again used to provide a means to stabilize this method.

Linearization of CMFD

Before a Fourier analysis can be applied to this method, it must first be linearized. A linear update term is defined for the scalar flux for simplicity:

$$\delta\phi_k^{(\ell+1/2)}(x,y)=\phi_k^{(\ell+3/4)}(x,y)-\phi_k^{(\ell+1/2)}(x,y)\ . \tag{3.38}$$

We linearize the method by changing the definition of $\hat{D}$ to be a measurement of the absolute error of Fick's law rather than a relative error to the scalar flux:

$$\hat{D}_{x,k}^{(\ell+1/2)}(x,y) = J_{x,k}^{(\ell+1/2)}(x,y) + D_k(x,y)\frac{\partial}{\partial x}\phi_k^{(\ell+1/2)}(x,y) \ ,$$
$$\hat{D}_{y,k}^{(\ell+1/2)}(x,y) = J_{y,k}^{(\ell+1/2)}(x,y) + D_k(x,y)\frac{\partial}{\partial y}\phi_k^{(\ell+1/2)}(x,y) \ .$$

This results in the update of the currents to be equal to the updates of the Fick's law approximation:

$$J_{x,k}^{(\ell+3/4)}(x,y) - J_{x,k}^{(\ell+1/2)}(x,y) = -D_k(x,y)\frac{\partial}{\partial x}\delta\phi_k^{(\ell+1/2)}(x,y) \ , \tag{3.39a}$$
$$J_{y,k}^{(\ell+3/4)}(x,y) - J_{y,k}^{(\ell+1/2)}(x,y) = -D_k(x,y)\frac{\partial}{\partial y}\delta\phi_k^{(\ell+1/2)}(x,y) \ . \tag{3.39b}$$

Integrating Eq. (3.36a) over all angles yields the intermediate balance equation for the sweep:

$$\begin{aligned}\frac{\partial}{\partial x}J_{x,k}^{(\ell+1/2)}(x,y) + \frac{\partial}{\partial y}J_{y,k}^{(\ell+1/2)}(x,y) + \Sigma_{t,k}(x,y)\phi_k^{(\ell+1/2)}(x,y) \\ = \Sigma_{s0,k}(x,y)\phi_k^{(\ell)}(x,y) + S_{f0,k}(x,y) - L_{z0,k}^{(\ell)}(x,y) \ .\end{aligned} \tag{3.40}$$

By the requirement of Eq. (3.3), the zeroth moment of $L_{z,k}$ must be

$$L_{z0,k}^{(\ell)}(x,y) = \frac{J_{z,k+1/2}^{(\ell)}(x,y) - J_{z,k-1/2}^{(\ell)}(x,y)}{\Delta_k} \ . \tag{3.41}$$

The axial currents of this equation can be estimated by Fick's law in Eq. (3.33a) consistently with the CMFD acceleration. Subtracting Eq. (3.40) from Eq. (3.37h)

yields:

$$\frac{\partial}{\partial x}\Big(J_{x,k}^{(\ell+3/4)}(x,y)-J_{x,k}^{(\ell+1/2)}(x,y)\Big)+\frac{\partial}{\partial y}\Big(J_{y,k}^{(\ell+3/4)}(x,y)-J_{y,k}^{(\ell+1/2)}(x,y)\Big)$$
$$+\frac{J_{z,k+1/2}^{(\ell+3/4)}(x,y)-J_{z,k-1/2}^{(\ell+3/4)}(x,y)}{\Delta_k}+\Sigma_{t,k}(x,y)\Big(\phi_k^{(\ell+3/4)}(x,y)-\phi_k^{(\ell+1/2)}(x,y)\Big)$$
$$=\Sigma_{s0,k}(x,y)\Big(\phi_k^{(\ell+3/4)}(x,y)-\phi_k^{(\ell)}(x,y)\Big)+\frac{J_{z,k+1/2}^{(\ell)}(x,y)-J_{z,k-1/2}^{(\ell)}(x,y)}{\Delta_k}\ .$$

Applying Eqs. (3.38),(3.39), and (3.33a) to this equation, and rearranging yields:

$$\begin{aligned}
&-D_k(x,y)\left(\frac{\partial^2}{\partial x^2}+\frac{\partial^2}{\partial y^2}\right)\delta\phi_k^{(\ell+1/2)}(x,y)\\
&-D_{k+1/2}(x,y)\frac{\delta\phi_{k+1}^{(\ell+1/2)}(x,y)-\delta\phi_k^{(\ell+1/2)}(x,y)}{\Delta_k\Delta_{k+1/2}}\\
&+D_{k-1/2}(x,y)\frac{\delta\phi_k^{(\ell+1/2)}(x,y)-\delta\phi_{k-1}^{(\ell+1/2)}(x,y)}{\Delta_k\Delta_{k-1/2}}\\
&+\Sigma_{a0,k}(x,y)\delta\phi_k^{(\ell+1/2)}(x,y)=\Sigma_{s0,k}(x,y)\Big(\phi_k^{(\ell+1/2)}(x,y)-\phi_k^{(\ell)}(x,y)\Big)\\
&\qquad+D_{k+1/2}(x,y)\frac{\phi_{k+1}^{(\ell+1/2)}(x,y)-\phi_k^{(\ell+1/2)}(x,y)}{\Delta_k\Delta_{k+1/2}}\\
&\qquad-D_{k-1/2}(x,y)\frac{\phi_k^{(\ell+1/2)}(x,y)-\phi_{k-1}^{(\ell+1/2)}(x,y)}{\Delta_k\Delta_{k-1/2}}\\
&\qquad-D_{k+1/2}(x,y)\frac{\phi_{k+1}^{(\ell)}(x,y)-\phi_k^{(\ell)}(x,y)}{\Delta_k\Delta_{k+1/2}}\\
&\qquad+D_{k-1/2}(x,y)\frac{\phi_k^{(\ell)}(x,y)-\phi_{k-1}^{(\ell)}(x,y)}{\Delta_k\Delta_{k-1/2}}\ .
\end{aligned}\tag{3.42}$$

The update equation becomes:

$$\phi_k^{(\ell+1)}(x,y)=\theta\Big(\phi_k^{(\ell+1/2)}(x,y)+\delta\phi_k^{(\ell+1/2)}\Big)+(1-\theta)\phi_k^{(\ell)}(x,y)\ .\tag{3.43}$$

3.4.3 Inclusion of a Nodal Diffusion Axial Solver

As the 2D/1D method is often intended to be used with thick axial planes, the accuracy of the axial diffusion calculation can suffer when it is treated with a finite difference method. Instead, an additional nodal diffusion sweep can be included between the transport sweep and the CMFD update. To form the 1D nodal diffusion equation that we will solve, we consider again the 2D/1D equation (Eq. (3.1)),

$$\sqrt{1-\mu^2}\mathbf{\Omega}_r \cdot \boldsymbol{\nabla}_r \psi(\mathbf{r},\mathbf{\Omega}) + \Sigma_t(\mathbf{r})\psi(\mathbf{r},\mathbf{\Omega}) = S(\mathbf{r},\mathbf{\Omega}) - L_z(\mathbf{r},\mathbf{\Omega}) \; .$$

First, we integrate this equation over all angles. Because of the balance restriction we imposed in Eq. (3.3), for all transverse leakage approximations we consider, we obtain:

$$\frac{\partial J_x(\mathbf{r})}{\partial x} + \frac{\partial J_y(\mathbf{r})}{\partial y} + \Sigma_a \phi(\mathbf{r}) = S_0(\mathbf{r}) - \frac{\partial J_z(\mathbf{r})}{\partial z} \; ,$$

or

$$\frac{\partial J_z(\mathbf{r})}{\partial z} + \Sigma_a \phi(\mathbf{r}) = S_0(\mathbf{r}) - \left[\frac{\partial J_x(\mathbf{r})}{\partial x} + \frac{\partial J_y(\mathbf{r})}{\partial y}\right] \; . \tag{3.44}$$

By consistently using the Fick's law approximation for the axial current, we obtain a 1D axial diffusion equation consistent with our original 2D/1D equation.

Using the 2-node SANM style nodal calculation of Section 2.3.3, the source term definitions are:

$$S_{0,j}^{(\ell)} \rightarrow S_{0,k}^{(\ell+1/2)}(x,y) = -\frac{\partial J_{x,k}^{(\ell+1/2)}}{\partial x} - \frac{\partial J_{y,k}^{(\ell+1/2)}}{\partial y} \; , \tag{3.45a}$$

$$S_{1,j}^{(\ell)} \rightarrow S_{1,k}^{(\ell+1/2)}(x,y) = \frac{1}{4}\left(S_{0,k+1}^{(\ell+1/2)} - S_{0,k-1}^{(\ell+1/2)}\right) \; , \tag{3.45b}$$

$$S_{2,j}^{(\ell)} \rightarrow S_{2,k}^{(\ell+1/2)}(x,y) = \frac{1}{12}\left(S_{0,k+1}^{(\ell+1/2)} - 2S_{0,k}^{(\ell+1/2)} + S_{0,k-1}^{(\ell+1/2)}\right) \; , \tag{3.45c}$$

$$S_{3,j}^{(\ell)} = 0 \; , \tag{3.45d}$$

$$S_{4,j}^{(\ell)} = 0 \; . \tag{3.45e}$$

The equations for the nodal terms and inter-node current remain the same as they were in Section 2.3.3, but are relabeled to match the 3D labeling of the 2D/1D

method:

$$\begin{aligned}
\bar{\phi}_j^{(\ell)} &\rightarrow \phi_k^{(\ell+1/2)}(x,y) \\
\phi_{n,j}^{(\ell+1/2)} &\rightarrow \phi_{n,k}^{(\ell+1/2)}(x,y) \\
A_j^{(\ell+1/2)} &\rightarrow A_k^{(\ell+1/2)}(x,y) \\
B_j^{(\ell+1/2)} &\rightarrow B_k^{(\ell+1/2)}(x,y) \\
J_{j+1/2}^{(\ell+1/2)} &\rightarrow J_{z,k+1/2}^{(\ell+1/2)}(x,y) \\
D_j &\rightarrow D_k(x,y) \\
\Delta_j &\rightarrow \Delta_k(x,y) \\
\beta_j &\rightarrow \beta_k(x,y) \\
\Sigma_{r,j} &\rightarrow \Sigma_{r,k}(x,y) \\
\Sigma_{D,j} &\rightarrow \Sigma_{D,k}(x,y) \\
\kappa_j &\rightarrow \kappa_k(x,y)
\end{aligned}$$

Finally, the CMFD calculation is different, as a current coupling term is used for the axial diffusion, and an additional update/relaxation equation exists for the inter-plane axial current:

$$\hat{D}_{z,k+1/2}^{(\ell+1/2)} = \frac{J_{z,k+1/2}^{(\ell+1/2)}(x,y) + D_{k+1/2}(x,y)\frac{\phi_{k+1}^{(\ell+1/2)} - \phi_k^{(\ell+1/2)}}{\Delta_{k+1/2}}}{\phi_{k+1}^{(\ell+1/2)} + \phi_k^{(\ell+1/2)}} \,, \tag{3.46}$$

$$\begin{aligned}
J_{z,k}^{(\ell+3/4)}(x,y) =& -D_{k+1/2}(x,y)\frac{\phi_{k+1}^{(\ell+3/4)} - \phi_k^{(\ell+3/4)}}{\Delta_{k+1/2}} \\
&+ \hat{D}_{y,k}^{(\ell+1/2)}(x,y)\left(\phi_{k+1}^{(\ell+3/4)} + \phi_k^{(\ell+3/4)}\right) \,,
\end{aligned} \tag{3.47}$$

$$J_{z,k+1/2}^{(\ell+1)} = \theta J_{z,k+1/2}^{(\ell+3/4)} + (1-\theta) J_{z,k+1/2}^{(\ell)} \,. \tag{3.48}$$

For the application of Fourier analysis to be done, the linearized version of this

is:

$$
\begin{aligned}
&-D_k(x,y)\left(\frac{\partial^2}{\partial x^2}+\frac{\partial^2}{\partial y^2}\right)\delta\phi_k^{(\ell+1/2)}(x,y)\\
&\quad -D_{k+1/2}(x,y)\frac{\delta\phi_{k+1}^{(\ell+1/2)}(x,y)-\delta\phi_k^{(\ell+1/2)}(x,y)}{\Delta_k\Delta_{k+1/2}}\\
&\qquad +D_{k-1/2}(x,y)\frac{\delta\phi_k^{(\ell+1/2)}(x,y)-\delta\phi_{k-1}^{(\ell+1/2)}(x,y)}{\Delta_k\Delta_{k-1/2}}\\
&\qquad +\Sigma_{a0,k}(x,y)\delta\phi_k^{(\ell+1/2)}(x,y)=\Sigma_{s0,k}(x,y)\left(\phi_k^{(\ell+1/2)}(x,y)-\phi_k^{(\ell)}(x,y)\right)\\
&\qquad -\left(\frac{J_{z,k+1/2}^{(\ell+1/2)}(x,y)-J_{z,k-1/2}^{(\ell+1/2)}(x,y)}{\Delta_k}-\frac{J_{z,k+1/2}^{(\ell)}(x,y)-J_{z,k-1/2}^{(\ell)}(x,y)}{\Delta_k}\right),
\end{aligned}
\tag{3.49}
$$

$$
\begin{aligned}
J_{z,k+1/2}^{(\ell+1)}=&\theta\left(J_{z,k+1/2}^{(\ell+1/2)}-\frac{D_{k+1/2}(x,y)}{\Delta_{k+1/2}}\left(\delta\phi_{k+1}^{(\ell+1/2)}(x,y)-\delta\phi_k^{(\ell+1/2)}(x,y)\right)\right)\\
&+(1-\theta)J_{z,k+1/2}^{(\ell)}\,.
\end{aligned}
\tag{3.50}
$$

3.4.4 Transverse Leakage Splitting

A practical difficulty occurs when using the 2D/1D approximation with CMFD acceleration. As CMFD is a non-linear method, it is sensitive to the presence of negative values (particularly non-positive scalar fluxes). With the 2D/1D approximation, nothing precludes the leakage term appearing on the right hand side of the transport equation from being negative. If the magnitude of such a leakage is sufficiently large, the transport sweep can potentially generate angular and scalar fluxes that are non-positive. To prevent this from occurring, a technique has been adopted in the MPACT code, whereby the source is "corrected", to make the right hand side of the transport equation non-negative while artificially increasing the collision cross section non-linearly. Compared to the transport sweep of Eq. (3.36a), the following

is used:

$$\left(\Omega_x\frac{\partial}{\partial x}+\Omega_y\frac{\partial}{\partial y}+\Sigma_{t,k}(x,y)+\frac{\tilde{L}^{(\ell)}_{z,k}(x,y)}{\phi^{(\ell)}_k(x,y)}\right)\psi^{(\ell+1/2)}_k(x,y,\mathbf{\Omega}) \\ = S^{(\ell)}_k(x,y,\mathbf{\Omega})-L^{(\ell)}_{z,k}(x,y,\mathbf{\Omega})+\frac{\tilde{L}^{(\ell)}_{z,k}(x,y)}{4\pi}\ . \tag{3.51}$$

It is not a preferable choice to induce this splitting technique, as all moments of the angular flux other than the scalar flux are perturbed; however, some practical problems require this choice for a convergent solution with CMFD. This splitting could be done more carefully by using the old angular flux as the scaling parameter (rather than the scalar flux), but this would result in a computational burden in both storage (storing these old angular fluxes) and calculation (the MOC method is well optimized for an isotropic collision term). The value $\tilde{L}^{(\ell)}_{z,k}(x,y)$ is non-negative and chosen such that,

$$S^{(\ell)}_k(x,y,\mathbf{\Omega})-L^{(\ell)}_{z,k}(x,y,\mathbf{\Omega})+\frac{\tilde{L}^{(\ell)}_{z,k}(x,y)}{4\pi}\geq 0\ . \tag{3.52}$$

The calculation of $\tilde{L}^{(\ell)}_{z,k}(x,y)$ varies with the 2D/1D leakage approximation, but is never more complicated than an optimization problem. The values for each approximation method follow; in these equations, the finite difference derivatives are given by:

$$\mathrm{D}^{(\ell)}_{0,k}(x,y)=\frac{\phi^{(\ell)}_{k+1/2}(x,y)-\phi^{(\ell)}_{k-1/2}(x,y)}{\Delta_k}\ ,$$
$$\mathrm{D}^{(\ell)}_{z,k}(x,y)=\frac{J^{(\ell)}_{z,k+1/2}(x,y)-J^{(\ell)}_{z,k-1/2}(x,y)}{\Delta_k}\ ,$$
$$\mathrm{D}^{(\ell)}_{x,k}(x,y)=\frac{J^{(\ell)}_{x,k+1/2}(x,y)-J^{(\ell)}_{x,k-1/2}(x,y)}{\Delta_k}\ ,$$
$$\mathrm{D}^{(\ell)}_{y,k}(x,y)=\frac{J^{(\ell)}_{y,k+1/2}(x,y)-J^{(\ell)}_{y,k-1/2}(x,y)}{\Delta_k}\ ,$$
$$\mathrm{D}^{(\ell)}_{r,k}(x,y)=\sqrt{\left(\mathrm{D}^{(\ell)}_{x,k}(x,y)\right)^2+\left(\mathrm{D}^{(\ell)}_{y,k}(x,y)\right)^2}\ .$$

- The "correction" term for the isotropic leakage is simply,

$$\tilde{L}_{z,k}^{(\ell)}(x,y) = \mathrm{D}_{z,k}^{(\ell)}(x,y) - S_{0,k}^{(\ell)}(x,y) \ . \tag{3.53}$$

- For the linear leakage, we use:

$$\tilde{L}_{z,k}^{(\ell)}(x,y) = \mathrm{D}_{z,k}^{(\ell)}(x,y) + \left|\mathrm{D}_{0,k}^{(\ell)}(x,y)\right| - S_{0,k}^{(\ell)}(x,y) \ . \tag{3.54}$$

- For the quadratic leakage, we use:

$$\tilde{L}_{z,k}^{(\ell)}(x,y) = 3\mathrm{D}_{z,k}^{(\ell)}(x,y) - S_{0,k}^{(\ell)}(x,y) \ . \tag{3.55}$$

- For the diffusion leakage, a non-trivial optimization problem occurs. The "correction" term for the bounds of the polar cosine domain, $\mu = \pm 1$, is,

$$\tilde{L}_{z,k}^{(\ell)}(x,y) = 3\mathrm{D}_{z,k}^{(\ell)}(x,y) + \left|\mathrm{D}_{0,k}^{(\ell)}(x,y)\right| - S_{0,k}^{(\ell)}(x,y) \ . \tag{3.56}$$

  This will be the "correction" term if the leakage is concave down with respect to μ; however, if it is concave up ($\mathrm{D}_{z,k}^{(\ell)}(x,y) > 0$), the maximum leakage may occur within the domain of μ. The extremum value of μ is given by:

$$\breve{\mu} = -\frac{\mathrm{D}_{0,k}^{(\ell)}(x,y)}{6\mathrm{D}_{z,k}^{(\ell)}(x,y)} \ .$$

  If this value lies within the domain of μ, then another "correction" to consider is,

$$\tilde{L}_{z,k}^{(\ell)}(x,y) = 3\breve{\mu}^2\mathrm{D}_{z,k}^{(\ell)}(x,y) - S_{0,k}^{(\ell)}(x,y) \ . \tag{3.57}$$

- Finally, for the P1 leakage, a more complicated optimization problem occurs. The exact maximum leakage cannot be found due to the presence of the cross-currents with the polar dependence $\mu\sqrt{1-\mu^2}$. For the purpose of estimating

the maximum leakage, this polar dependence is instead approximated as:

$$\mu\sqrt{1-\mu^2} \approx \begin{cases} -0.5 & -1 \leq \mu \leq -0.5 \\ \mu & -0.5 \leq \mu \leq 0.5 \\ 0.5 & 0.5 \leq \mu \leq 1 \end{cases} .$$

Maximizing over the azimuthal angle is straightforward, resulting in:

$$\left| \mathrm{D}_{x,k}^{(\ell)}(x,y)\cos\alpha + \mathrm{D}_{y,k}^{(\ell)}(x,y)\sin\alpha \right| \leq \mathrm{D}_{r,k}^{(\ell)}(x,y) \ .$$

The "correction" leakage for the bounds of the polar cosine domain, $\mu = \pm 1$, is:

$$\tilde{L}_{z,k}^{(\ell)}(x,y) = 3\mathrm{D}_{z,k}^{(\ell)}(x,y) + \left|\mathrm{D}_{0,k}^{(\ell)}(x,y)\right| + \frac{3}{2}\mathrm{D}_{r,k}^{(\ell)}(x,y) - S_{0,k}^{(\ell)}(x,y) \ . \tag{3.58}$$

Additionally, the "correction" leakage on the kink in the approximating function, $\mu = \pm 0.5$ is:

$$\tilde{L}_{z,k}^{(\ell)}(x,y) = \frac{3}{4}\mathrm{D}_{z,k}^{(\ell)}(x,y) + \frac{1}{2}\left|\mathrm{D}_{0,k}^{(\ell)}(x,y)\right| + \frac{3}{2}\mathrm{D}_{r,k}^{(\ell)}(x,y) - S_{0,k}^{(\ell)}(x,y) \ . \tag{3.59}$$

If an extremum lies within the linear portion of the approximating function, then it will occur at:

$$\breve{\mu} = -\frac{\mathrm{D}_{0,k}^{(\ell)}(x,y)}{6\mathrm{D}_{z,k}^{(\ell)}(x,y)} \left(1 + \frac{3\mathrm{D}_{r,k}^{(\ell)}(x,y)}{\left|\mathrm{D}_{0,k}^{(\ell)}(x,y)\right|} \right) \ ,$$

or, if $\mathrm{D}_{0,k}^{(\ell)}(x,y) = 0$,

$$\breve{\mu} = \pm\frac{\mathrm{D}_{r,k}^{(\ell)}(x,y)}{2\mathrm{D}_{z,k}^{(\ell)}(x,y)} \ ,$$

with value:

$$\tilde{L}_{z,k}^{(\ell)}(x,y) = 3\breve{\mu}^2\mathrm{D}_{z,k}^{(\ell)}(x,y) - S_{0,k}^{(\ell)}(x,y) \ . \tag{3.60}$$

If an extemum lies within either of the flat portions of the approximating func-

tion, then it will occur at:

$$\breve{\mu} = -\frac{\mathrm{D}_{0,k}^{(\ell)}(x,y)}{6\mathrm{D}_{z,k}^{(\ell)}(x,y)}$$

$$\tilde{L}_{z,k}^{(\ell)}(x,y) = 3\breve{\mu}^2\mathrm{D}_{z,k}^{(\ell)}(x,y) + \frac{3}{2}\mathrm{D}_{r,k}^{(\ell)}(x,y) - S_{0,k}^{(\ell)}(x,y)\ . \tag{3.61}$$

By using these axial leakage splitting techniques, we can prevent negative sources in the transport sweep, which could lead to negative scalar fluxes. This prevents stability issues in the non-linear CMFD acceleration scheme that can arise from negative scalar fluxes.

3.5 Chapter Summary

In this chapter, we have defined the 2D/1D equation and several different axial leakage approximations. We have discussed some aspects of the radial 2D transport equation and the axial diffusion equation. We have discussed some of the properties of the 2D/1D approximation. We have discretized this method and developed iterative methods to apply to it. Finally, we described the process of transverse leakage splitting to improve the stability of non-linear acceleration.

In the next chapter, we apply Fourier analysis to the various iteration schemes that we have developed. This analysis will allow us to predict the optimal under-relaxation factor for efficient convergence. We test these predictions with numerical estimates of the spectral radius with and without under-relaxation. We also consider the accuracy of the method by comparing it to 3D MOC and diffusion solutions of a nearly classically diffusive problem. Finally, we provide motivation for the development of accurate shape functions.

Chapter 4

Analysis

4.1 Efficiency and Stability

Given that the greatest deficiency of the 2D/1D method in DeCART is stability, it is of utmost importance that we ensure that the 2D/1D method used in MPACT is as stable and efficient as possible. We do this theoretically using Fourier analysis and then numerically to confirm the analysis. Uniquely, we also use the results of the Fourier analysis to define the relaxation factor to optimize the convergence of the numerical results.

4.1.1 Fourier Analysis of Source Iteration 2D/1D

In Section 3.4, we described several iterative methods for solving the 2D/1D equations. We now Fourier analyze each transverse leakage approximation and solution method.

Isotropic Axial Leakage

The isotropic approximation is considered first, using $D = 1/3\Sigma_t$:

$$L_{z,k}^{(\ell)}(x,y,\mathbf{\Omega}) \approx -\frac{1}{4\pi\Delta_k}\left(D_{k+1/2}(x,y)\frac{\phi_{k+1}^{(\ell)}(x,y)-\phi_k^{(\ell)}(x,y)}{\Delta_{k+1/2}} - D_{k-1/2}(x,y)\frac{\phi_k^{(\ell)}(x,y)-\phi_{k-1}^{(\ell)}(x,y)}{\Delta_{k-1/2}}\right) .$$

For an infinite, homogeneous medium with uniform $\Delta_k = \Delta_z$, the standard Fourier ansatz is:

$$S_f(\mathbf{r}) = 0 \ , \tag{4.1a}$$

$$\phi_k^{(\ell)}(\mathbf{r}_k) = \omega^\ell e^{i\Sigma_t(\boldsymbol{\lambda}\cdot\mathbf{r}_k)} \ , \tag{4.1b}$$

$$\psi_k^{(\ell+1/2)}(\mathbf{r}_k,\mathbf{\Omega}) = \omega^\ell \tilde{\psi}(\boldsymbol{\lambda},\mathbf{\Omega}) e^{i\Sigma_t(\boldsymbol{\lambda}\cdot\mathbf{r}_k)} \ , \tag{4.1c}$$

$$\phi_k^{(\ell+1/2)}(\mathbf{r}_k) = \omega^\ell \tilde{\phi}(\boldsymbol{\lambda}) e^{i\Sigma_t(\boldsymbol{\lambda}\cdot\mathbf{r}_k)} \ , \tag{4.1d}$$

where $\boldsymbol{\lambda} = (\lambda_x, \lambda_y, \lambda_z)$ is an arbitrary fixed 3-vector. Introducing Eqs. (4.1) into (3.36), and neglecting anisotropic scattering, we easily obtain

$$\Big(i\big(\Omega_x\lambda_x + \Omega_y\lambda_y\big) + 1\Big)\tilde{\psi}(\boldsymbol{\lambda},\mathbf{\Omega}) = \frac{1}{4\pi}\left(c - \frac{1}{3}\Lambda_z^2\right) \ , \tag{4.2a}$$

$$\tilde{\phi}(\boldsymbol{\lambda}) = \int \tilde{\psi}(\boldsymbol{\lambda},\mathbf{\Omega})\, d\Omega \ , \tag{4.2b}$$

$$\omega = \theta\tilde{\phi}(\boldsymbol{\lambda}) + 1 - \theta \ , \tag{4.2c}$$

where

$$\Lambda_z = \Lambda_z(\lambda_z;\Sigma_t\Delta_z) = \frac{\sin(\lambda_z\Sigma_t\Delta_z/2)}{\Sigma_t\Delta_z/2} \ .$$

Introducing Eq. (4.2a) into Eq. (4.2b), we get

$$\tilde{\phi}(\boldsymbol{\lambda}) = \left(c - \frac{1}{3}\Lambda_z^2\right) I_0(\lambda_r) \ , \tag{4.3}$$

where $c = \Sigma_s/\Sigma_t$ is the scattering ratio, and

$$\begin{aligned} I_0(\lambda_r) &= \frac{1}{4\pi} \int\limits_{4\pi} \frac{d\Omega}{1 + i(\Omega_x \lambda_x + \Omega_y \lambda_y)} \\ &= \frac{1}{2} \int\limits_{-1}^{1} \frac{d\mu}{1 + (\lambda_r \mu)^2} \qquad \left(\lambda_r = \sqrt{\lambda_x^2 + \lambda_y^2} \right) \ , \\ &= \frac{\tan^{-1} \lambda_r}{\lambda_r} \ . \end{aligned}$$

$I_0(\lambda_r)$ monotonically decreases from 1 to 0 as λ_r increases from 0 to ∞. Thus, since $I_0(\lambda_r) > 0$, Eq. (4.3) gives

$$\left[c - \frac{4}{3(\Sigma_t \Delta_z)^2} \right] I_0(\lambda_r) \leq \tilde{\phi}(\boldsymbol{\lambda}) \leq c I_0(\lambda_r) \ .$$

This implies

$$\tilde{\phi}_{max} = c \ , \tag{4.4a}$$

which is attained for "flat" radial and axial modes ($\lambda_r \approx 0$ and $\lambda_z \approx 0$). Also,

$$\tilde{\phi}_{min} = \begin{cases} 0 & , \quad \Sigma_t \Delta_z \geq \frac{2}{\sqrt{3c}} \ , \ \ (\text{ "large" } \Delta_z) \ , \\ c - \frac{4}{3(\Sigma_t \Delta_z)^2} & , \quad \Sigma_t \Delta_z < \frac{2}{\sqrt{3c}} \ , \ \ (\text{ "small" } \Delta_z) \ , \end{cases} \tag{4.4b}$$

which is attained (i) for "large" Δ_z by $\lambda_r \approx \infty$ (radially oscillatory modes), and (ii) for "small" Δ_z by $\lambda_r \approx 0$ (radially flat modes) and $\lambda_z \approx \pi/\Sigma_t \Delta_z$ (axially oscillatory modes).

By Eq. (4.2c), we have for $0 \leq \theta \leq 1$

$$\theta \tilde{\phi}_{min} + 1 - \theta \leq \omega \leq \theta \tilde{\phi}_{max} + 1 - \theta \ . \tag{4.5}$$

For $\theta = 1$ (the "Source Iteration" method originally in DeCART), Eqs. (4.4) and (4.5) give

$$\tilde{\phi}_{min} \leq \omega \leq \tilde{\phi}_{max} \ ,$$

and therefore

$$\rho = |\omega|_{max} = \begin{cases} c & , \quad \sqrt{\frac{2}{3c}} < \Sigma_t \Delta_z \ , \\ \frac{4}{3(\Sigma_t \Delta_z)^2} - c & , \quad \Sigma_t \Delta_z \leq \sqrt{\frac{2}{3c}} \ . \end{cases} \tag{4.6}$$

This method is stable for

$$\Sigma_t \Delta_z > \frac{2}{\sqrt{3(1+c)}} \ ,$$

but for small Δ_z it becomes unstable, similar to the original method in DeCART.

Since $\tilde{\phi}_{max} > 0$, it can be shown that the optimum value of θ in Eq. (4.5) is the value for which the left and right sides are equal in magnitude but opposite in sign:

$$\theta_{opt}\tilde{\phi}_{min} + 1 - \theta_{opt} = -\left[\theta_{opt}\tilde{\phi}_{max} + 1 - \theta_{opt}\right] \ . \tag{4.7a}$$

Thus,

$$\theta_{opt} = \frac{2}{2 - (\tilde{\phi}_{max} + \tilde{\phi}_{min})} \ , \tag{4.7b}$$

and then

$$\begin{aligned} \rho = |\omega|_{max} &= \theta_{opt}\tilde{\phi}_{max} + 1 - \theta_{opt} \\ &= \frac{\tilde{\phi}_{max} - \tilde{\phi}_{min}}{2 - (\tilde{\phi}_{max} + \tilde{\phi}_{min})} \ . \end{aligned} \tag{4.7c}$$

Combining Eqs. (4.4) and (4.7), we obtain:

$$\theta_{opt} = \begin{cases} \frac{2}{2-c} & , \quad \frac{2}{\sqrt{3c}} < \Sigma_t \Delta_z \ , \\ \frac{3(\Sigma_t \Delta_z)^2}{2+3(1-c)(\Sigma_t \Delta_z)^2} & , \quad \Sigma_t \Delta_z \leq \frac{2}{\sqrt{3c}} \ , \end{cases} \tag{4.8a}$$

$$\rho = \begin{cases} \frac{c}{2-c} & , \quad \frac{2}{\sqrt{3c}} < \Sigma_t \Delta_z \ , \\ \frac{2}{2+3(1-c)(\Sigma_t \Delta_z)^2} & , \quad \Sigma_t \Delta_z \leq \frac{2}{\sqrt{3c}} \ . \end{cases} \tag{4.8b}$$

Eq. (4.8b) shows that the iterative method defined by Eqs. (3.36) with θ defined by Eq. (4.8a) is stable for all scattering ratios $0 \leq c \leq 1$ and all axial grids $\Delta_z > 0$. An example of this is shown in Figure 4. Like standard Source Iteration applied to the S_N equations, this method become slowly converging as $c \to 1$. It also becomes

slowly converging as $\Delta_z \to 0$. However, like Source Iteration, it does not become unstable.

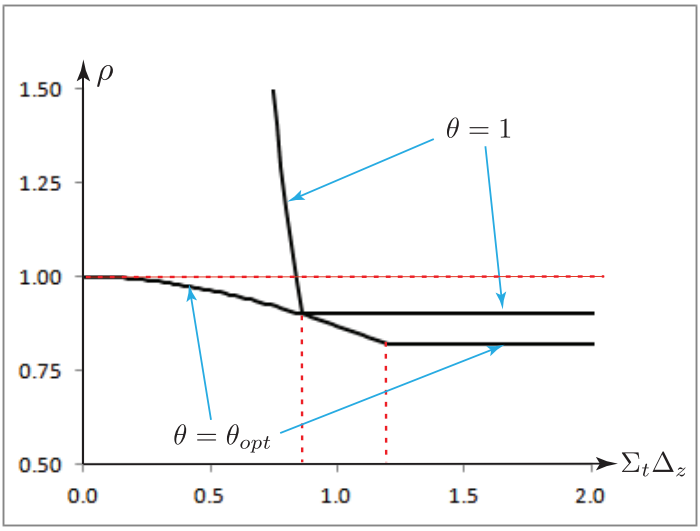

Figure 4: Spectral Radius ρ vs Axial Optical Thickness $\Sigma_t \Delta_z$ for $c = 0.9$

Linear Axial Leakage

Next, we consider the linear approximation, again using $D = 1/3\Sigma_t$:

$$L^{(\ell)}_{z,k}(x,y,\mathbf{\Omega}) \approx \frac{1}{4\pi\Delta_k}\left[-D_{k+1/2}(x,y)\frac{\phi^{(\ell)}_{k+1}(x,y)-\phi^{(\ell)}_{k}(x,y)}{\Delta_{k+1/2}}\right.$$
$$+ D_{k-1/2}(x,y)\frac{\phi^{(\ell)}_{k}(x,y)-\phi^{(\ell)}_{k-1}(x,y)}{\Delta_{k-1/2}}$$
$$+ \mu\frac{\phi^{(\ell)}_{k+1}(x,y)\Delta_{k+1}+\phi^{(\ell)}_{k}(x,y)\Delta_{k}}{\Delta_{k+1}+\Delta_{k}}$$
$$\left.- \mu\frac{\phi^{(\ell)}_{k}(x,y)\Delta_{k}+\phi^{(\ell)}_{k-1}(x,y)\Delta_{k-1}}{\Delta_{k}+\Delta_{k-1}}\right].$$

Again, introducing Eqs. (4.1) into (3.36) for the linear axial leakage, and neglecting anisotropic scattering, we easily obtain

$$\Big(i\big(\Omega_x\lambda_x+\Omega_y\lambda_y\big)+1\Big)\tilde{\psi}(\boldsymbol{\lambda},\boldsymbol{\Omega})=\frac{1}{4\pi}\left(c-\frac{1}{3}\Lambda_z^2-i\Omega_z\frac{\sin\lambda\Sigma_t\Delta_z}{\Sigma_t\Delta_z}\right)\ , \tag{4.9a}$$

$$\tilde{\phi}(\boldsymbol{\lambda})=\int\tilde{\psi}(\boldsymbol{\lambda},\boldsymbol{\Omega})\,d\Omega\ , \tag{4.9b}$$

$$\omega=\theta\tilde{\phi}(\boldsymbol{\lambda})+1-\theta\ . \tag{4.9c}$$

Introducing Eq. (4.9a) into Eq. (4.9b), we get

$$\tilde{\phi}(\boldsymbol{\lambda})=\left(c-\frac{1}{3}\Lambda_z^2\right)I_0(\lambda_r)-i\frac{\sin\lambda\Sigma_t\Delta_z}{\Sigma_t\Delta_z}I_1(\lambda_r)\ , \tag{4.10}$$

where $I_0(\lambda_r)$ was previously defined, and

$$I_1(\lambda_r)=\frac{1}{4\pi}\int\limits_{4\pi}\frac{\Omega_z d\Omega}{1+i(\Omega_x\lambda_x+\Omega_y\lambda_y)}=0\ .$$

This integral is clearly zero, as it is anti-symmetric in the polar cosine and an integral over all angles. Thus, for approximations in which only the scalar flux is iterated upon, any moments that are anti-symmetric in the polar cosine do not affect the convergence rate; thus, the linear approximation converges at the same rate as the isotropic approximation. Also, this means that the quadratic approximation, the diffusion approximation, and the P_1 approximation will all have the same spectral radius. This further confirms the discussion of the considerations of the 2D transport equation.

Quadratic Axial Leakage

Finally, we consider the quadratic approximation, again using $D = 1/3\Sigma_t$:

$$L_{z,k}^{(\ell)}(x,y,\mathbf{\Omega}) \approx \frac{3\mu^2}{4\pi\Delta_k}\left(-D_{k+1/2}(x,y)\frac{\phi_{k+1}^{(\ell)}(x,y)-\phi_k^{(\ell)}(x,y)}{\Delta_{k+1/2}} + D_{k-1/2}(x,y)\frac{\phi_k^{(\ell)}(x,y)-\phi_{k-1}^{(\ell)}(x,y)}{\Delta_{k-1/2}}\right).$$

Again, introducing Eqs. (4.1) into (3.36) for the linear axial leakage, and neglecting anisotropic scattering, we easily obtain

$$\Big(i\big(\Omega_x\lambda_x+\Omega_y\lambda_y\big)+1\Big)\tilde{\psi}(\boldsymbol{\lambda},\mathbf{\Omega}) = \frac{1}{4\pi}\left(c-\Omega_z^2\Lambda_z^2\right)\ , \tag{4.11a}$$

$$\tilde{\phi}(\boldsymbol{\lambda}) = \int \tilde{\psi}(\boldsymbol{\lambda},\mathbf{\Omega})\,d\Omega\ , \tag{4.11b}$$

$$\omega = \theta\tilde{\phi}(\boldsymbol{\lambda})+1-\theta\ . \tag{4.11c}$$

Introducing Eq. (4.11a) into Eq. (4.11b), we get

$$\tilde{\phi}(\boldsymbol{\lambda}) = cI_0(\lambda_r) - \Lambda_z^2 I_2(\lambda_r), \tag{4.12}$$

where $I_0(\lambda_r)$ was previously defined, and

$$\begin{aligned} I_2(\lambda_r) &= \frac{1}{4\pi}\int_{4\pi}\frac{\Omega_z^2 d\Omega}{1+i(\Omega_x\lambda_x+\Omega_y\lambda_y)} \\ &= \frac{1}{4\pi}\int_0^{2\pi}\sin^2\alpha d\alpha\int_{-1}^{1}\frac{1-\mu^2}{1+(\lambda_r\mu)^2}d\mu\ , \\ &= \frac{1}{2}\int_0^1\frac{1-\mu^2}{1+(\lambda_r\mu)^2}d\mu\ , \\ &= \frac{(1+\lambda_r^2)\tan^{-1}\lambda_r-\lambda_r}{2\lambda_r^3}\ . \end{aligned}$$

$I_2(\lambda_r)$ monotonically decreases from 1/3 to 0 as λ_r increases from 0 to ∞. Thus, since $I_0(\lambda_r) > 0$ and $I_2(\lambda_r) > 0$, Eq. (4.12) gives

$$cI_0(\lambda_r) - \frac{4}{(\Sigma_t \Delta_z)^2} I_2(\lambda_r) \leq \tilde{\phi}(\boldsymbol{\lambda}) \leq cI_0(\lambda_r) \; .$$

This implies

$$\tilde{\phi}_{max} = c \; , \tag{4.13a}$$

which is attained for "flat" radial and axial modes ($\lambda_r \approx 0$ and $\lambda_z \approx 0$). Also,

$$\tilde{\phi}_{min} = \begin{cases} 0 & , \quad \Sigma_t \Delta_z \geq \frac{2}{\sqrt{3c}} \; , \quad (\text{ "large" } \Delta_z) \; , \\ c - \frac{4}{3(\Sigma_t \Delta_z)^2} & , \quad \Sigma_t \Delta_z < \frac{2}{\sqrt{3c}} \; , \quad (\text{ "small" } \Delta_z) \; , \end{cases} \tag{4.13b}$$

which is attained (i) for "large" Δ_z by $\lambda_r \approx \infty$ (radially oscillatory modes), and (ii) for "small" Δ_z by $\lambda_r \approx 0$ (radially flat modes) and $\lambda_z \approx \pi / \Sigma_t \Delta_z$ (axially oscillatory modes). At this point, the analysis is identical to that of the isotropic axial leakage approximation. However, this does not imply that convergence is identical between the isotropic and quadratic axial leakage approximations when CMFD acceleration is applied.

4.1.2 Fourier Analysis of CMFD Accelerated 2D/1D

From the section on iterative methods, Eq. (3.36a), (3.36b), (3.42), and (3.43) form a complete, linearized CMFD, 2D/1D iteration scheme. The same standard Fourier ansatz for the source iteration method, Eq. (4.1), can be applied, with the addition of an ansatz for the update term:

$$\delta\phi_k^{(\ell+1/2)}(\mathbf{r}_k) = \omega^\ell \widetilde{\delta\phi}(\boldsymbol{\lambda}) e^{i\Sigma_t(\boldsymbol{\lambda}\cdot\mathbf{r}_k)} \; . \tag{4.14}$$

Because the transport sweep and the scalar flux integral equations are unchanged, so are their corresponding equations in the Fourier analysis. The CMFD and relaxation equations do not depend on the choice of 2D/1D approximation, so they can be analyzed outside of that context. Applying the ansatz to Eqs. (3.42) and (3.43) easily

yields:

$$\left(\frac{\lambda_r^2+\Lambda_z^2}{3}+1-c\right)\widetilde{\delta\phi}(\boldsymbol{\lambda})=\left(c-\frac{\Lambda_z^2}{3}\right)\left(\tilde{\phi}(\boldsymbol{\lambda})-1\right). \tag{4.15}$$

The update equation becomes:

$$\omega(\boldsymbol{\lambda})=\theta\left(\tilde{\phi}(\boldsymbol{\lambda})+\widetilde{\delta\phi}(\boldsymbol{\lambda})\right)+1-\theta\,. \tag{4.16}$$

Combining these two results yields:

$$\omega(\boldsymbol{\lambda})=1-\theta\frac{1-\tilde{\phi}(\boldsymbol{\lambda})}{1-\left(c-\frac{\Lambda_z^2}{3}\right)\left(1+\frac{\lambda_r^2}{3}\right)^{-1}}\,. \tag{4.17}$$

In both isotropic-like and quadratic-like axial leakage approximations, the radially flat modes are the most slowly convergent modes as,

$$\tilde{\phi}(0,0,\lambda_z)=c-\frac{\Lambda_z^2}{3}\,. \tag{4.18}$$

Inserting this into the CMFD acceleration growth factor equation, we see that

$$\omega(0,0,\lambda_z)=1-\theta\,.$$

Thus, if $\theta=1$, the flat modes are perfectly accelerated and converge immediately. The extremum for ω occurs at some $|\lambda_r|>0$. To proceed from this point, the choice of transverse leakage approximation matters.

Isotropic-like Leakage Approximations

From the source iteration section, the equation for $\tilde{\phi}(\boldsymbol{\lambda})$ was found in Eq. (4.3); inserting this into Eq. (4.17) — the CMFD equation for the growth factor — yields:

$$\omega(\boldsymbol{\lambda})=1-\theta\frac{1-\left(c-\frac{\Lambda_z^3}{3}\right)I_0(\lambda_r)}{1-\left(c-\frac{\Lambda_z^2}{3}\right)\left(1+\frac{\lambda_r^2}{3}\right)^{-1}}\,. \tag{4.19}$$

In this form, it is clear that the CMFD acceleration operator well-approximates the transport operator for slowly oscillating radial modes, leading to efficient acceleration of the most slowly converging modes of the source iteration method,

$$I_0(\lambda_r) = \frac{\tan^{-1}\lambda_r}{\lambda_r} \approx 1 - \frac{\lambda^2}{3} + \frac{\lambda^4}{5} + \cdots \approx \left(1 + \frac{\lambda_r^2}{3}\right)^{-1} .$$

Aside from the trivial minimum found in Eq.(4.18), the extremum of the growth factor cannot be determined explicitly given the form of $I_0(\lambda_r)$. However, this function can be parametrized with $\zeta = c - \Lambda_z^2/3$. Evaluating this function numerically, the extremum value can be seen in Figure 5. It is seen that the extrema of the growth factor decrease monotonically with the parameter ζ, with the maximum value occurring for $\zeta = c = 1$, $\omega \approx 0.2247$ (this is the standard result from traditional CMFD). Even though the extremum cannot be calculated explicitly, the numerical results indicate that an empirical estimation should perform well.

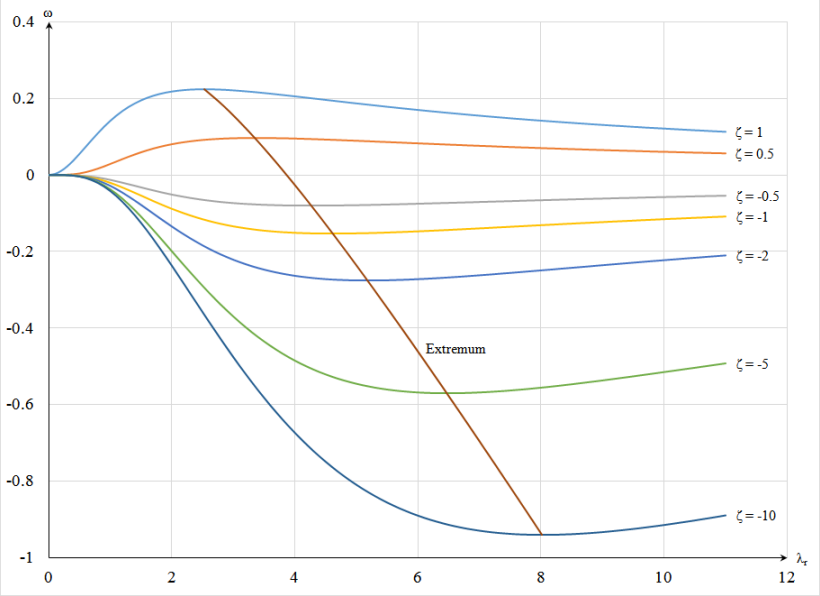

Figure 5: Growth Factor ω for Various Radial Frequencies λ_r for a Sample of Parametrized Values ζ

To make a good empirical approximation, we look at a wide range of values for $-100 \leq \zeta \leq 1$. Figure 6 shows the extremum values of ω, calculated numerically, for

these values of ζ. These data show that the trend seen in Figure 5 continues — a monotonic decrease in ω_{ext} with ζ. It is possible to determine an empirical relation for ω directly, but it is better to determine it for the maximizing/minimizing value of λ_r. This is the case because the equation for ω is available explicitly, and because this is an optimization problem, $\frac{\partial \omega}{\partial \lambda_r} \approx 0$ near the extremum. Thus, small errors in λ_{ext} will result in negligible errors in ω_{ext}. Figure 7 shows the extremum inducing value of λ_r for the large set of ζ sampled. We determine the empirical relation using a least-squares method, recognizing that the data have a form like a shifted root equation. In the range considered, this empirical relation gives values for ω_{ext} less than 5×10^{-5}, and for negative ζ, these errors become less than 10^{-6}.

$$\begin{gathered} \lambda_{ext} \approx S + M(F - \zeta)^P \ , \\ S = 1.93801895412889 \ , \quad M = 1.88037759461481 \ , \\ F = 1.07821249297909 \ , \quad P = 0.487975837139675 \ . \end{gathered} \tag{4.20}$$

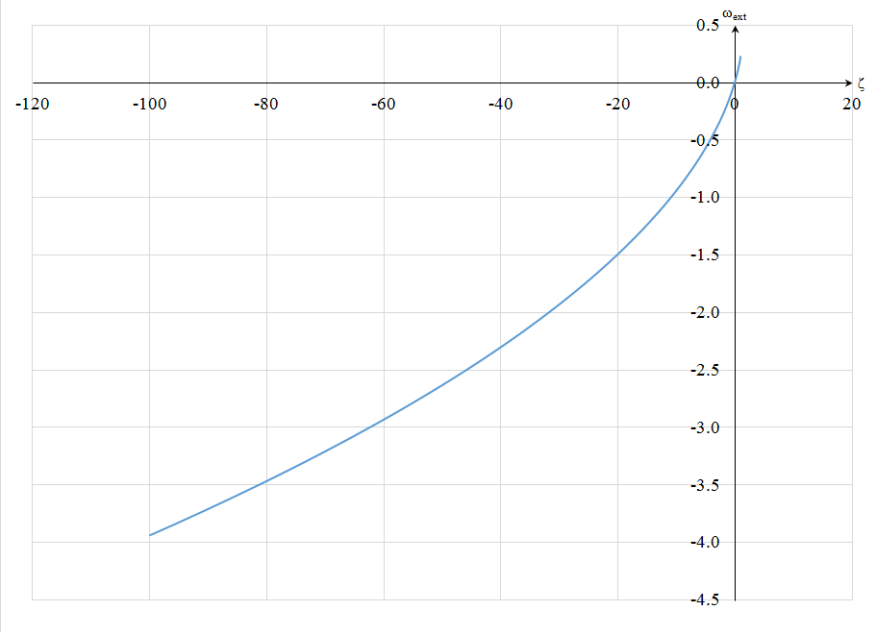

Figure 6: Extremum Growth Factor ω_{ext} vs Parametrized Value ζ

With implicit values of ω_{ext} in hand, we can make some statements about the

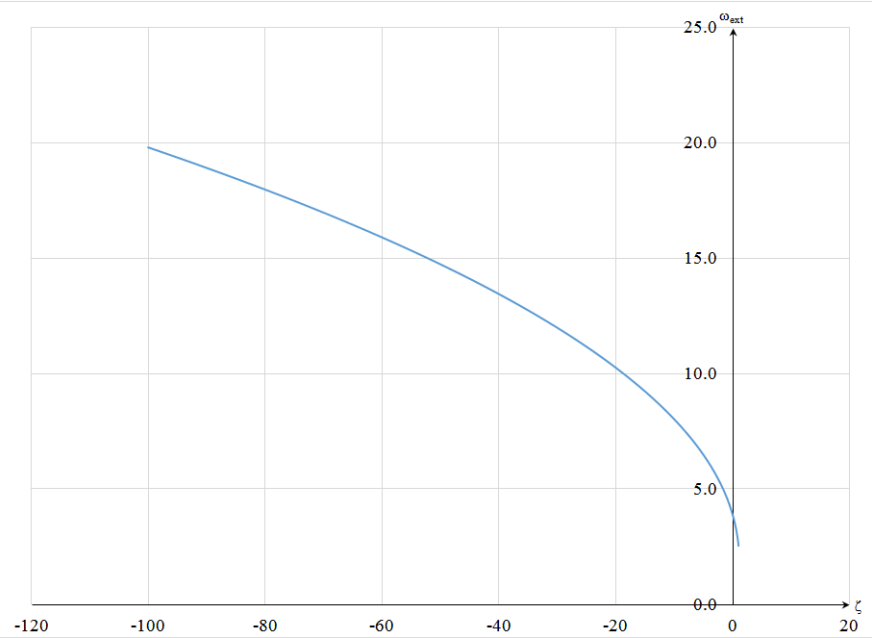

Figure 7: Radial Frequency λ_{ext} which yields Extremum Growth Factor ω_{ext} vs Parametrized Value ζ

method. Traditional CMFD occurs when $\theta = 1$, and this method is conditionally stable if $\zeta \gtrapprox -10.947$ or,

$$\Sigma_t \Delta_z \gtrapprox \frac{2}{\sqrt{3(c + 10.947)}} \ . \tag{4.21}$$

The region of conditional stability for the CMFD accelerated, isotropic 2D/1D approximation is much larger than that of source iteration. This improvement comes from the improved communication between the planes — at each iterate, the planes receive information from the whole system rather than just neighboring planes.

As with source iteration, the relaxation factor can be chosen to yield optimal convergence. We have upper and lower bounds for the growth factor with relaxation based on the Fourier analysis without relaxation:

$$\theta\omega_{min,\theta=1} + 1 - \theta \leq \omega \leq \theta\omega_{max,\theta=1} + 1 - \theta \ . \tag{4.22}$$

We can determine the optimal relaxation factor by choosing it such that the magni-

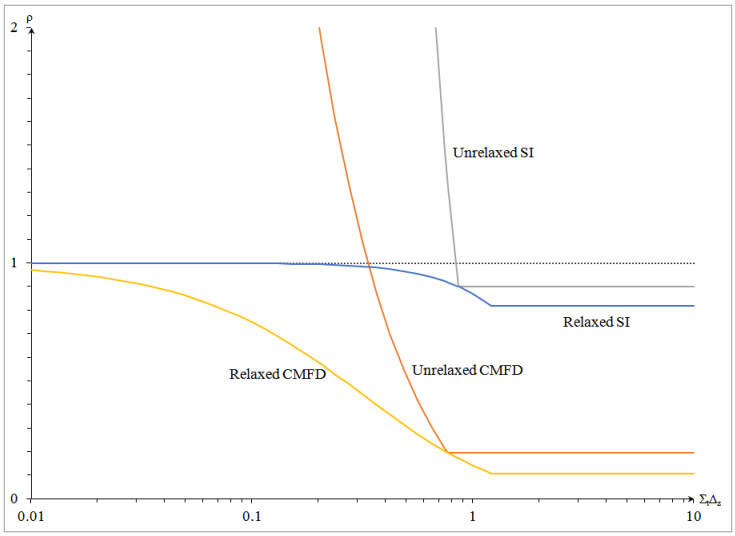

Figure 8: Spectral Radius ρ Comparison of SI and CMFD vs Optical Thickness $\Sigma_t \Delta_z$ with Scattering Ratio $c = 0.9$

tudes of the most positive and negative growth factors are equal:

$$-\left(\theta_{opt}\omega_{min,\theta=1} + 1 - \theta_{opt}\right) = \theta_{opt}\omega_{max,\theta=1} + 1 - \theta_{opt} \ . \tag{4.23}$$

The optimal relaxation factor is then:

$$\theta_{opt} = \frac{2}{2 - \left(\omega_{max,\theta=1} + \omega_{min,\theta=1}\right)} \ . \tag{4.24}$$

The spectral radius that results from using this optimal relaxation factor is then:

$$\rho_{opt} = \frac{\omega_{max,\theta=1} - \omega_{min,\theta=1}}{2 - \left(\omega_{max,\theta=1} + \omega_{min,\theta=1}\right)} \ . \tag{4.25}$$

To summarize the Fourier analysis results thus far, we plot the spectral radius of the relaxed and unrelaxed "source iteration" and CMFD accelerated 2D/1D iteration schemes when using isotropic leakage in Figure 8. As expected, we see that CMFD converges much more rapidly than the "source iteration" counterpart. In fact, the relaxed CMFD iteration scheme is rapidly convergent for all but the thinnest of axial planes; in comparison, the relaxed "source iteration" scheme also guarantees stability

but is slow to converge for even for medium thickness planes. When these methods are not relaxed, we see that the CMFD iteration scheme has a lower plane thickness bound for stability than "source iteration", but the bounding plane is not thin enough to avoid potential stability issues if applied to realistic reactor problems.

Quadratic-like Leakage Approximations

From the source iteration section, the equation for $\tilde{\phi}(\boldsymbol{\lambda})$ was found in Eq. (4.12); inserting this into Eq. (4.17) — the CMFD equation for the growth factor — yields:

$$\omega(\boldsymbol{\lambda}) = 1 - \theta \frac{1 - (cI_0(\lambda_r) - \Lambda_z^3 I_2(\lambda_r))}{1 - \left(c - \frac{\Lambda_z^2}{3}\right)\left(1 + \frac{\lambda_r^2}{3}\right)^{-1}} \,. \tag{4.26}$$

Unlike the isotropic-like leakages, this growth factor cannot be directly parameterized on a single value. The integral $I_2(\lambda_r)$ is clearly bounded between 1/3 and 0; furthermore, it can be bounded more closely in relation to the integral $I_0(\lambda_r)$. Bounding from above,

$$\begin{aligned} I_2(\lambda_r) &= \frac{(1+\lambda_r^2)\tan^{-1}\lambda_r - \lambda_r}{2\lambda_r^3} \,, \\ &= \frac{\tan^{-1}\lambda_r}{2\lambda_r} - \frac{\lambda_r - \tan^{-1}\lambda_r}{2\lambda_r^3} \,, \\ &\leq \frac{I_0(\lambda_r)}{2} \,. \end{aligned}$$

Bounding from below,

$$\begin{aligned} I_2(\lambda_r) &= \frac{\tan^{-1}\lambda_r}{3\lambda_r} + \frac{(1+\frac{\lambda_r^2}{3})\tan^{-1}\lambda_r - \lambda_r}{2\lambda_r^3} \,, \\ I_2(\lambda_r) &\geq \frac{I_0(\lambda_r)}{3} \,. \end{aligned}$$

These bounds are displayed in Figure 9.

From this, we expect the isotropic-like leakage empirical formula, Eq. (4.20), to give a good approximate value for λ_{ext}. To get the true extremum value, we could

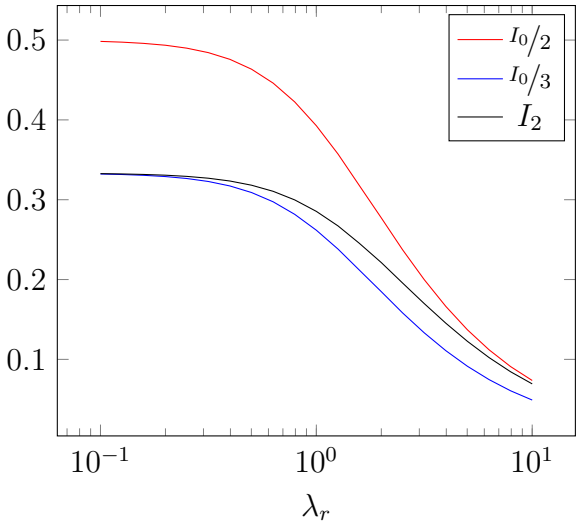

Figure 9: Bounded Limits of $I_2(\lambda_r)$, Relative to $I_0(\lambda_r)$

apply a finite difference Newton's method iteration:

$$\lambda_{n+1} = \lambda_n - \frac{d\lambda}{2} \frac{\omega(\lambda_n + d\lambda) - \omega(\lambda_n - d\lambda)}{\omega(\lambda_n + d\lambda) - 2\omega(\lambda_n) + \omega(\lambda_n - d\lambda)} \,, \tag{4.27a}$$

$$\lambda_{ext} \approx \lim_{n \to \infty} \lambda_n \,. \tag{4.27b}$$

In practice, we do not employ the Newton's method iteration. The Fourier analysis is based on an idealized problem and the initial estimate provided by Eq. (4.20) is sufficient for the purposes of stabilizing and nearly optimizing the method when using the quadratic leakage approximation.

4.1.3 Fourier Analysis of 2D/1D with Nodal Axial Diffusion and CMFD

In this iterative method, both the plane scalar flux and inter-plane current are retained each iteration; we must therefore use a different Fourier ansatz than previous to proceed:

$$\phi_k^{(\ell)}(\mathbf{r}_k) = \omega^\ell \tilde{\phi} e^{i\Sigma_t(\boldsymbol{\lambda}\cdot\mathbf{r}_k)} \,, \tag{4.28a}$$

$$J^{(\ell)}_{z,k+1/2}(\mathbf{r}_k) = \omega^\ell \tilde{J}_z e^{i\Sigma_t(\boldsymbol{\lambda}\cdot\mathbf{r}_{k+1/2})} \ , \tag{4.28b}$$

$$\psi^{(\ell+1/2)}_k(\mathbf{r}_k) = \omega^\ell \tilde{\psi} e^{i\Sigma_t(\boldsymbol{\lambda}\cdot\mathbf{r}_k)} \ , \tag{4.28c}$$

$$\phi^{(\ell+1/2)}_k(\mathbf{r}_k) = \omega^\ell \hat{\phi} e^{i\Sigma_t(\boldsymbol{\lambda}\cdot\mathbf{r}_k)} \ , \tag{4.28d}$$

$$J^{(\ell+1/2)}_{x/y,k}(\mathbf{r}_k) = \omega^\ell \hat{J}_{x/y} e^{i\Sigma_t(\boldsymbol{\lambda}\cdot\mathbf{r}_k)} \ , \tag{4.28e}$$

$$S^{(\ell+1/2)}_{n,k}(\mathbf{r}_k) = \omega^\ell \hat{S}_n e^{i\Sigma_t(\boldsymbol{\lambda}\cdot\mathbf{r}_k)} \ , \tag{4.28f}$$

$$\phi^{(\ell+1/2)}_{n,k}(\mathbf{r}_k) = \omega^\ell \hat{\phi}_n e^{i\Sigma_t(\boldsymbol{\lambda}\cdot\mathbf{r}_k)} \ , \tag{4.28g}$$

$$A^{(\ell+1/2)}_k(\mathbf{r}_k) = \omega^\ell \hat{A} e^{i\Sigma_t(\boldsymbol{\lambda}\cdot\mathbf{r}_k)} \ , \tag{4.28h}$$

$$B^{(\ell+1/2)}_k(\mathbf{r}_k) = \omega^\ell \hat{B} e^{i\Sigma_t(\boldsymbol{\lambda}\cdot\mathbf{r}_k)} \ , \tag{4.28i}$$

$$J^{(\ell+1/2)}_{z,k+1/2}(\mathbf{r}_k) = \omega^\ell \hat{J}_z e^{i\Sigma_t(\boldsymbol{\lambda}\cdot\mathbf{r}_{k+1/2})} \ , \tag{4.28j}$$

$$\delta\phi^{(\ell+1/2)}_k(\mathbf{r}_k) = \omega^\ell \tilde{\delta\phi} e^{i\Sigma_t(\boldsymbol{\lambda}\cdot\mathbf{r}_k)} \ . \tag{4.28k}$$

Applying this ansatz to the transport equation and the equations for the resulting scalar flux and radial currents, we obtain:

$$\big(1 + i(\lambda_x\Omega_x + \lambda_y\Omega_y)\big)\tilde{\psi} = \frac{1}{4\pi}\big(c\tilde{\phi} - i\Lambda_z\tilde{J}\big) \ , \tag{4.29a}$$

$$\hat{\phi} = \big(c\tilde{\phi} - i\Lambda_z\tilde{J}\big) I_0(\lambda_r) \ , \tag{4.29b}$$

$$\hat{J}_{x,y} = \big(c\tilde{\phi} - i\Lambda_z\tilde{J}\big)\frac{1}{4\pi}\int\limits_{4\pi} \frac{\Omega_{x/y}d\Omega}{1 + i(\lambda_x\Omega_x + \lambda_y\Omega_y)} \ . \tag{4.29c}$$

Moving on to the flat nodal source term, we get:

$$\begin{aligned}\tilde{S}_0 &= -i\Sigma_t\big(\lambda_x\hat{J}_x + \lambda_y\hat{J}_y\big) \\ &= -\Sigma_t\big(c\tilde{\phi} - i\Lambda_z\tilde{J}\big)\frac{1}{4\pi}\int\limits_{4\pi}\frac{i(\lambda_x\Omega_x + \lambda_y\Omega_y)d\Omega}{1 + i(\lambda_x\Omega_x + \lambda_y\Omega_y)} \ ,\end{aligned}$$

or

$$\tilde{S}_0 = -\Sigma_t\big(c\tilde{\phi} - i\Lambda_z\tilde{J}\big)\big(1 - I_0(\lambda_r)\big) \ . \tag{4.30a}$$

The remaining non-zero nodal source terms become:

$$\tilde{S}_1 = -i\Sigma_t\big(c\tilde{\phi} - i\Lambda_z\tilde{J}\big)\big(1 - I_0(\lambda_r)\big)\sin(\lambda_z\Sigma_t\Delta_z/2)\cos(\lambda_z\Sigma_t\Delta_z/2)\ , \tag{4.30b}$$

$$\tilde{S}_2 = \frac{\Sigma_t}{3}\big(c\tilde{\phi} - i\Lambda_z\tilde{J}\big)\big(1 - I_0(\lambda_r)\big)\sin^2(\lambda_z\Sigma_t\Delta_z/2)\ . \tag{4.30c}$$

The nodal flux terms become:

$$\hat{\phi}_0 = \frac{c\tilde{\phi} - i\Lambda_z\tilde{J}}{1-c}\big(1 - I_0(\lambda_r)\big)\left(\frac{\Lambda_z^2}{3(1-c)} - 1\right)\ , \tag{4.31a}$$

$$\hat{\phi}_1 = -i\frac{c\tilde{\phi} - i\Lambda_z\tilde{J}}{1-c}\big(1 - I_0(\lambda_r)\big)\sin(\lambda_z\Sigma_t\Delta_z/2)\cos(\lambda_z\Sigma_t\Delta_z/2)\ , \tag{4.31b}$$

$$\hat{\phi}_2 = \frac{1}{3}\frac{c\tilde{\phi} - i\Lambda_z\tilde{J}}{1-c}\big(1 - I_0(\lambda_r)\big)\sin^2(\lambda_z\Sigma_t\Delta_z/2)\ . \tag{4.31c}$$

The hyperbolic cosine nodal term becomes:

$$\begin{aligned}\hat{B} &= \frac{\kappa}{\sinh(\kappa)}\big(\hat{\phi} - \hat{\phi}_0\big) \\ &= \frac{\kappa}{\sinh(\kappa)}\big(c\tilde{\phi} - i\Lambda_z\tilde{J}\big)\left[I_0(\lambda_r) + \frac{1 - {}^{\Lambda_z^2}\!/_{3(1-c)}}{1-c}\big(1 - I_0(\lambda_r)\big)\right]\ ,\end{aligned}$$

or

$$\hat{B} = \frac{\kappa}{\sinh(\kappa)}\frac{c\tilde{\phi} - i\Lambda_z\tilde{J}}{1-c}\left[1 - \frac{\Lambda_z^2}{3(1-c)} - \left(c - \frac{\Lambda_z^2}{3(1-c)}\right)I_0(\lambda_r)\right]\ . \tag{4.32}$$

The Fourier ansatz cannot be directly applied to the matrix equation for the hyperbolic sine nodal term as the $A_k^{(\ell+1/2)}(x,y)$ obtained when solving the two nodes for $J_{k-1/2}^{(\ell+1/2)}(x,y)$ is not the same as that obtained whens solving the two nodes for $J_{k+1/2}^{(\ell+1/2)}(x,y)$. Applying the Fourier ansatz to the solution of the matrix equation yields:

$$\begin{aligned}\hat{A}e^{-i\lambda_z\Sigma_t\Delta_z/2} = &-\frac{\cos(\lambda_z\Sigma_t\Delta_z/2)\left(\kappa\sinh^2(\kappa)\hat{B} + \kappa\cosh(\kappa)\hat{\phi}_1 + 3\sinh(\kappa)\hat{\phi}_2\right)}{\kappa\sinh(\kappa)\cosh(\kappa)} \\ &+ \frac{i\sin(\lambda_z\Sigma_t\Delta_z/2)\left(\kappa\cosh^2(\kappa)\hat{B} + \kappa\cosh(\kappa)\big(\hat{\phi}_0 + \hat{\phi}_2\big) + \sinh(\kappa)\hat{\phi}_1\right)}{\kappa\sinh(\kappa)\cosh(\kappa)}\ .\end{aligned} \tag{4.33}$$

The final nodal equation, the edge current becomes:

$$\begin{aligned}
\hat{J}_z &= -\beta\left(\kappa\cosh(\kappa)\hat{A} + \kappa\sinh(\kappa)\hat{B} + \hat{\phi}_1 + 3\hat{\phi}_2\right)e^{-i\lambda_z\Sigma_t\Delta_z/2} \\
&= -\beta\Bigg[-\cos(\lambda_z\Sigma_t\Delta_z/2)\left(\kappa\sinh(\kappa)\hat{B} + \frac{\kappa}{\tanh(\kappa)}\hat{\phi}_1 + 3\hat{\phi}_2\right) \\
&\qquad + i\sin(\lambda_z\Sigma_t\Delta_z/2)\left(\frac{\kappa\cosh^2(\kappa)}{\sinh(\kappa)}\hat{B} + \frac{\kappa}{\tanh(\kappa)}\left(\hat{\phi}_0 + \hat{\phi}_2\right) + \hat{\phi}_1\right) \\
&\qquad + \left(\kappa\sinh(\kappa)\hat{B} + \hat{\phi}_1 + 3\hat{\phi}_2\right)e^{-i\lambda_z\Sigma_t\Delta_z/2}\Bigg] \\
&= -\beta\Bigg[\cos(\lambda_z\Sigma_t\Delta_z/2)\left(1 - \frac{\kappa}{\tanh(\kappa)}\right)\hat{\phi}_1 \\
&\qquad + i\sin(\lambda_z\Sigma_t\Delta_z/2)\left(\frac{\kappa}{\sinh(\kappa)}\hat{B} + \frac{\kappa}{\tanh(\kappa)}\left(\hat{\phi}_0 + \hat{\phi}_2\right) - 3\hat{\phi}_2\right)\Bigg],
\end{aligned}$$

or

$$\begin{aligned}
i\Lambda_z\hat{J}_z = \frac{\Lambda_z^2}{3}\frac{c\tilde{\phi} - i\Lambda_z\tilde{J}}{1-c}\Bigg[&\frac{\kappa^2}{\sinh^2(\kappa)}\left(1 - \frac{\Lambda_z^2}{3(1-c)} - \left(c - \frac{\Lambda_z^2}{3(1-c)}\right)I_0(\lambda_r)\right) \\
&- \left(1 - I_0(\lambda_r)\right)\left(1 - \frac{\kappa}{\tanh(\kappa)}\frac{\Lambda_z^2}{3(1-c)}\left(1 - \frac{2}{3}\kappa^2\right)\right)\Bigg].
\end{aligned} \tag{4.34}$$

With the transform of the nodal equations complete, only the CMFD equations remain. Applying the Fourier ansatz to these equations yields:

$$\left(\frac{\lambda_r^2 + \Lambda_z^2}{3} + 1 - c\right) = \left(c\hat{\phi} - i\Lambda_z\hat{J}_z\right) - \left(c\tilde{\phi} - i\Lambda_z\tilde{J}_z\right), \tag{4.35}$$

$$\omega\tilde{\phi} = \hat{\phi} + \tilde{\delta\phi}, \tag{4.36}$$

$$\omega\tilde{J}_z = \hat{J}_z - \frac{i\Lambda_z}{3}\tilde{\delta\phi}. \tag{4.37}$$

The update equations can be combined to avoid a matrix equation for the growth factor:

$$\omega\left(c\tilde{\phi} - i\Lambda_z\tilde{J}_z\right) = \left(c\hat{\phi} - i\Lambda_z\hat{J}_z\right) + \left(c - \frac{\Lambda_z^2}{3}\right)\tilde{\delta\phi} \; . \tag{4.38}$$

The growth factor of the method if CMFD were not used would be:

$$\omega_{NODAL,SI} = \frac{c\hat{\phi} - i\Lambda_z\hat{J}_z}{c\tilde{\phi} - i\Lambda_z\tilde{J}_z} \; . \tag{4.39}$$

This notation is useful for the simplifying the CMFD equation:

$$\begin{aligned} \omega &= \omega_{NODAL,SI} - \frac{\Lambda_z^2/3 - c}{\Lambda_z^2/3 + \lambda_r^2/3 + 1 - c}\left(\omega_{NODAL,SI} - 1\right) \; , \\ \omega &= 1 - \frac{1 - \omega_{NODAL,SI}}{1 - \left(c - \Lambda_z^2/3\right)\left(1 + \lambda_r^2/3\right)^{-1}} \; . \end{aligned} \tag{4.40}$$

From this and Eq. (4.19), we see that whether finite difference or nodal methods are used, the accelerated and unaccelerated growth factors are related by the form:

$$\omega_{CMFD} = 1 - \frac{1 - \omega_{SI}}{1 - \left(c - \Lambda_z^2/3\right)\left(1 + \lambda_r^2/3\right)^{-1}} \; .$$

Coincidentally, the growth factor–while difficult to evaluate theoretically–is seen computationally to be bounded by the finite difference method. From this, we take for granted that the under-relaxation factors produced from the finite difference method will conservatively stabilize the nodal methods.

We see below in Figure 10, that for a particular case of scattering ratio and plane thickness, the negative growth factor for nodal axial diffusion with unrelaxed CMFD is bounded by the finite difference equivalent. This is our motivation for using the finite difference relaxation when using nodal solvers.

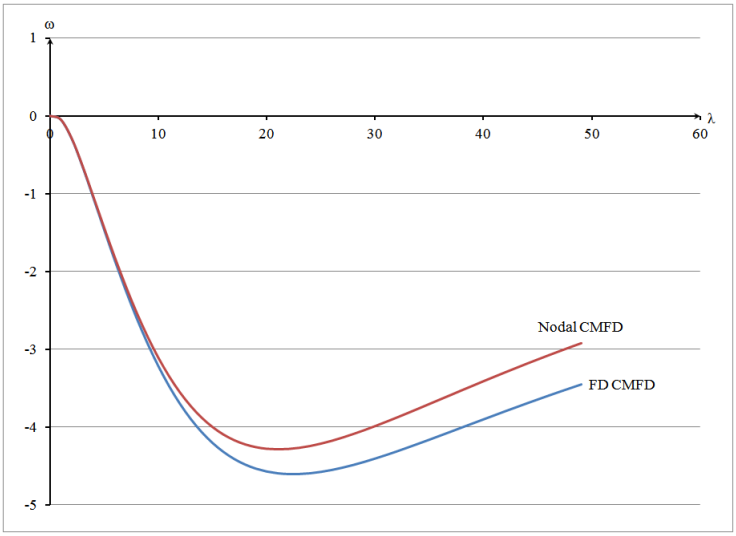

Figure 10: Comparison of the Most Negative Growth Factors between Finite Difference and Nodal Leakage Accelerated by Unrelaxed CMFD for $c = 0.9$ and $\Sigma_t \Delta_z = 0.1$

4.1.4 A Comment on the use of Fourier Analysis

We apply the results of this Fourier analysis to the MPACT code, such that the code itself chooses the optimal relaxation factor based on the plane optical thickness and the scattering ratio (within-group scattering ratio for multi-group problems). To our knowledge, *this is the first time that Fourier analysis has been directly used to improve the performance of a neutron transport code*. Generally, Fourier analysis is used as a demonstrative technique to predict and confirm the convergence properties of an iterative method. We have gone one step further, to use the results to also improve and optimize the convergence of an iterative method.

4.1.5 Numerical Estimates of Spectral Radius

To test the stability and convergence rates of the "source iteration with under-relaxation" scheme, we considered a total of 35 different problems, defined by:

$$
\begin{aligned}
X = Y = Z &= 10 \text{ cm} , \\
\Sigma_t &= 1.0 \text{ cm}^{-1} , \\
\Sigma_s = c &= 0.0,\ 0.25.\ 0.5,\ 0.75, \text{ and } 0.95 \quad (5 \text{ cases}) , \\
Q &= 0.0 \text{ cm}^{-3} \text{ sec}^{-1} , \\
\Delta_x = \Delta_y &= 0.5 \text{ cm} , \\
\Delta_z &= 10.0,\ 5.0,\ 2.0,\ 1.0,\ 0.5,\ 0.2, \text{ and } 0.1 \text{ cm} \quad (7 \text{ cases}) .
\end{aligned}
$$

These problems differ by their 5 values of the scattering ratio c and their 7 values of the axial cell width Δ_z, but they all have the solution $\phi_k(x, y) = 0$. To estimate the spectral radius ρ for each of the 35 cases, we started the iterations with a noisy initial guess and monitored the rate at which the solutions converged to 0. The spectral radius ρ was estimated as

$$\rho = \frac{||\phi^{(n+1)}||}{||\phi^{(n)}||} ,$$

where $||\cdot||$ denotes the L_2 norm over all three spatial dimensions, and n (the iteration count) is sufficiently high that the estimate of ρ is stable.

Source Iteration

When the iterations are run with $\theta = 1$, there is no under-relaxation, and the iteration method becomes very similar to the original iteration method in DeCART. The estimated and predicted (via Fourier analysis) values of ρ are shown below in Figure 11.

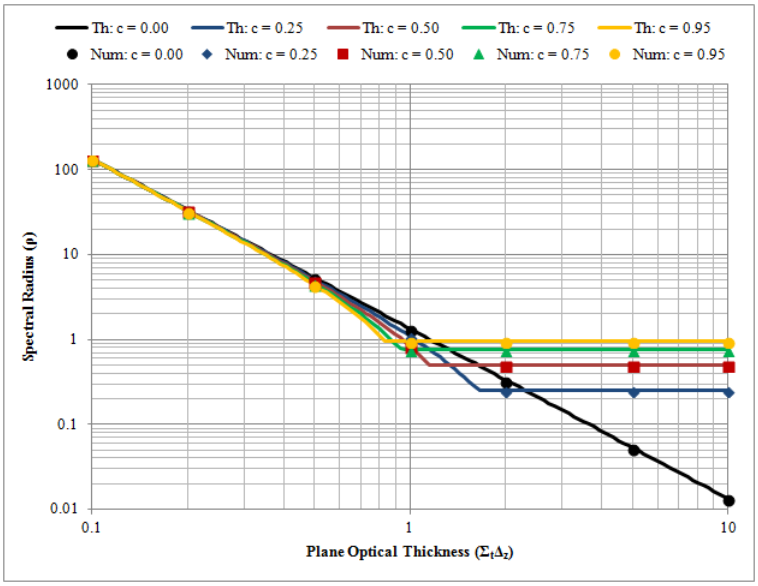

Figure 11: ρ vs $\Sigma_t \Delta_z$ for $\theta = 1$

We see that the estimated values of ρ (symbols) and the theoretical values of ρ (lines) agree quite well, with $\rho = c =$ scattering ratio for $\Sigma_t \Delta_z$ sufficiently large, and $\rho > 1$ (unstable) for roughly $\Sigma_t \Delta_x < 1$.

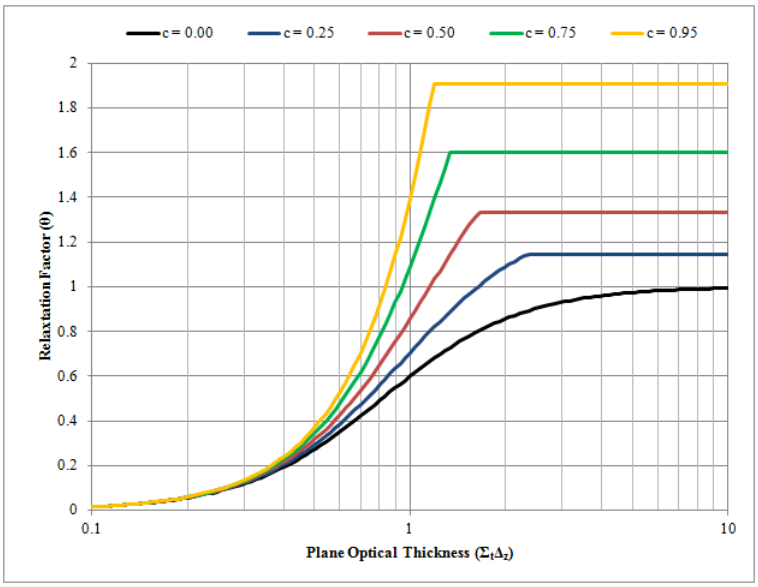

Figure 12: θ_{opt} vs $\Sigma_t \Delta_z$

In Figure 12, the optimal relaxation factor θ_{opt} is plotted as a function of $\Sigma_t \Delta_z$, for 5 different values of the scattering ratio c. As expected, this figure shows that for small $\Sigma_t \Delta_z$ we have $\theta_{opt} < 1$, which corresponds to under-relaxation. Interestingly, for large $\Sigma_t \Delta_z$, we have $\theta_{opt} > 1$, which corresponds to over-relaxation. For large $\Sigma_t \Delta_z$, it is not necessary to over-relax; if one simply uses $\theta = 1$, the theoretical spectral radius $\rho = c$ results. However, the use of $\theta = \theta_{opt}$ does reduce the theoretical spectral radius to $\rho = c/(2 - c)$.

For $\theta = \theta_{opt}$, Figure 13 shows the theoretical (solid lines) and the observed (symbols) estimates of the spectral radius ρ:

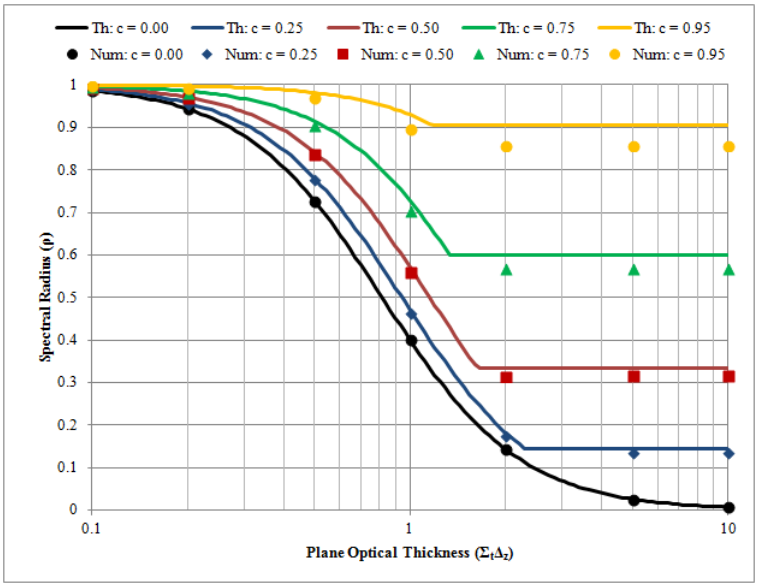

Figure 13: ρ vs $\Sigma_t \Delta_z$ for $\theta = \theta_{opt}$

Again, the agreement between theory and experiment is very good. We have determined that the reason for the faster-than-theoretically-predicted rates of convergence observed experimentally for larger values of $\Sigma_t \Delta_z$ are due to the vacuum boundary conditions. (For large values of Δ_z, the most slowly converging Fourier modes are flat, and these modes are not present unless the system becomes very optically thick.) Overall, the most significant result is that the inclusion of under-relaxation stabilizes the method, and the convergence rates are well- (and conservatively-) predicted by the Fourier analysis.

CMFD Accerlation

In Figure 14 below, we see again that the Fourier analysis accurately predicts the spectral radius of the unrelaxed method. The method is more stable than source iteration, but it becomes unstable for planes with optical thickness $\Sigma_t \Delta_z \lessapprox 0.35$.

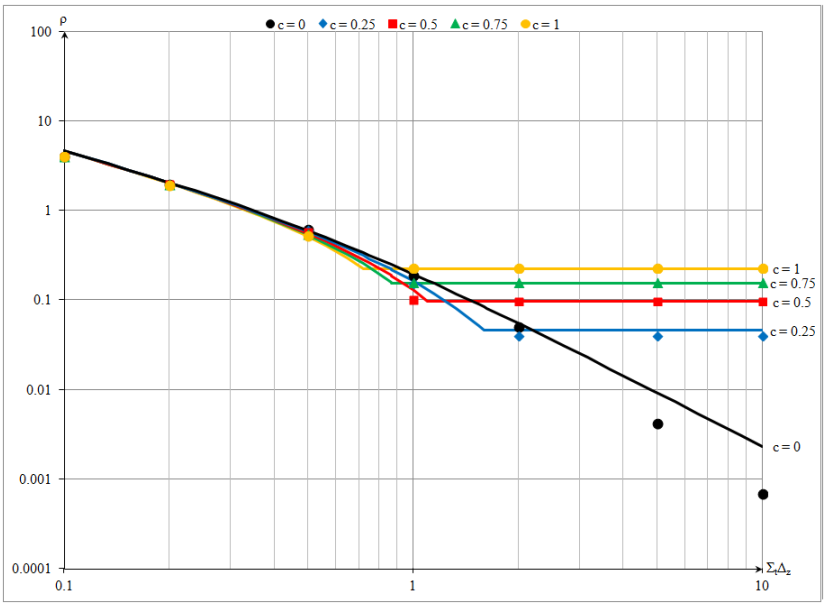

Figure 14: Non-optimized Spectral Radius ρ_{opt} vs Plane Optical Thickness $\Sigma_t \Delta_z$ for Various Scattering Ratios c

In Figure 15 we see that for large plane optical thicknesses, the method can again be over-relaxed for optimal convergence; whereas for small plane optical thicknesses, the method requires under-relaxation for stability. In Figure 16, we observe that the application of the optimal relaxation factor yields a method that is unconditionally stable with more rapid convergence for thick planes than traditional CMFD.

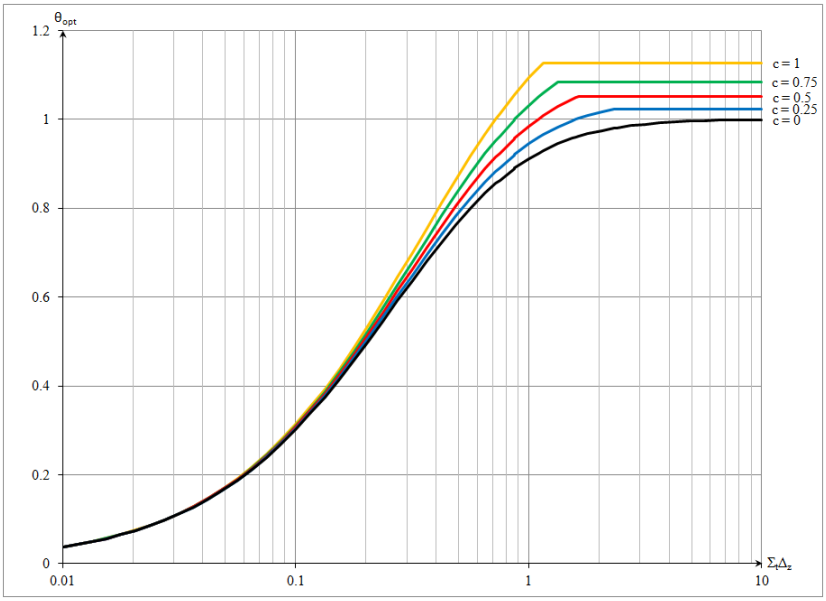

Figure 15: Optimal Relaxation Factor θ_{opt} vs Plane Optical Thickness $\Sigma_t \Delta_z$ for Various Scattering Ratios c

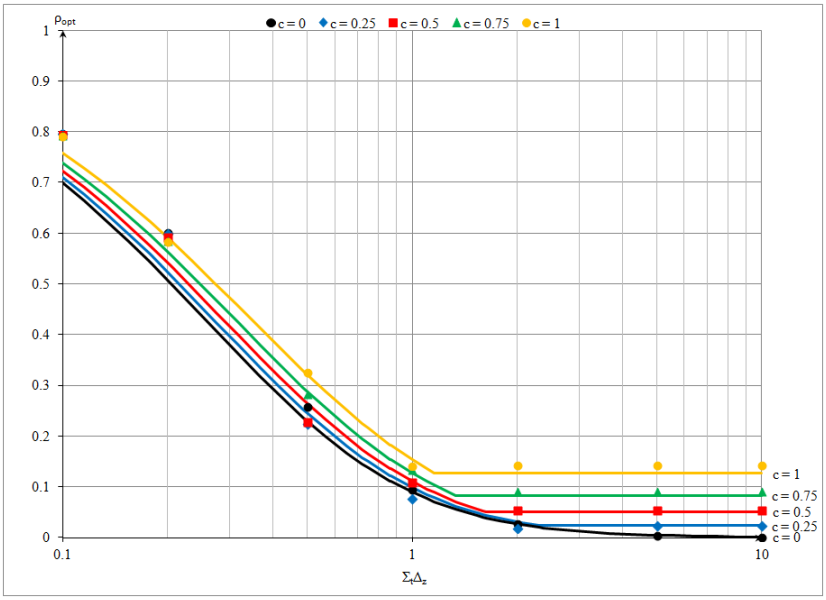

Figure 16: Optimal Spectral Radius ρ_{opt} vs Plane Optical Thickness $\Sigma_t \Delta_z$ for Various Scattering Ratios c

4.2 Accuracy

To demonstrate these properties of the 2D/1D equations, we consider the 3D fixed-source homogeneous-medium transport equation with a flat source:

$$\mathbf{\Omega}\cdot\boldsymbol{\nabla}\psi(\mathbf{r},\mathbf{\Omega})+\Sigma_t\psi(\mathbf{r},\mathbf{\Omega})=\frac{\Sigma_s}{4\pi}\int\limits_{4\pi}\psi(\mathbf{r},\mathbf{\Omega}')d\Omega'+\frac{Q}{4\pi}\ ,\quad \mathbf{r}\in V\ ,\ \mathbf{\Omega}\in 4\pi\ , \tag{4.41}$$

defined on a hexahedral domain V consisting of points $\mathbf{r}=(x,y,z)$, with $(x,y)\in$ the square R consisting of points $0<x,y<L$, and $0\le z\le Z$. The boundary conditions (i) on the "inner" three sides of V touching the point $(0,0,0)$ are reflecting, and (ii) on the "outer" three sides of V are vacuum.

We discretize z by a uniform grid $0=z_{1/2}<\cdots<z_{k-1/2}<z_{k+1/2}<\cdots z_{K+1/2}=Z$, with $z_{k+1/2}-z_{k-1/2}=\Delta_z$. For the k^{th} axial "slice," we define

$$\psi_k(x,y,\mathbf{\Omega})=\frac{1}{\Delta_z}\int\limits_{z_{k-1/2}}^{z_{k+1/2}}\psi(x,y,z',\mathbf{\Omega})dz'\ ,\quad 1\le k\le K\ . \tag{4.42}$$

In Chapter 3, we derived for this (homogeneous medium, uniform axial grid) problem, the following axially-discretized 2D/1D approximation to Eqs. (4.41):

$$\Big(\Omega_x\frac{\partial}{\partial x}+\Omega_y\frac{\partial}{\partial y}+\Sigma_t\Big)\psi_k(x,y,\mathbf{\Omega})=\frac{1}{4\pi}\Bigg[\Sigma_s\phi_k(x,y)+Q \\ +\frac{D}{\Delta_z^2}\Big(\phi_{k+1}(x,y)-2\phi_k(x,y)+\phi_{k-1}(x,y)\Big)\Bigg]\ , \tag{4.43}$$

where

$$\phi_k(x,y)=\int\limits_{4\pi}\psi_k(x,y,\mathbf{\Omega}')\,d\Omega'\quad ,\quad D=\frac{1}{3\Sigma_t}\ . \tag{4.44}$$

The boundary of V has six planar surfaces. The boundary conditions on the four "radial" bounding surfaces of V (whose normal vectors point in the radial directions) are the usual transport reflecting or vacuum boundary conditions. On the two "axial"

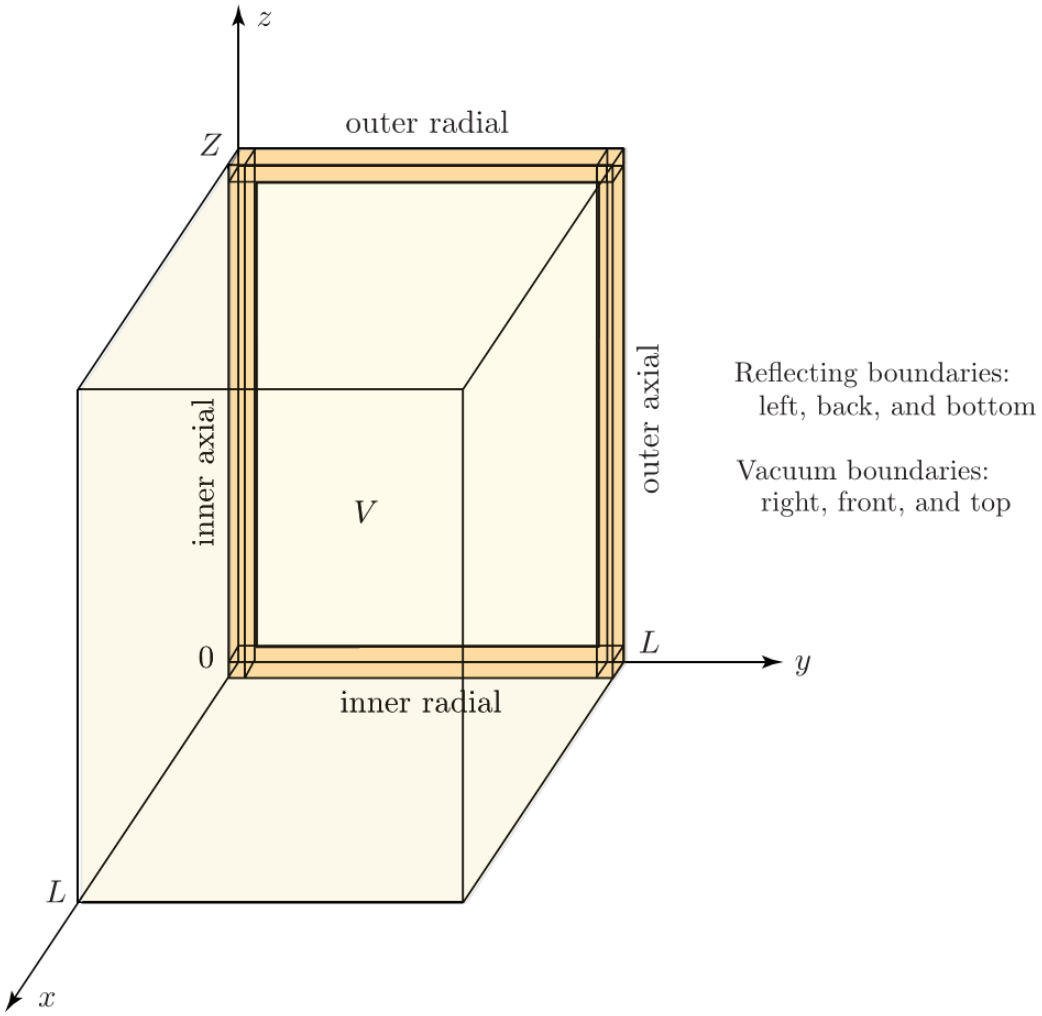

Figure 17: The Hexahedral System V

bounding surfaces of V, whose normal vectors point in the $\pm$ axial directions, the reflecting and vacuum boundary conditions can be formulated as

$$\phi_0(x,y) = \phi_1(x,y)\ , \quad (x,y) \in R \qquad \text{(reflecting)}\ , \tag{4.45a}$$

$$\phi_{K+1}(x,y) = \left(\frac{4D-\Delta_z}{4D+\Delta_z}\right)\phi_K(x,y)\ , \quad (x,y) \in R\text{(vacuum)}\ . \tag{4.45b}$$

These conditions specify ϕ_0 and ϕ_{K+1} and thus make Eq. (4.43) valid for all $1 \leq k \leq K$.

In the MPACT code [12], we have discretized the 2D/1D equation in x, y, and $\mathbf{\Omega}$ using the method of characteristics [17]. In this chapter we discuss the accuracy of the resulting 2D/1D solutions (by showing plots of the scalar flux on the four rows of spatial cells shown in Figure 1) and the performance of the iterative "source iteration with under-relaxation" iteration scheme.

4.2.1 Accuracy in Homogeneous, Purely Scattering Media

To test the accuracy of the 2D/1D solutions, we consider six homogeneous, purely-scattering problems, defined as follows:

$$
\begin{aligned}
Z &= 10 \text{ cm} , \\
X = Y = L &= 10,\ 5,\ \text{and } 2.5 \text{ cm} \qquad (3 \text{ cases}) , \\
\Sigma_t = \Sigma_s &= 1.0 \text{ cm}^{-1} , \\
Q &= 1.0 \text{ cm}^{-3} \text{ sec}^{-1} , \\
\Delta_x = \Delta_y &= 0.05L , \\
\Delta_z &= 0.5 \text{ and } 1.0 \text{ cm} \qquad (2 \text{ cases}) .
\end{aligned}
$$

The problems differ by their values of Δ_z and L, with $\Delta_x = \Delta_y$ scaled proportional to L. For $L = 10$ cm, the system is a cube of width, height, and depth equal to 20 mean free paths. This problem is reasonably "diffusive," so the 3D MOC, 2D/1D and standard diffusion solutions should agree reasonably well. Figure 18 plots the cell-averaged scalar fluxes along the four rows of cells depicted in Figure 17: the "Inner Radial" row, which adjoins the center of the system and extends to the outer boundary in the radial (y) direction, the "Inner Axial" row, which adjoins the center of the system and extends to the outer boundary in the axial (z) direction, and the "Outer Radial" and "Outer Axial" rows, which adjoin the outer boundary of the system.

The 3D MOC and 2D/1D solutions agree closely on the inner radial, inner axial, and outer axial rows of cells. Along these rows, the axial derivative (diffusion) term in the 2D/1D equation does not dominate the radial derivative (transport) term – and

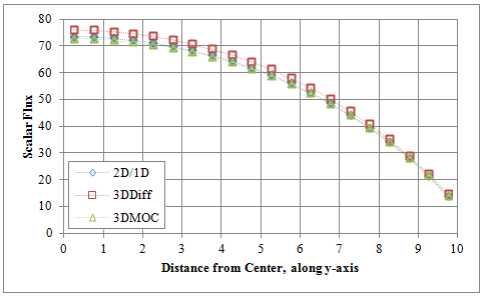

(a) Inner Radial

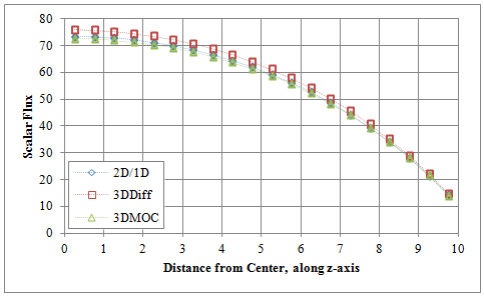

(b) Inner Axial

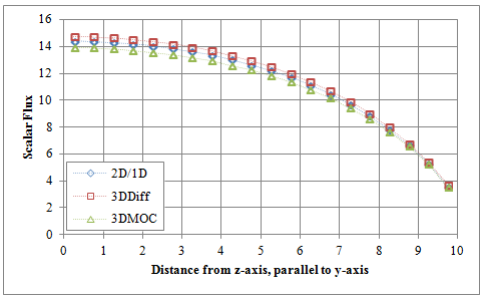

(c) Outer Radial

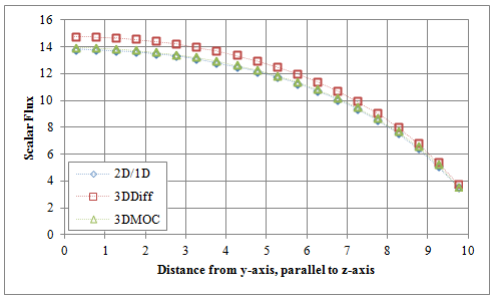

(d) Outer Axial

Figure 18: Scalar Flux Plots for $L = 10$ cm and $\Delta_z = 0.5$ cm

the resulting approximation should be accurate. The accuracy is not as good on the outer radial row of cells, in which an axial transport boundary layer occurs. Here the diffusion axial derivative term of the 2D/1D equation dominates the transport radial derivative terms, and the axial transport boundary layer is treated with diffusion (not transport) accuracy.

In all four subplots of Figure 18, the diffusion solution has the correct qualitative shape, but its amplitude is consistently about 6% high. The reason for the reasonable but not tight accuracy of the diffusion approximation is that the $L = 10$ problem is not sufficiently large (optically thick).

Overall, the 2D/1D solution agrees closely with the 3D MOC solution (i.e. has "transport accuracy") in the interior of V, and on the parts of ∂V where the axial derivative does not dominate the radial derivative. On the parts of ∂V where the axial derivative dominates the radial derivative, the 2D/1D solution has "diffusion accuracy." (Where this happens – on the outer radial row of cells – the 2D/1D error

is about half that of the diffusion solution.)

As L = width = depth of V is reduced, V becomes more "leaky" (and hence more transport-like) in the radial directions x and y. However, V remains optically thick in the z-direction, and the scalar flux should continue to vary smoothly and slowly in z. The 2D/1D solutions for smaller L should continue to have transport accuracy – except possibly on the outer radial row of cells, where at worst it should have diffusion accuracy. Figure 19 depicts similar plots as in Figure 18, but instead for the $L = 5$ problem.

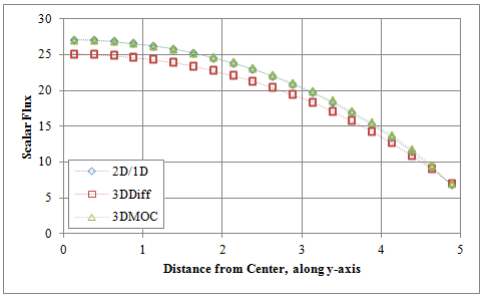

(a) Inner Radial

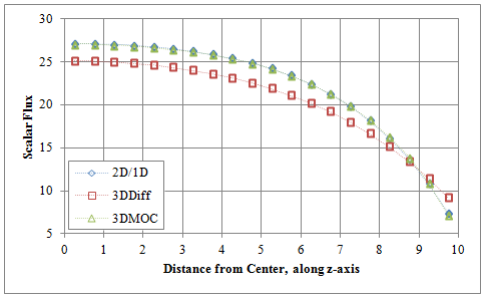

(b) Inner Axial

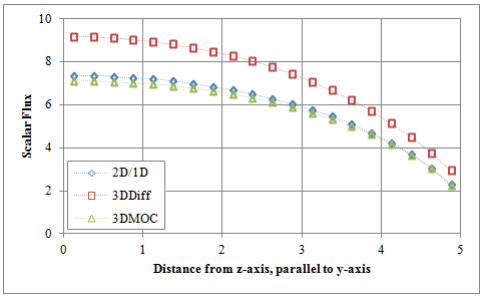

(c) Outer Radial

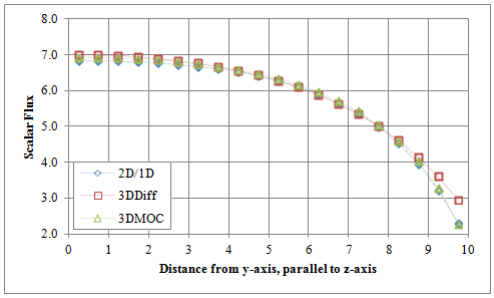

(d) Outer Axial

Figure 19: Scalar Flux Plots for $L = 5$ cm and $\Delta_z = 0.5$ cm

Figure 19 shows that indeed, the 2D/1D solution has transport accuracy away from the outer radial rows of cells, and in this row it is more accurate than before! The likely reason for this is that the axial derivatives in this row are similar to those in the previous problem, but the radial derivatives are larger. Thus, the axial derivatives in this problem do not dominate to the same extent that they did in the previous problem. In this problem, the diffusion solution is about 10% low in the center of the problem, 20% high on the outer radial row, and reasonably accurate on the outer

axial row of cells.

Next, Figure 20 depicts the same types of plots as in Figure 18, for the $L = 2.5$ problem:

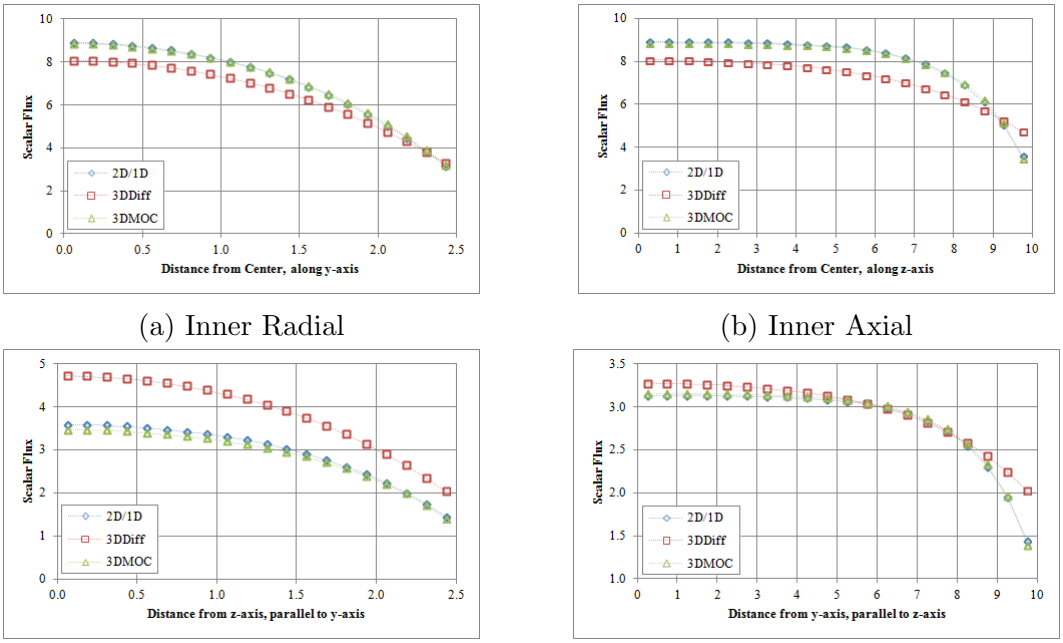

(a) Inner Radial

(b) Inner Axial

(c) Outer Radial

(d) Outer Axial

Figure 20: Scalar Flux Plots for $L = 2.5$ cm and $\Delta_z = 0.5$ cm

These plots continue the same basic trends seen – and discussed – in Figures 18 and 19. Overall, Figures 2-4 show that the 2D/1D solutions treat "radial" boundary layers (along surfaces whose normals point in a radial direction) with transport accuracy, and "axial" boundary layers (along surfaces whose normals point in an axial direction) with at worst diffusion accuracy. (If the axial boundary layers contain significant radial derivative terms, the 2D/1D accuracy increases.)

The next three figures present the same three problems depicted in Figures 18-20, but now calculated with a coarser axial grid size of $\Delta_z = 1.0$ cm. We include these results to give evidence that – provided the solution varies slowy in z – the 2D/1D solution will remain accurate if Δ_z is chosen to be on the order of (or smaller than) a *diffusion length*. The discretization of the transport part of the 2D/1D equation

generally requires the radial variables x and y to be discretized on a grid which is small compared to a *mean free path*. Thus: for the 3D problems in which the 2D/1D approximation is valid, it should be possible to discretize the 2D/1D equations on a coarser axial grid than the 3D transport equation. (This is another advantage of the 2D/1D approximation.) We note that DeCART and MPACT are routinely run in this manner – with an axial grid which is much coarser than the radial grid.

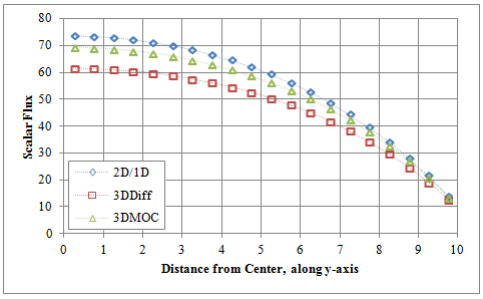

(a) Inner Radial

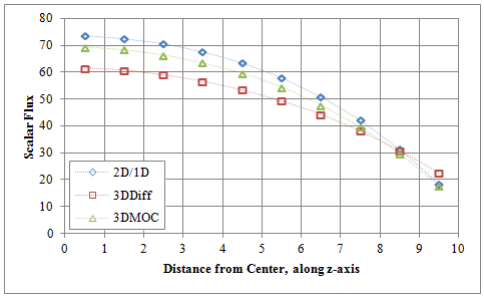

(b) Inner Axial

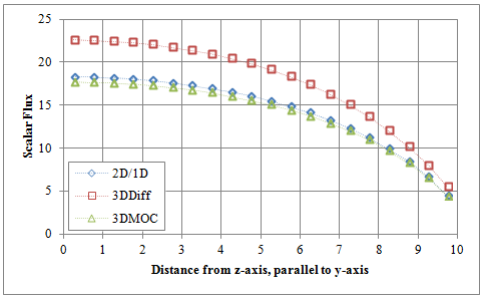

(c) Outer Radial

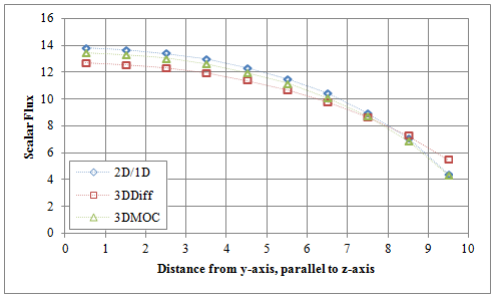

(d) Outer Axial

Figure 21: Scalar Flux Plots for $L = 10$ cm and $\Delta_z = 1.0$ cm

The results in Figures 21-23 are similar to those in Figures 18-20. Overall, the diffusion solution is less accurate than before, due to the transport boundary layer on the outer radial surface, which is now even less resolved by the diffusion solution on the coarser axial grid. In all cases, 2D/1D solution has transport accuracy at points where axial boundary layers do not occur, and at worst diffusion accuracy at points where axial boundary layers do occur. This property of the 2D/1D solutions should continue to hold in heterogeneous reactor cores – which possess a multitude of radial boundary layers, but few axial boundary layers.

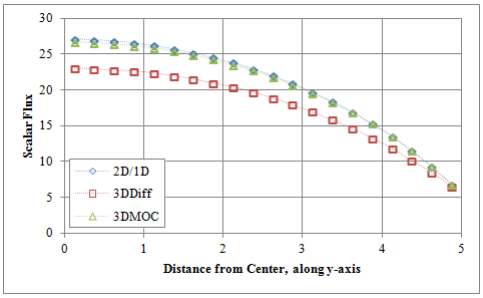

(a) Inner Radial

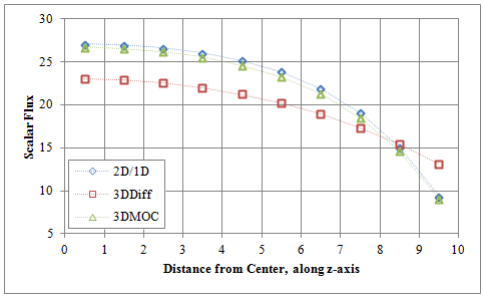

(b) Inner Axial

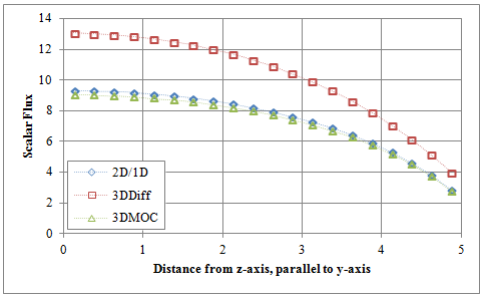

(c) Outer Radial

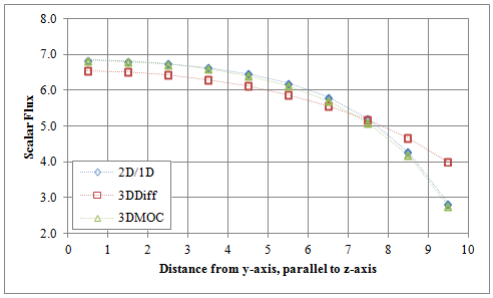

(d) Outer Axial

Figure 22: Scalar Flux Plots for $L = 5$ cm and $\Delta_z = 1.0$ cm

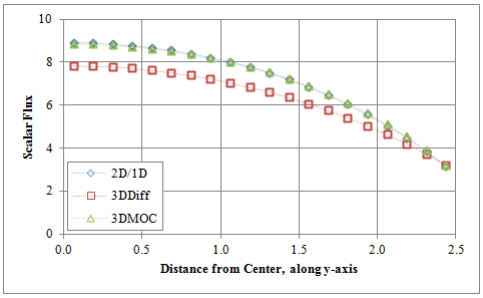

(a) Inner Radial

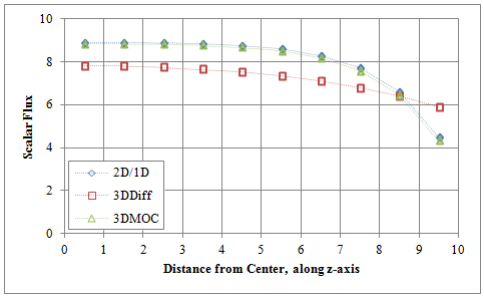

(b) Inner Axial

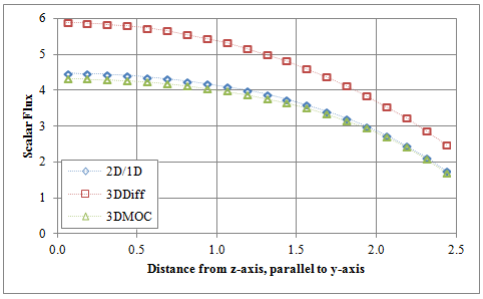

(c) Outer Radial

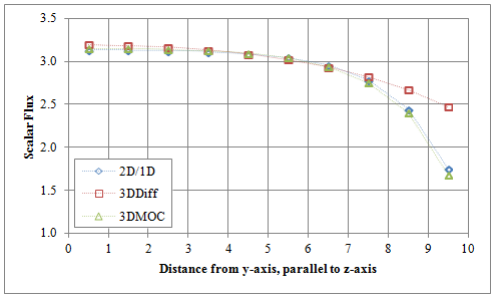

(d) Outer Axial

Figure 23: Scalar Flux Plots for $L = 2.5$ cm and $\Delta_z = 1.0$ cm

Although not measured explicitly, it is worth mentioning that, anecdotally, the 2D/1D algorithm is at least two orders of magnitude faster than 3D MOC. This occurs for a number of reasons:

1. A 3D ray intersects with mesh geometry more frequently than a 2D ray and is thus more computationally expensive individually.
2. Many axial ray segments are needed within each plane for 3D MOC, increasing the overall number of rays to be traced.
3. In 2D MOC, there are no differences in the geometry intersections as the polar cosine changes. This is not the case in 3D MOC, further increasing the complexity of tracing 3D rays.

4.2.2 Motivation for Shape Functions

In order to demonstrate the need for shape functions and evaluate the accuracy of the scalar flux weighting shape function developed in subsection 3.3.1, we consider a 2-group, rectilinear, simplified reactor problem in which we vary no aspect of the discretization other than the use of a shape function. We consider three cases for the same problem: an "exact" shape function (in which the fine mesh and coarse mesh are identical), a "flat" shape function (in which the shape function is unity for each fine mesh region), and a "scalar flux" shape function (in which the shape function is the ratio of the previous iteration fine mesh scalar flux to coarse mesh scalar flux). In all cases, we choose an identical MOC discretization (quadrature and ray spacing) and fine mesh.

Unlike the previous accuracy test, we consider an eigenvalue problem, as the realistic problems we will consider in Chapter 5 will be eigenvalue problems. The 2D/1D

eigenvalue problem that we are solving is:

$$\left(\Omega_x\frac{\partial}{\partial x}+\Omega_y\frac{\partial}{\partial y}+\Sigma_{t,g}\right)\psi_{k,g}(x,y,\mathbf{\Omega})=\frac{1}{4\pi}\left[\sum_{g'=1}^{2}\left(\Sigma_{s,g'\to g}+\frac{\chi_g\nu_{g'}\Sigma_{f,g'}}{k_{eff}}\right)\phi_{k,g'}(x,y)\right.$$
$$\left.+\frac{D}{\Delta_z^2}\left(\phi_{g,i,j,k+1}-2\phi_{g,i,j,k}+\phi_{g,i,j,k-1}\right)V_{g,i,j,k}(x,y)\right]. \tag{4.46}$$

We use the same hexahedral system shown in Figure 17, but we now have Cartesian "pin cells" with both fuel and moderator.

Table 1: Cross Sections of Shape Function Test Problem in cm^{-1}

Cross Section	Fuel	Moderator
$\Sigma_{t,1}$	0.44	1.01
$\Sigma_{a,1}$	0.03	0.01
$\nu\Sigma_{f,1}$	0.04	0
χ_1	1.0	0
$\Sigma_{t,2}$	0.9	3.05
$\Sigma_{a,2}$	0.6	0.05
$\nu\Sigma_{f,2}$	1.1	0
χ_2	0	0
$\Sigma_{s,1\to1}$	0.4	0.4
$\Sigma_{s,2\to1}$	0	0
$\Sigma_{s,1\to2}$	0.01	0.6
$\Sigma_{s,2\to2}$	0.3	3.0

The core dimensions and plane thickness are

$$Z = 15 \text{ cm},$$
$$X = Y = L = 8 \text{ cm},$$
$$\Delta_z = 1.0 \text{ cm}.$$

Also, in this problem, we consider two different mesh arrangements. For the "exact"

shape function results, the fine mesh and coarse mesh are identical:

$$\Delta_x = \Delta_y = 0.125 \text{ cm} ;$$

whereas, for the "flat" and "scalar flux" shape functions, we use two different meshes:

$$\delta_x = \delta_y = 0.125 \text{ cm} ,$$
$$\Delta_x = \Delta_y = 1.0 \text{ cm} .$$

The coarse cell and repeated fine cell structure is shown below in Figure 24.

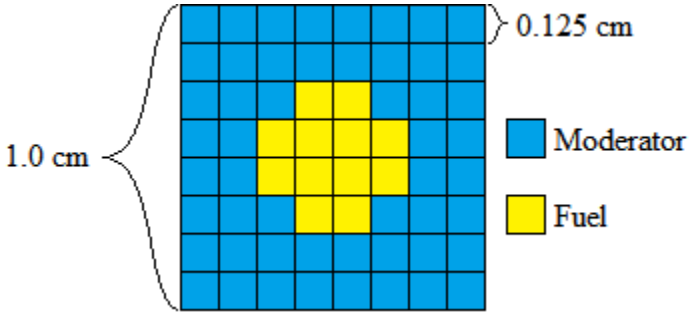

Figure 24: Coarse Cell of the Shape Function Test Problem

To first consider the impact of the shape function, we look at the eigenvalue. We see that, for this problem, the lack of a shape function when comparing the "flat" shape function solution to the "exact" solution results in a significant error. The inclusion of the "scalar flux" shape function ameliorates only a slim portion of this error. Clearly, to obtain more accurate results, much more robust shape functions need to be used.

Table 2: Comparison of k-Eigenvalues with Different Shape Functions

Shape Function	k_{eff}	error [pcm]
Exact	1.1090720	—
Flat	1.1143052	523.32
Flux	1.1142447	517.27

Next, we look at the flux distribution itself. Because this is a "toy" problem, we

care more about the relative error than the actual results.

Table 3: Global Flux Distribution Error with Different Shape Functions

Error	Flat	Flux
RMS Absolute	0.011916	0.011903
RMS Relative	3.50%	3.49%
Max Absolute	0.0415	0.0415
Max Relative	12.92%	12.92%

Again, the "flat" shape function results in noticeable error in the scalar flux distribution when compared to the "exact" solution. Unfortunately, using the "scalar flux" shape function results in negligible reduction of error. Given that we slight improvement when using the simplest possible shape function, we would anticipate more accurate shape functions showing even better accuracy. In fact, another MPACT developer implemented a method similar to the 2D/1D "fusion" method [20] where they observed precisely this fact. In their work, they found it necessary to at least include first order Chebyshev moments in the azimuthal angle ($\cos\alpha$ and $\sin\alpha$) in order to see significant gains in using a shape function.

4.3 Chapter Summary

In this chapter, we have applied Fourier analysis to both predict *and optimize* the iteration schemes that we have considered for the 2D/1D method. With numerical simulation, we have confirmed the predicted spectral radius of the methods and the basic accuracy of the method. In the next chapter, we will apply the 2D/1D method to established, benchmark problems, to determine their accuracy when applied to realistic reactor problems.

Chapter 5

Simulation

In Chapter 4, we considered a few simple problems to test the stability and fundamental accuracy of the methods developed. While these problems are useful in understanding the method, testing against verified benchmark problems lets us verify the performance of the method for realistic problems. We also consider the merits of the two-node, NEM nodal method as opposed to finite differencing of the axial leakage.

5.1 The Takeda Benchmark

The Takeda Benchmarks [21] are a collection of four different benchmark problems of varying complexity. Model one is the simplest benchmark, yet it is challenging for the 2D/1D method due to stark material heterogeneities. As we will only consider model one of the four benchmarks, we will refer to it as the Takeda Benchmark.

The following figures are from the Takeda Benchmark [21] specification and are used to illustrate the geometry. In Figure 25, we see the three regions of the problem: (i) the core, (ii) the reflector, and (iii) the control rod/void region. Each of these regions is homogeneous. The core/rod interface poses the greatest challenge to 2D/1D as the flux is highly anisotropic in this region.

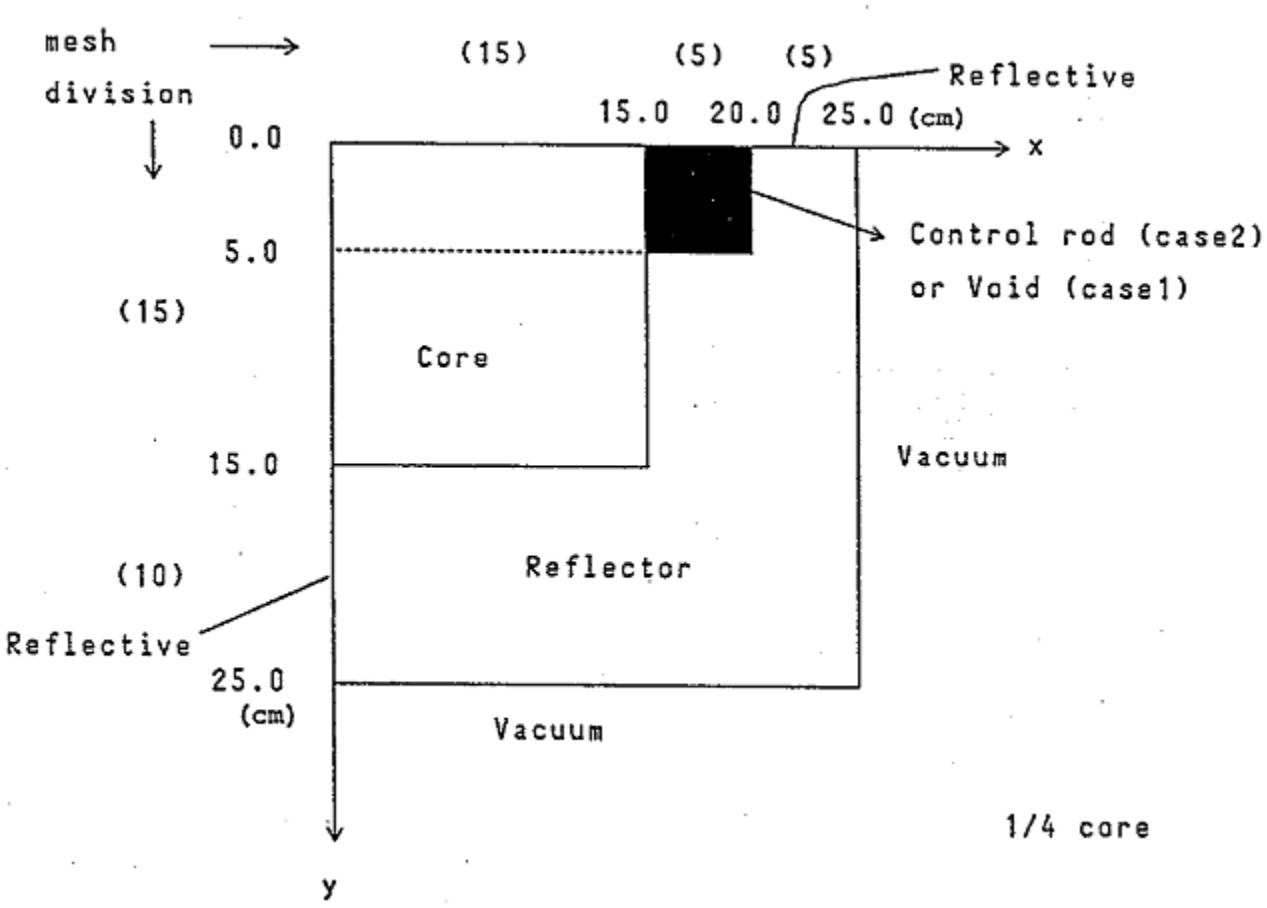

Figure 25: Top Down View of the Takeda Geometry [21]

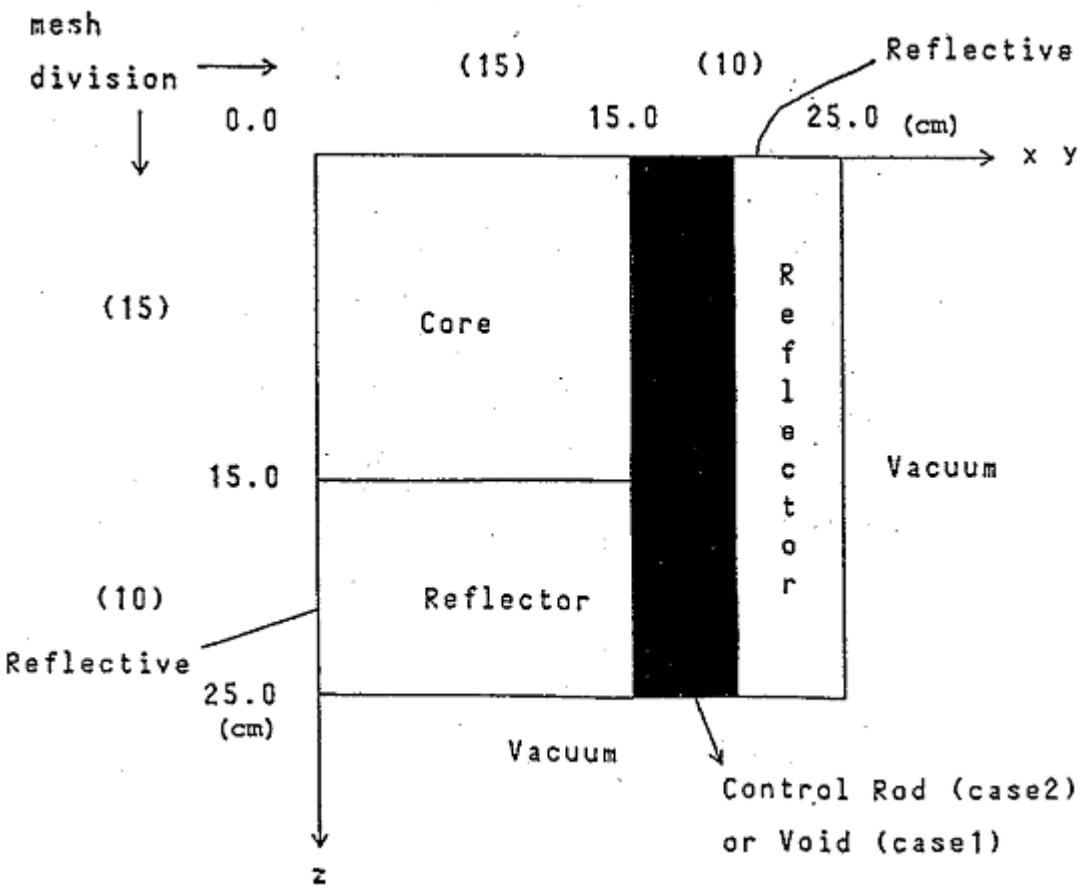

Figure 26: Side View of the Takeda Geometry [21]

5.2 Results of 2D/1D Applied to the Takeda Benchmark

For the solution of this problem with 2D/1D, we use 1 cm × 1 cm radial coarse cells with 0.5 cm×0.5 cm fine cells within. For each plane, the thickness is $\Delta_z = 1$ cm. A Chebyshev-Gauss product quadrature is used with 16 azimuthal angles per quarter and 4 polar angles per half for the 2D MOC, with a ray spacing of 0.05 cm. Our solution matrix consists of 40 method combinations for each of the two problem cases: finite difference vs. nodal, five angular descriptions, two shape function, and axial splitting on/off. We choose to be exhaustive for this benchmark, as it is relatively quick to solve it.

5.2.1 The Unrodded Configuration

The eigenvalues produced by the various methods for the unrodded configuration with finite difference leakage methods are shown below in Table 4. When axial splitting is used, we see that some of these cases could not converge to the desired tolerance; this is a consequence of the source term being split in some iterations and not others, leading to two solutions slightly too different to reconcile.

Table 4: The Finite Difference Eigenvalue Results for the Unrodded Configuration

Shape Function	FLAT	FLAT	FLUX	FLUX
Leakage Splitting?	FALSE	TRUE	FALSE	TRUE
ISO	0.9506628	0.9577284	0.9505832	0.9576517
LIN	0.9506628	0.9742434	0.9505832	0.9741743
QUAD	0.9454783	0.9668799*	0.9453714	0.9666814*
DIFF	0.9454783	0.9829008*	0.9453714	0.9827104*
P1	0.9454783	1.0007217*	0.9453714	1.0004884*

(reference: $k_{eff} = 0.978 \pm 0.0006$)
(* the desired k-eff/flux residual tolerance of 1×10^{-6} could not be achieved)

We also note that our predictions of the different angular methods–that odd polar cosine moments have no influence on the scalar flux due to the use of Fick's law–

are confirmed. Although not shown, the power profiles of the "isotropic" and "linear" leakage approximations are identical. Also, the power profiles of the "quadratic", "diffusion", and "P_1" leakage approximations are identical. This is only true when axial splitting in disabled, because when enabled, each leakage method uses a unique splitting logic. With this confirmed, we will only consider the "isotropic" and "quadratic" leakage approximations for the other benchmarks.

The errors of these eigenvalues when compared to the benchmark are shown below in Table 5. We see that, as expected, this problem is very 3D in nature and is therefore difficult to accurately solve with the 2D/1D method. The use of transverse leakage splitting leads to a large variance in the solution, with different values occurring for all angular approximations due to the different logic being used for each method.

Table 5: The Finite Difference Eigenvalue Error in pcm for the Unrodded Configuration

Shape Function	FLAT	FLAT	FLUX	FLUX
Leakage Splitting?	FALSE	TRUE	FALSE	TRUE
ISO	-2733.72	-2027.16	-2741.68	-2034.83
LIN	-2733.72	-375.66	-2741.68	-382.57
QUAD	-3252.17	-1112.01	-3262.86	-1131.86
DIFF	-3252.17	490.08	-3262.86	471.04
P1	-3252.17	2272.17	-3262.86	2248.84

Next, we consider the results when using nodal methods rather than finite difference methods for the unrodded configuration. In Table 6, we see the eigenvalues; in Table 7, we see the associated errors.

Table 6: The Nodal Eigenvalue Results for the Unrodded Configuration

Shape Function	FLAT	FLAT	FLUX	FLUX
Leakage Splitting?	FALSE	TRUE	FALSE	TRUE
ISO	DNC	0.9160434*	DNC	0.9173312*
LIN	DNC	DNC	DNC	DNC
QUAD	DNC	0.9766204*	DNC	0.9836573*
DIFF	DNC	0.9775694*	DNC	0.9820469*
P1	DNC	DNC	DNC	DNC

(reference: $k_{eff} = 0.978 \pm 0.0006$)
(* the desired k-eff/flux residual tolerance of 1×10^{-6} could not be achieved)
(DNC: Did Not Converge)

Unfortunately, we see that this problem poses a tremendous challenge for the nodal method used with 2D/1D, as no cases converged successfully. For the few that did manage partial convergence, some cases did produce good estimates of the eigenvalue. Given the issues observed with other methods within this test matrix subset, we do not have great confidence in these results.

Table 7: The Nodal Eigenvalue Error in pcm for the Unrodded Configuration

Shape Function	FLAT	FLAT	FLUX	FLUX
Leakage Splitting?	FALSE	TRUE	FALSE	TRUE
ISO	DNC	-6195.66	DNC	-6066.88
LIN	DNC	DNC	DNC	DNC
QUAD	DNC	-137.96	DNC	565.73
DIFF	DNC	-43.06	DNC	404.69
P1	DNC	DNC	DNC	DNC

(DNC: Did Not Converge)

We see that the nodal methods have great difficulty with convergence for this problem. In the next section, we will see that the convergence issues are lessened in the rodded configuration. We can deduce that the void region (not well approximated by diffusion theory) is the culprit for these issues.

5.2.2 The Rodded Configuration

The eigenvalues produced by the various methods for the rodded configuration with finite difference leakage methods are shown below in Table 8. The same patterns persist from the previous case, with the exception of the diffusion angular approximation converging when axial leakage splitting is enabled.

Table 8: The Finite Difference Eigenvalue Results for the Rodded Configuration

Shape Function	FLAT	FLAT	FLUX	FLUX
Leakage Splitting?	FALSE	TRUE	FALSE	TRUE
ISO	0.9487457	0.9519845	0.9486799	0.9519225
LIN	0.9487457	0.9702874	0.9486799	0.9702272
QUAD	0.9435999	0.9549328*	0.9435247	0.9548492*
DIFF	0.9435999	0.9728765	0.9435247	0.9728006
P1	0.9435999	0.9919363*	0.9435247	0.9918602*

(reference: $k_{eff} = 0.9624 \pm 0.0006$)

(* the desired k-eff/flux residual tolerance of 1×10^{-6} could not be achieved)

The errors of these eigenvalues when compared to the benchmark are shown below in Table 9. With the control rod inserted, the 2D/1D method performs better, due to the removal of the void region. Regardless, the method is greatly challenged. For both cases, we see that the higher order leakage approximation seems to be less accurate than the lower order counterparts. Also, the "scalar flux" shape function has negligible effect on the solution, marginally increasing the error. For both of these counterintuitive results, it is possible that this is a removal of cancellation of error

Table 9: The Eigenvalue Error in pcm for the Rodded Configuration

Shape Function	FLAT	FLAT	FLUX	FLUX
Leakage Splitting?	FALSE	TRUE	FALSE	TRUE
ISO	-1365.43	-1041.55	-1372.01	-1047.75
LIN	-1365.43	788.74	-1372.01	782.72
QUAD	-1880.01	-746.72	-1887.53	-755.08
DIFF	-1880.01	1047.65	-1887.53	1040.06
P1	-1880.01	2953.63	-1887.53	2946.02

Next, we consider the results obtained using nodal methods rather than finite difference methods for the unrodded configuration. In Table 10, we see the eigenvalues; in Table 11, we see the associated errors.

Table 10: The Nodal Eigenvalue Results for the Rodded Configuration

Shape Function	FLAT	FLAT	FLUX	FLUX
Leakage Splitting?	FALSE	TRUE	FALSE	TRUE
ISO	0.9498518	0.9586234*	0.9497863	0.9584979*
LIN	0.9498518	1.0265975*	0.9497863	1.0291577*
QUAD	DNC	0.9811197*	DNC	0.9828844*
DIFF	DNC	1.0981441*	DNC	DNC
P1	DNC	1.1097580*	DNC	1.1110824*

(reference: $k_{eff} = 0.9624 \pm 0.0006$)
(* the desired k-eff/flux residual tolerance of 1×10^{-6} could not be achieved)
(DNC: Did Not Converge)

Table 11: The Nodal Eigenvalue Error in pcm for the Rodded Configuration

Shape Function	FLAT	FLAT	FLUX	FLUX
Leakage Splitting?	FALSE	TRUE	FALSE	TRUE
ISO	-1254.82	-377.66	-1261.37	-390.21
LIN	-1254.82	6419.75	-1261.37	6675.77
QUAD	DNC	1871.97	DNC	2048.44
DIFF	DNC	13574.41	DNC	DNC
P1	DNC	14735.80	DNC	14868.24

(DNC: Did Not Converge)

As with the unrodded configuration, convergence issues persist, but the nodal methods do possess better accuracy than their finite difference counterparts for this configuration. The "isotropic" and "linear" approximations produce identical solutions with leakage splitting disabled, confirming that the axial differencing method does not affect this symmetry fact. Again, this feature is purely due to the use of a Fick's law approximation; it is present in both the finite difference and nodal diffusion methods.

The Takeda Benchmark specification only details the group average material fluxes; whereas the standard output of MPACT was designed to specify power distributions.

Thus, we only have the eigenvalue to compare our method to the benchmark. Not surprisingly, the strong material gradients challenge the 2D/1D method greatly.

5.3 The C5G7 Extended Benchmark

The original C5G7 benchmark [22] provided heterogeneous 2D and 3D problems that reasonably represent realistic reactors. A multitude of numerical codes (both deterministic and Monte Carlo) were used to generate the benchmark standard. Two years later, an extension of these problems [23] was generated that includes absorbing control rods uninserted, partially inserted, and moderately inserted into the core. We apply the 2D/1D method with the various leakage approximations to the extended C5G7 benchmark problems.

The following figures are from the extended benchmark [23] and illustrate the pin and reactor geometry. In Figure 27, the region surrounding and above the fuel is just moderator. In the unrodded (Figure 31), rodded-A (Figure 32), and rodded-B (Figure 33) configurations, the shaded region of the corresponding figures denotes the presence of control rods inserted into the region.

5.4 Results of 2D/1D Applied to the C5G7 Benchmark

In MPACT, twenty cases were simulated for each of the three rod configurations. The problem was divided into eighteen planes, each $3.57cm$ thick. The rodded pin cells had five annular divisions in the fuel/absorber/guide tube region and two in the moderator region, with eight azimuthal divisions in each to form the flat source regions. The unrodded pin cells were divided into 25 square flat source regions. A Chebyshev-Gauss product quadrature was again used with 16 azimuthal angles per quarter and 4 polar angles per half for the 2D MOC, with a ray spacing of 0.05 cm.

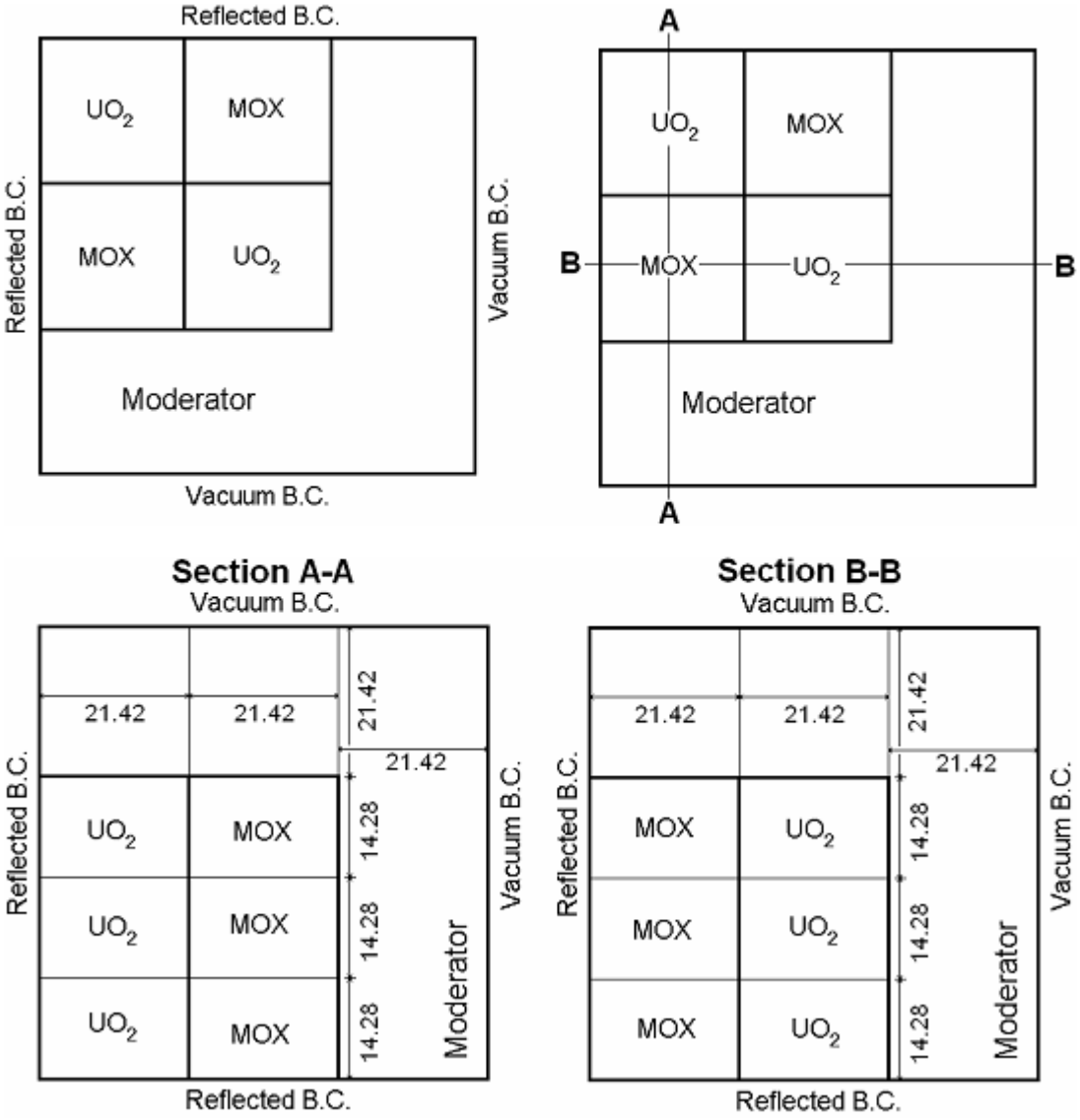

Figure 27: The Extended C5G7 Core Configuration [23]

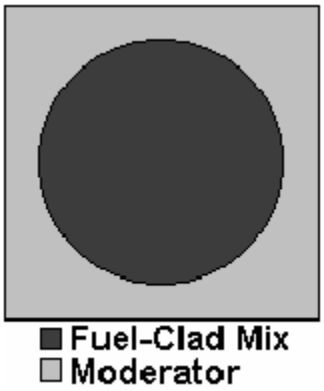

Figure 28: The C5G7 Pin Structure [23]

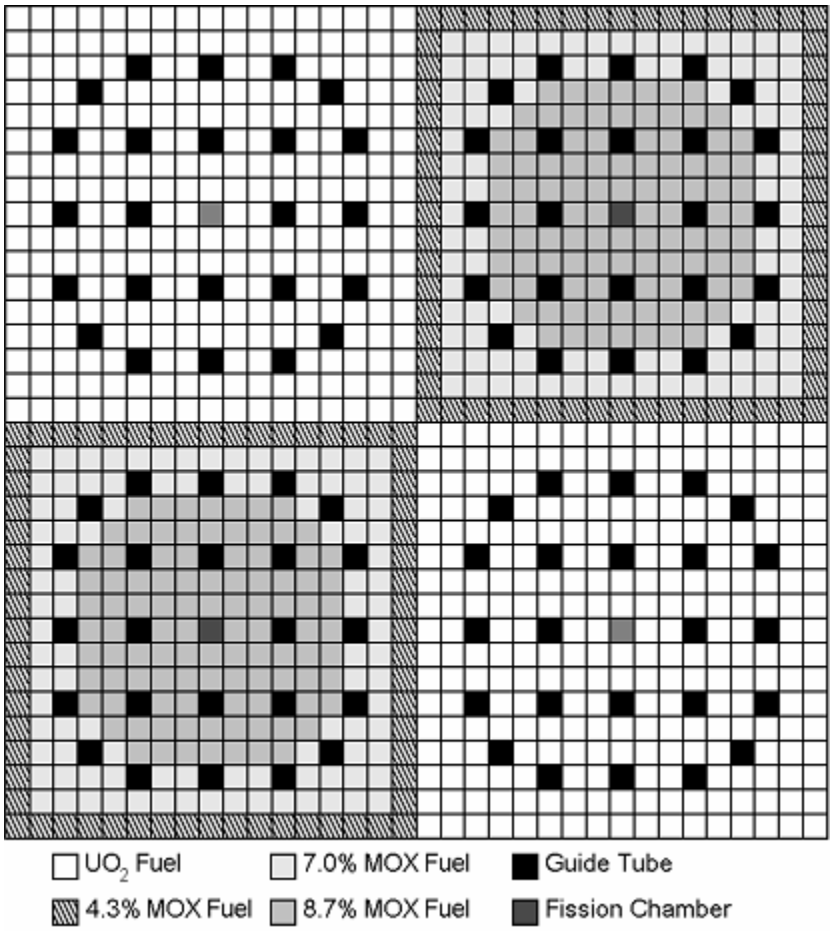

Figure 29: The C5G7 Assembly Pin Arrangement [23]

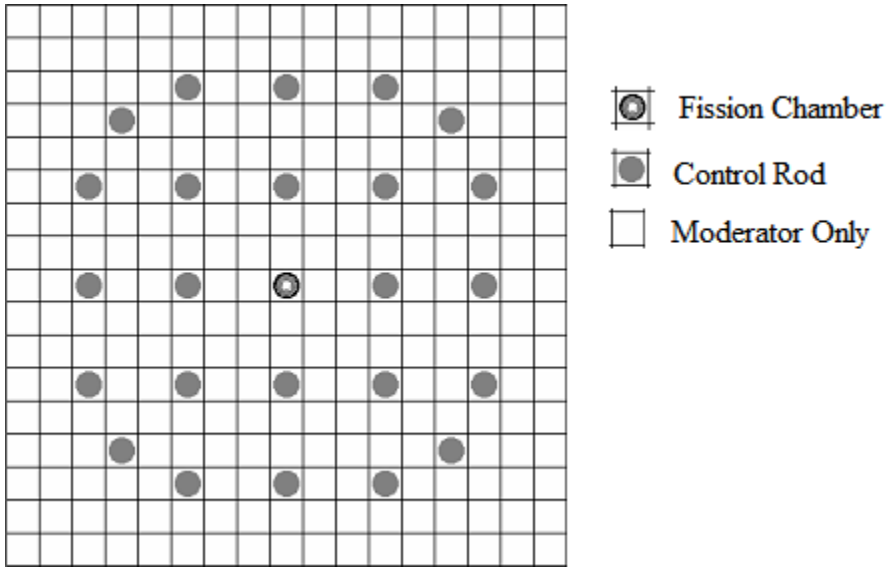

Figure 30: The Extended C5G7 Reflector Pin Arrangement [23]

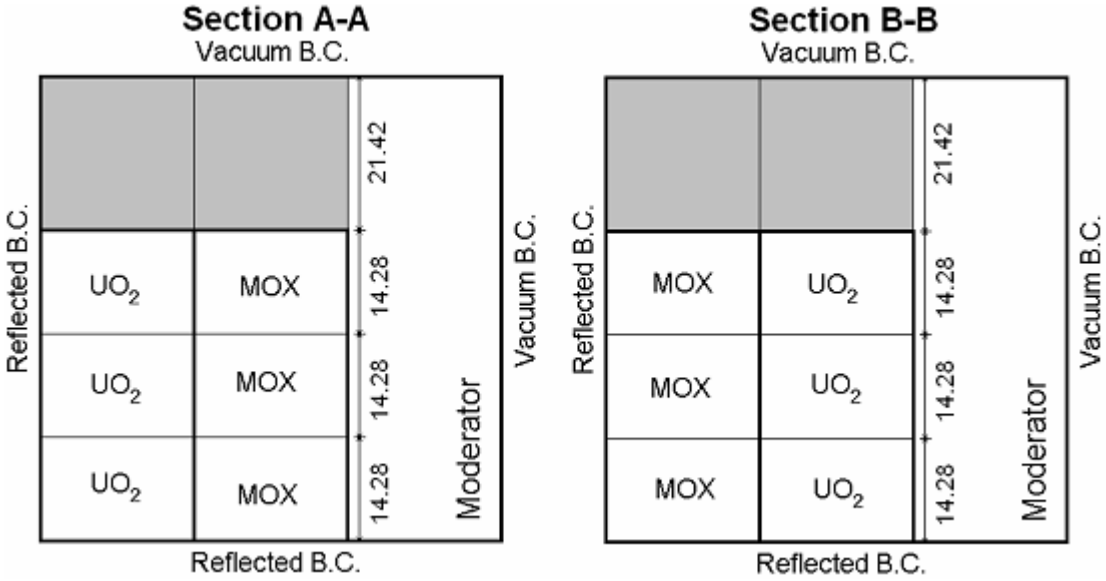

Figure 31: The Extended C5G7 Unrodded Core Configuration [23]

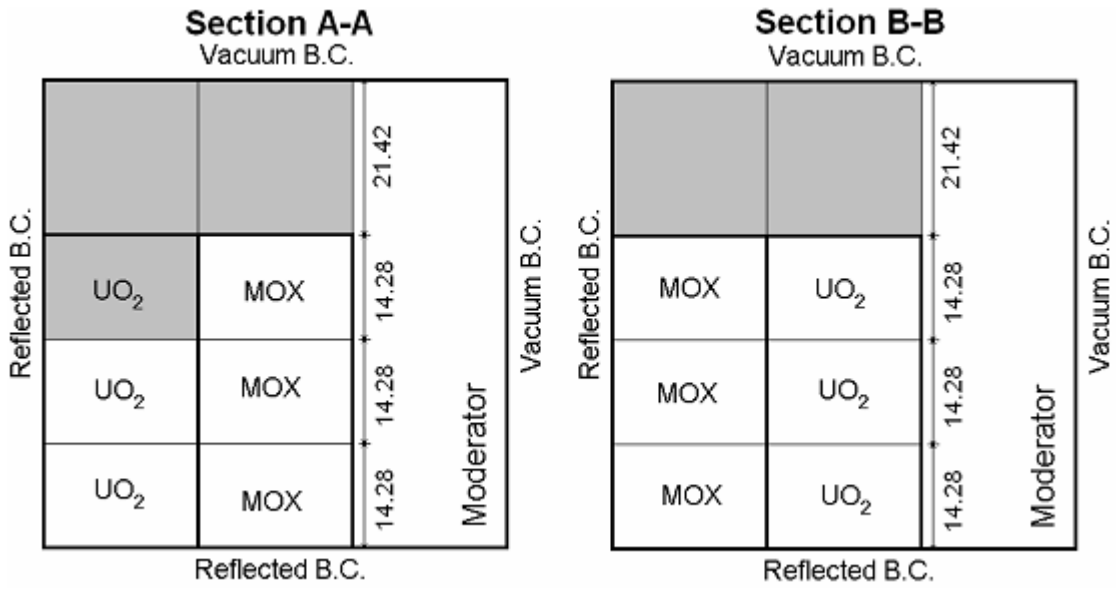

Figure 32: The Extended C5G7 Rodded-A Core Configuration [23]

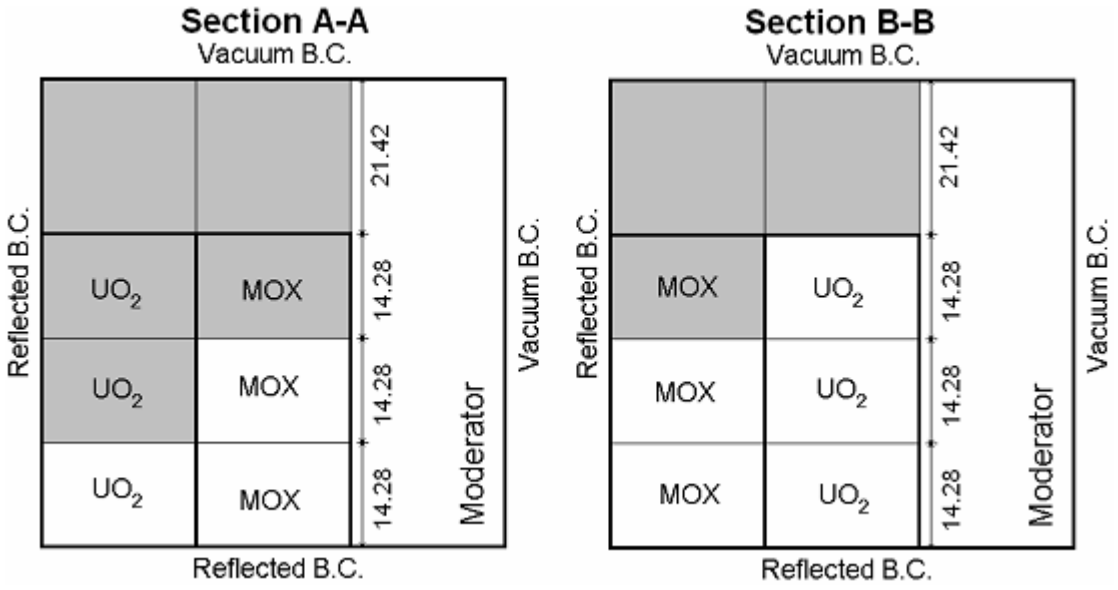

Figure 33: The Extended C5G7 Rodded-B Core Configuration [23]

5.4.1 The Unrodded Configuration

The eigenvalues and their errors compared to the benchmark for the unrodded configuration are shown in Table 12 and Table 13, respectively. We see that the higher-order leakage approximations seem to be less accurate than the lower-order counterparts–we presume that this is a removal of error cancellation. The nodal methods are also consistently more accurate than the finite difference methods. In addition, the inclusion of the flux shape function has little bearing on the result, as was the case in Chapter 4. Surprisingly, for the unrodded case, splitting the leakage to maintain positivity of the source universally improves the accuracy of the eigenvalue.

Table 12: The Eigenvalue Results for the Unrodded Configuration

Shape Function	FLAT	FLAT	FLUX	FLUX
Leakage Splitting?	FALSE	TRUE	FALSE	TRUE
ISO-FD	1.1416391	1.1418438	1.1416266	1.1418277
ISO-NODAL	1.1419941	1.1422042	1.1419794	1.1421855
QUAD-FD	1.1411530	1.1417664	1.1411310	1.1417339
QUAD-NODAL	1.1414666	1.1421031	1.1414360	1.1420609

(reference: $k_{eff} = 1.14308 \pm 0.006\%$)

Table 13: The Eigenvalue Error in pcm for the Unrodded Configuration

Shape Function	FLAT	FLAT	FLUX	FLUX
Leakage Splitting?	FALSE	TRUE	FALSE	TRUE
ISO-FD	-144.09	-123.62	-145.34	-125.23
ISO-NODAL	-108.59	-87.58	-110.06	-89.45
QUAD-FD	-192.70	-131.36	-194.90	-134.61
QUAD-NODAL	-161.34	-97.69	-164.40	-101.91

Table 14 summarizes the power profile information for the "isotropic" leakage approximations with nodal diffusion, a "flat" shape function, and leakage splitting enabled. We see that the maximum pin power for each of the three axial fuel regions is quite accurate; the third plane (closest to the problem boundary) has the most error and is most likely due to the axial diffusion boundary conditions that exist with the 2D/1D approximation. Overall, the errors associated with the pin power distribution are within 3%.

Table 14: The Power Profile Accuracy for the Unrodded Configuration Solved with "Isotropic" Leakage, Nodal Diffusion, a "Flat" Shape Function, and Leakage Splitting Enabled

	Z Slice #1 Reference	Z Slice #1 User	Z Slice #2 Reference	Z Slice #2 User	Z Slice #3 Reference	Z Slice #3 User	Overall Reference	Overall User
Specific Pin Power Data								
Maximum Pin Power	1.108	1.108	0.882	0.879	0.491	0.484	2.481	2.471
Percent Error (associated 68% MC)	0.090	-0.008	0.100	-0.408	0.130	-1.298	0.060	-0.406
Distribution Percent Error Results								
Maximum Error (associated 68% MC)	0.290	2.803	0.320	2.518	0.430	1.582	0.192	2.339
AVG Error	0.164	0.611	0.183	0.473	0.245	0.680	0.109	0.432
RMS Error	0.171	0.845	0.190	0.675	0.255	0.765	0.114	0.614
MRE Error	0.062	0.173	0.055	0.129	0.042	0.158	0.093	0.336
Number of Accurate Fuel Pin Powers								
Number of Fuel Pins Within 68% MC	371	107	371	140	371	98	371	104
Number of Fuel Pins Within 95% MC	518	206	518	276	518	180	518	185
Number of Fuel Pins Within 99% MC	540	262	540	331	540	254	540	233
Number of Fuel Pins Within 99.9% MC	544	324	544	392	544	299	544	281
Total Number of Fuel Pins	545	545	545	545	545	545	545	545
Average Pin Power In Each Assembly								
UO2-1 Power	219.04	219.01	174.24	173.68	97.93	96.95	491.21	489.65
MOX Power	94.53	95.06	75.25	75.42	42.92	42.69	212.70	213.17
UO2-2 Power	62.12	62.64	49.45	49.69	27.82	27.68	139.39	140.01
UO2-1 Power Percent Error	0.082	-0.013	0.073	-0.319	0.055	-1.002	0.123	-0.319
MOX Power Percent Error	0.061	0.559	0.054	0.225	0.041	-0.529	0.092	0.221
UO2-2 Power Percent Error	0.043	0.846	0.038	0.484	0.029	-0.506	0.065	0.448

5.4.2 The Rodded-A Configuration

The eigenvalues and their errors compared to the benchmark for the rodded-A configuration are shown in Table 15 and Table 16, respectively. Again, we see that the use of leakage splitting improves the accuracy of the method in calculating the eigenvalue. This may occur as the splitting process generates an implicit shape function.

Table 15: The Eigenvalue Results for the Rodded-A Configuration

Shape Function	FLAT	FLAT	FLUX	FLUX
Leakage Splitting?	FALSE	TRUE	FALSE	TRUE
ISO-FD	1.1273792	1.1275939	1.1273743	1.1275852
ISO-NODAL	1.1270744	1.1272912	1.1270785	1.1272914
QUAD-FD	1.1267410	1.1273839	1.1267559	1.1273879
QUAD-NODAL	1.1261915	1.1268471	1.1262464	1.1268901

(reference: $k_{eff} = 1.12806 \pm 0.006\%$)

Table 16: The Eigenvalue Error in pcm for the Rodded-A Configuration

Shape Function	FLAT	FLAT	FLUX	FLUX
Leakage Splitting?	FALSE	TRUE	FALSE	TRUE
ISO-FD	-68.08	-46.61	-68.57	-47.48
ISO-NODAL	-98.56	-76.88	-98.15	-76.86
QUAD-FD	-131.90	-67.61	-130.41	-67.21
QUAD-NODAL	-186.85	-121.29	-181.36	-116.99

Table 17 summarizes the power profile information for the "isotropic" leakage approximations with nodal diffusion, a "flat" shape function, and leakage splitting enabled. We see that the maximum pin power for each of the three axial fuel regions is quite accurate; the presence of the control rods has improved the accuracy of the third plane (the one with the worst error in the unrodded configuration). Overall, the errors associated with the pin power distribution are again within 3%. Compared to the unrodded case, we see that more of the individual pins are within the Monte Carlo solution statistical errors. From this, we can presume that the guide tubes, being void, present more difficulty for the 2D/1D approximation than the control rods. This intuitively makes sense as the control rods, although heavily absorbing, have a much larger collision cross section and are more diffusive in comparison.

Table 17: The Power Profile Accuracy for the Rodded-A Configuration Solved with "Isotropic" Leakage, Nodal Diffusion, a "Flat" Shape Function, and Leakage Splitting Enabled

	Z Slice #1 Reference	Z Slice #1 User	Z Slice #2 Reference	Z Slice #2 User	Z Slice #3 Reference	Z Slice #3 User	Overall Reference	Overall User
Specific Pin Power Data								
Maximum Pin Power	1.197	1.190	0.832	0.828	0.304	0.305	2.253	2.243
Percent Error (associated 68% MC)	0.080	-0.554	0.100	-0.450	0.200	0.332	0.059	-0.485
Distribution Percent Error Results								
Maximum Error (associated 68% MC)	0.210	2.246	0.310	2.430	0.220	1.380	0.183	2.069
AVG Error	0.157	0.536	0.180	0.471	0.260	0.353	0.108	0.412
RMS Error	0.163	0.725	0.186	0.654	0.266	0.441	0.111	0.574
MRE Error	0.066	0.200	0.056	0.137	0.037	0.051	0.094	0.334
Number of Accurate Fuel Pin Powers								
Number of Fuel Pins Within 68% MC	371	97	371	140	371	232	371	95
Number of Fuel Pins Within 95% MC	518	179	518	258	518	403	518	181
Number of Fuel Pins Within 99% MC	540	252	540	311	540	476	540	234
Number of Fuel Pins Within 99.9% MC	544	315	544	381	544	513	544	283
Total Number of Fuel Pins	545	545	545	545	545	545	545	545
Average Pin Power In Each Assembly								
UO2-1 Power	237.41	236.61	167.51	166.90	56.26	56.19	461.18	459.70
MOX Power	104.48	104.85	78.01	78.17	39.23	39.15	221.71	222.17
UO2-2 Power	69.80	70.23	53.39	53.62	28.21	28.11	151.39	151.97
UO2-1 Power Percent Error	0.087	-0.338	0.071	-0.364	0.040	-0.120	0.119	-0.321
MOX Power Percent Error	0.065	0.352	0.056	0.213	0.040	-0.203	0.094	0.205
UO2-2 Power Percent Error	0.047	0.621	0.040	0.438	0.029	-0.341	0.068	0.377

5.4.3 The Rodded-B Configuration

The eigenvalues and their errors compared to the benchmark for the rodded-B configuration are shown in Table 18 and Table 19, respectively. The same patterns persist as for the rodded-A case: (i) better results with lower-order leakage, (ii) negligible change/improvement when using the flux shape functions, and (iii) leakage splitting improves the eigenvalue solution.

Table 18: The Eigenvalue Results for the Rodded-B Configuration

Shape Function	FLAT	FLAT	FLUX	FLUX
Leakage Splitting?	FALSE	TRUE	FALSE	TRUE
ISO-FD	1.0774628	1.0777238	1.0774706	1.0777272
ISO-NODAL	1.0761943	1.0764548	1.0762326	1.0764886
QUAD-FD	1.0764876	1.0772709	1.0765603	1.0773308
QUAD-NODAL	1.0744857	1.0752708	1.0746901	1.0754617

(reference: $k_{eff} = 1.07777 \pm 0.006\%$)

Table 19: The Eigenvalue Error in pcm for the Rodded-B Configuration

Shape Function	FLAT	FLAT	FLUX	FLUX
Leakage Splitting?	FALSE	TRUE	FALSE	TRUE
ISO-FD	-30.72	-4.62	-29.94	-4.28
ISO-NODAL	-157.57	-131.52	-153.74	-128.14
QUAD-FD	-128.24	-49.91	-120.97	-43.92
QUAD-NODAL	-328.43	-249.92	-307.99	-230.83

Table 20 summarizes the power profile information for the "isotropic" leakage approximations with nodal diffusion, a "flat" shape function, and leakage splitting enabled. We see that the maximum pin power for each of the three axial fuel regions is again quite accurate; the deeper insertion of the control rods has further harmed the accuracy of the first plane, but improved the accuracy of the second and third plane. Overall, the errors associated with the pin power distribution are again within 3%. Compared to the previous two cases, we see that even more of the individual pins are within the Monte Carlo solution statistical errors. This further confirms our prior statements that void regions present the greatest challenge to the 2D/1D approximation.

Table 20: The Power Profile Accuracy for the Rodded-B Configuration Solved with "Isotropic" Leakage, Nodal Diffusion, a "Flat" Shape Function, and Leakage Splitting Enabled

	Z Slice #1 Reference	Z Slice #1 User	Z Slice #2 Reference	Z Slice #2 User	Z Slice #3 Reference	Z Slice #3 User	Overall Reference	Overall User
Specific Pin Power Data								
Maximum Pin Power	1.200	1.185	0.554	0.554	0.217	0.217	1.835	1.825
Percent Error (associated 68% MC)	0.090	-1.284	0.150	0.009	0.240	-0.136	0.083	-0.545
Distribution Percent Error Results								
Maximum Error (associated 68% MC)	0.240	2.734	0.260	2.392	0.380	2.593	0.157	2.427
AVG Error	0.146	0.686	0.181	0.463	0.285	0.758	0.105	0.535
RMS Error	0.150	0.852	0.184	0.681	0.290	0.920	0.108	0.711
MRE Error	0.073	0.398	0.055	0.119	0.034	0.083	0.098	0.480
Number of Accurate Fuel Pin Powers								
Number of Fuel Pins Within 68% MC	371	78	371	171	371	103	371	75
Number of Fuel Pins Within 95% MC	518	150	518	314	518	219	518	155
Number of Fuel Pins Within 99% MC	540	184	540	372	540	290	540	190
Number of Fuel Pins Within 99.9% MC	544	227	544	418	544	376	544	224
Total Number of Fuel Pins	545	545	545	545	545	545	545	545
Average Pin Power In Each Assembly								
UO2-1 Power	247.75	245.30	106.56	106.67	41.12	41.23	395.43	393.19
MOX Power	125.78	125.81	81.41	81.70	29.42	29.73	236.62	237.24
UO2-2 Power	91.64	92.10	65.02	65.41	30.68	30.82	187.34	188.33
UO2-1 Power Percent Error	0.091	-0.988	0.056	0.100	0.035	0.259	0.112	-0.565
MOX Power Percent Error	0.073	0.017	0.058	0.364	0.034	1.035	0.100	0.263
UO2-2 Power Percent Error	0.055	0.498	0.046	0.599	0.032	0.472	0.078	0.529

5.5 CASL VERA 3A Milestone Problem

The final simulation we consider comes from the Advanced Modeling Applications (AMA) branch of CASL [24]. Of the five core physics problems described, we consider the 3D assembly–specifically, the first case with no absorber rods. This problem is the most realistic of the three, with sixty energy groups. Due to the detailed isotopics and fine energy grouping of this model, a critical step to the correct solution of this model is the resonance calculation; within MPACT, the subgroup method [25] is used to perform these resonance calculations. We use this method as a "black-box" to obtain better results.

This assembly is a 17x17 grid of fuel rods, guide tubes, and an instrumentation tube as shown in Figure 34. These pins have three material regions: pin interior (e.g. fuel), clad, and moderator.

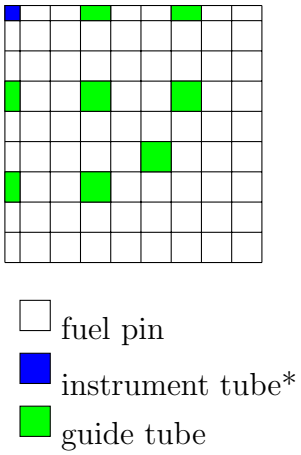

Figure 34: The Quarter Assembly Configuration of the VERA 3A Benchmark
* The instrument tube is the center of the assembly.

Figure 35 is from the benchmark document to show the axial distribution of materials in the assembly.

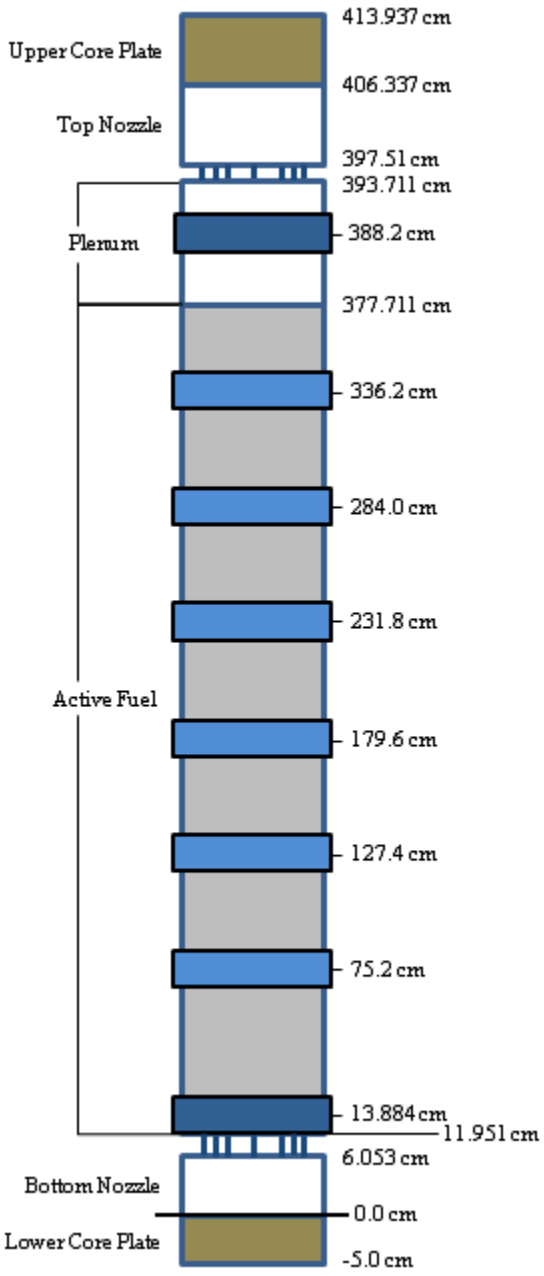

Figure 35: The VERA 3A Benchmark Assembly Axial Geometry [24]

5.6 Results of 2D/1D Applied to the CASL VERA 3A Milestone Problem

In MPACT, twenty cases were performed for this benchmark. The problem was divided into 58 axial planes of variable thickness to match the problem geometry. The rodded pin cells had three annular divisions in the fuel/absorber/guide tube region and one each in the clad and moderator region, with eight azimuthal divisions in each to form the flat source regions. The unrodded pin cells were divided into 16 square flat source regions (4 for quarter pin cells). Again, we use a Chebyshev-Gauss quadrature, but with 8 azimuthal angles per quadrant and two polar angles per half for the 2D MOC, with a ray spacing of 0.05 cm. Unlike the previous benchmarks, the VERA 3A Benchmark has a great deal of axial heterogeneity, with six grid spacers within the fuel region and more structural components above and below the fuel assembly. Because of this, we expect this benchmark to challenge the 2D/1D approximation in a way different than the cases we have studied thus far.

Running this problem, we see that the eigenvalue results are similar for all methods considered. The nodal methods perform better overall, with shape functions and axial leakage having little effect. Because enabling leakage splitting has little effect, we presume that, for this problem, splitting to maintain a positive source occurs very infrequently.

Table 21: The Eigenvalue Results for VERA 3A Benchmark

Shape Function	FLAT	FLAT	FLUX	FLUX
Leakage Splitting?	FALSE	TRUE	FALSE	TRUE
ISO-FD	1.1709894	1.1709895	1.1709893	1.1709893
ISO-NODAL	1.1710347	1.1710347	1.1710345	1.1710346
QUAD-FD	1.1709670	1.1709672	1.1709668	1.1709671
QUAD-NODAL	1.1710124	1.1710126	1.1710122	1.1710125

(reference: $k_{eff} = 1.176286 \pm 0.00001$)

Examining the 2D radial and 1D axial power profiles, we find again that the isotropic leakage, with nodal diffusion, a "flat" shape function, and axial leakage

Table 22: The Eigenvalue Error in pcm for the VERA 3A Benchmark

Shape Function	FLAT	FLAT	FLUX	FLUX
Leakage Splitting?	FALSE	TRUE	FALSE	TRUE
ISO-FD	-473.26	-473.25	-473.27	-473.27
ISO-NODAL	-468.73	-468.73	-468.75	-468.74
QUAD-FD	-475.50	-475.48	-475.52	-475.49
QUAD-NODAL	-470.96	-470.94	-470.98	-470.95

splitting enabled produces the best results. The following tables and figures show these results and the relative error when compared to the benchmark solution. In Table 23 and Table 24, the pin powers are shown for the pin configuration shown in Figure 34.

Table 23: The 2D Radial Pin Powers for VERA 3A Benchmark

–	1.0348	1.0356	–	1.0346	1.0310	–	1.0113	0.9771
1.0348	1.0097	1.0099	1.0357	1.0092	1.0063	1.0254	0.9887	0.9729
1.0356	1.0099	1.0108	1.0376	1.0118	1.0090	1.0266	0.9884	0.9724
–	1.0357	1.0376	–	1.0441	1.0437	–	1.0109	0.9748
1.0346	1.0092	1.0118	1.0441	1.0322	1.0497	1.0350	0.9840	0.9656
1.0310	1.0063	1.0090	1.0437	1.0497	–	1.0167	0.9658	0.9561
–	1.0254	1.0266	–	1.0350	1.0167	0.9745	0.9496	0.9472
1.0113	0.9887	0.9884	1.0109	0.9840	0.9658	0.9496	0.9405	0.9428
0.9771	0.9729	0.9724	0.9748	0.9656	0.9561	0.9472	0.9428	0.9480

Table 24: The 2D Radial Pin Power Relative Errors in pcm for the VERA 3A Benchmark

–	-80.14	-63.69	–	-29.95	-75.60	–	12.86	-3.07
-80.14	13.87	-6.93	-78.15	13.87	22.86	-15.60	40.47	1.03
-63.69	-6.93	13.85	-56.83	11.86	-13.87	-44.79	-2.02	-7.20
–	-78.15	-56.83	–	-14.36	-60.33	–	2.97	21.55
-29.95	13.87	11.86	-14.36	47.49	-27.62	1.93	49.82	10.36
-75.60	22.86	-13.87	-60.33	-27.62	–	7.87	19.68	26.15
–	-15.60	-44.79	–	1.93	7.87	61.61	55.84	44.36
12.86	40.47	-2.02	2.97	49.82	19.68	55.84	79.81	25.46
-3.07	1.03	-7.20	21.55	10.36	26.15	44.36	25.46	14.77

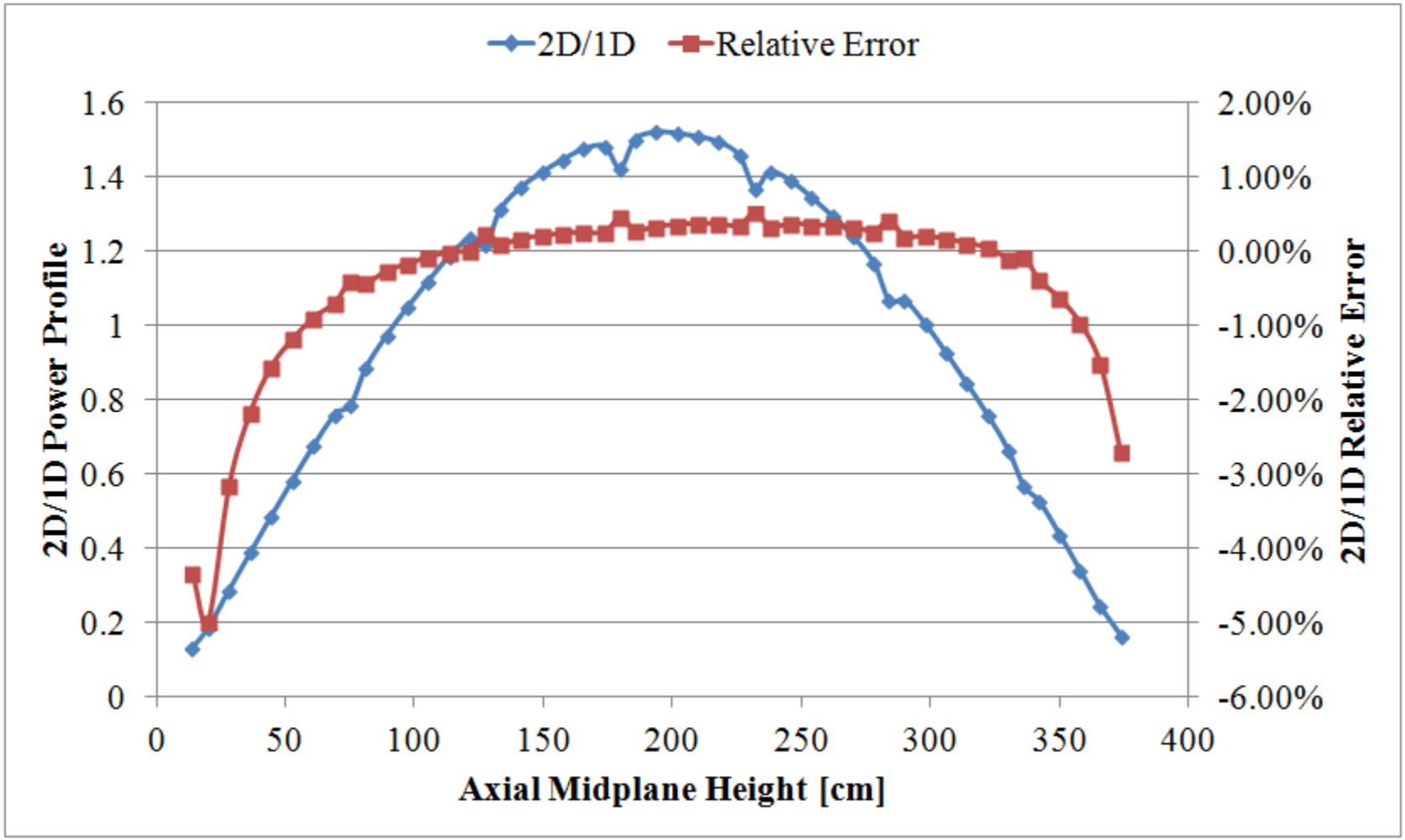

Figure 36: The 1D Axial Core Power Profile for the VERA 3A Benchmark

Chapter 6

Conclusion

In this thesis we have proposed a basic mathematical foundation for the 2D/1D methodology in DeCART and MPACT. The starting point of our analysis is a 2D/1D equation – a second-order integrodifferential equation that approximates the linear 3D Boltzmann equation only in its axial leakage term. Many approximations to the axial leakage are possible; in this thesis we have treated the five simplest: (i) isotropic, (ii) linear, (iii) quadratic, (iv) diffusion, (v) and P_1. By systematically discretizing the 2D/1D equation in each of its independent variables, and then by formulating and Fourier-analyzing various iterative methods for solving the discrete equations, we obtain computational methods that (i) iteratively converge for each fixed grid, and (ii) also converge as the grid is refined – to the analytic solution of the original 2D/1D equation. Numerical results confirm these theoretical predictions and show that for 3D problems in which the standard diffusion approximation is valid, the 2D/1D and linear Boltzmann equations yield highly similar solutions. Furthermore, applying this method to benchmark problems, we see good agreement for reactor-like problems–those with radial heterogeneity and weak axial derivatives of the angular flux.

The theory presented in this thesis fulfills two goals:

1. By using the 2D/1D equation as the starting point, numerical 2D/1D solutions can be interpreted in the limit as the numerical grids become fine: these solutions

will consistently limit to the analytic solution of the continuous 2D/1D equation – which approximates the Boltzmann equation more accurately than the standard diffusion equation. (Without an underlying integro-differential equation as a starting point, it is not evident that a discretization method will possess a limiting solution as the grids are refined.)

2. By using a standard Fourier analysis, stable iteration methods have been developed for solving the consistently-discretized 2D/1D equations.

Both of these goals are confirmed by the numerical results.

The following issues should be kept in mind:

1. If the angular discretizations of L_z and ψ satisfy Eq. (3.1b), then the angularly-discretized 2D/1D Eq. (3.1) becomes identical to the angularly-discretized linear Boltzmann equation. Thus, by systematically increasing the accuracy of the angular dependence of the axial leakage term, the solution of the *continuous* 2D/1D equation should systematically limit to the solution of the *continuous* Boltzmann equation.

2. As the angular complexity of the transverse leakage term increases, the amount of information that must be passed between processors will increase, and the parallel efficiency of the resulting method will decrease. Thus, there is a tradeoff between accuracy and parallelizability.

3. An extra degree of complexity occurs because of the fine and coarse radial spatial grids: no amount of angular refinement will cause the discrete 2D/1D solution to limit to the discrete Boltzmann solution unless all the spatial grids are refined.

To summarize the results of our numerical simulations, they show that the 2D/1D solutions treat "radial" boundary layers (along surfaces whose normals point in a radial direction) with transport accuracy, and "axial" boundary layers (along surfaces whose normals point in an axial direction) with at worst diffusion accuracy. If an axial boundary layer contains strong radial derivatives, then the accuracy of the 2D/1D solution actually increases. This is all that one would hope for, from solving

an equation that preserves the correct transport physics in the radial directions and the approximate diffusion physics in the axial direction.

Our simulations also confirm that a key element of stability of the 2D/1D iteration scheme is the under-relaxation step. Under-relaxation is never used for iteratively solving standard S_N calculations; the necessary inclusion of this step for solving the 2D/1D equation demonstrates a fundamental difference between this equation and the Boltzmann transport equation.

If the under-relaxation step is not performed, the iteration method used in our simulations becomes quite similar to the original iteration method used in DeCART – and it becomes unstable for sufficiently small Δ_z. This true for both the "source iteration" and CMFD accelerated method, with the "source iteration" method being more sensitive to instability and requiring more under-relaxation to guarantee stability.

In MPACT, the radial transport solver of the 2D/1D equation itself is discretized on the fine radial grid, and the axial leakage of the 2D/1D equation and low-order "diffusion" equation in the CMFD method is discretized consistently on the coarse radial grid. The axial leakage of the 2D/1D equation on a coarse grid results in the need to employ shape functions in order to reduce this error. We employed the "scalar flux" shape function as an improvement over the lack of a shape function ("flat") but found little improvement. This agrees with the findings of another MPACT developer [20], who noted that in order to get a shape function to work with the 2D/1D fusion method, at least first-order Chebyshev moments of the azimuthal angle must be included.

The resulting 2D/1D solutions are not identical to solutions of the 3D Boltzmann transport equation, because the 2D/1D physics in the axial direction is diffusion not transport. However, more accurate approximations to the axial derivative term can be envisioned, as was discussed in Chapter 3. In particular, approximations more sophisticated than P_1 (for example, P_3) can be used. In fact, the current KAERI version of DeCART now uses an SP_3 approximation to the transverse leakage term [11].

The main point to emphasize is that many different possibilities exist for approximating the axial leakage term in the 3D Boltzmann transport equation, so that the resulting "2D/1D" equation (i) models practical reactor core problems with sufficient accuracy, and (ii) can be solved more efficiently than the standard 3D Boltzmann transport equation. We discuss some of these possibilities next.

6.1 Future Work

The theory presented here is developed for only the five "simplest" 2D/1D equations; for the 1D axial diffusion discretization, we use either (i) a standard finite-difference approximation, or (ii) a nodal approximation; for iteration schemes, we consider a relatively simple "Source Iteration" method with under-relaxation and a CMFD accelerated method, also with under-relaxation. The theory presented here certainly does not include all possible improvements to the 2D/1D method. For the theory to become more applicable to realistic reactor core problems than in its current form, it could be improved in the following ways.

6.1.1 Diffusion Coefficient

The standard diffusion coefficient in Eq. (3.34) can be directly applied to problems with radial spatial variation of the type found in reactor cores. This basic procedure is followed in DeCART and MPACT, and useful numerical results are obtained. However, accuracy will be improved when the methods in subsection 3.1.2 are adopted. The methods from this section are using asymptotic lattice-diffusion theory, using an Eddington factor, or preserving some desired transport behavior.

The accuracy of the 2D/1D solution depends strongly on the use of the correct diffusion coefficient in the approximate axial derivative term. For problems that are classically diffusive, such as the ones tested here in Chapter 4, our numerical results show that the standard diffusion coefficient $D = 1/3\Sigma_{tr}$ is correct. However, for a reactor lattice, where classic diffusion theory is not valid (because the angular depen-

dence of the neutron flux is much more complicated than linear), the classic formula $D = 1/3\Sigma_{tr}$ (or a homogenized version of this formula) is not justified theoretically. Fortunately, for lattice problems, a systematic asymptotic theory does predict an axial diffusion coefficient [18, 19], and we recommend that this be implemented and tested in MPACT.

6.1.2 Shape Functions

In this thesis, we presented the two most very basic shape functions possible: "flat" and "scalar flux" weighted. It is possible to formulate more detailed and accurate shape functions. For instance, a smaller subset of discrete angles could be used to define a shape function, or a shape function could be defined using spherical harmonic expansions of the coarse and fine grid angular fluxes in the numerator and denominator of the fundamental shape function. The systematic asymptotic theory for lattice problems [18, 19] also predicts an appropriate lattice diffusion shape function.

6.1.3 Alternate Axial Solvers

In this thesis, we considered finite difference and nodal axial diffusion. Both of these approximations agree with the underlying 2D/1D equation. Alternate, more accurate axial solvers exist in MPACT, such as 1D nodal P_3 and S_N solvers. The underlying integrodifferential equation when using these methods with the axial leakage methods presented here is unclear and may not exist. In order to state an underlying 2D/1D equation when using these methods, it may be a *requirement* to use a more accurate axial leakage approximation.

6.1.4 Alternate Leakage Splitting

In Chapter 4, we discussed the concept of axial leakage splitting to preserve the flat-source region-wise positivity of the source. In Chapter 5, we observed that its inclusion also seemed to improve the pin power distribution by working as an implicit

shape function. This suggests that the inclusion of the transverse axial leakage as an absorption term, rather than a source term, could produce more accurate solutions than the methodologies investigated here. The difficulty of this approach would be the possibility of negative, effective absorption cross sections which would cause the angular flux of the 2D sweep to grow, rather than decay, exponentially along the ray sweep.

6.2 Final Thoughts

In conclusion: we have presented in this thesis the beginning of a mathematical theory for the 2D/1D methodology in DeCART and MPACT, so that this methodology can be systematically developed and improved for practical reactor core problems. This lays the ground work for more advanced 2D/1D approximations to be made with a solid mathematical basis. We have presented results of 2D/1D and 3D calculations for some geometrically simple problems, showing that (i) the 2D/1D solutions exist and are more accurate than standard diffusion, and (ii) the iterative method is stable and behaves as predicted by the Fourier analysis. We have also shown that the method performs admirably when applied to benchmark reactor problems. From this, we look favorably on the 2D/1D methodology, as a fast, accurate tool for the numerical simulation of reactor physics problems.

Bibliography

[1] N.Z. Cho, G.S. Lee, and C.J. Park, "Fusion Method of Characteristics and Nodal Method for 3D Whole Core Transport Calculation," *Trans. Am. Nucl. Soc.*, **86**, pp. 322-324 (2002).

[2] J.Y. Cho, H.G. Joo, K.S. Kim, and S.Q. Zee, "Three-Dimensional Heterogeneous Whole Core Transport Calculation Employing Planar MOC Solutions," *Trans. Am. Nucl. Soc.*, **87**, pp. 234-236 (2002).

[3] N.Z. Cho, G.S. Lee, and C.J. Park, "Refinement of the 2-D/1-D Fusion Method for 3-D Whole Core Transport Calculation," *Trans Am. Nucl. Soc.*, **87**, pp. 417-420 (2002).

[4] N.Z. Cho, G.S. Lee, and C.J. Park, "A Fusion Technique of 2-D/1-D Methods for Three-Dimensional Whole-Core Transport Calculations," *Proc. Korean Nucl. Soc.*, Kwangju, Korea (May, 2002).

[5] N.Z. Cho, G.S. Lee, and C.J. Park, "Partial Current-Based CMFD Acceleration of the 2D/1D Fusion Method for 3D Whole Core Transport Calculations," *Trans. Am. Nucl. Soc.*, **88**, pp. 594-596 (2003).

[6] H.G. Joo, J.Y. Cho, K.S. Kim, C.C. Lee, and S.Q. Zee, "Methods and Performance of a Three-Dimensional Whole Core Transport Code DeCART," *Proc. PHYSOR 2004*, Chicago, April 25-29, 2004, American Nuclear Society, CD-ROM (2004).

[7] S. Kosaka and T. Takeda, "Verification of 3D Heterogeneous Core Transport Calculation Using Non-linear Iteration Technique," *J. Nucl. Sci. Tech.*, **41**, No. 6, pp. 645-654 (2004).

[8] N.Z. Cho, "Fundamentals and Recent Developments of Reactor Physics Methods," *Nucl. Eng. Tech.*, **37**, pp. 25-78 (2005).

[9] G.S. Lee and N.Z. Cho, "2D/1D Fusion Method Solutions of the Three-Dimensional Transport OECD Benchmark Problem C5G7 MOX," *Prog. Nucl. Energy*, **48**, pp. 410-423 (2006).

[10] J.Y. Cho and J.G. Joo, "Solution of the C5G7MOX Benchmark Three-Dimensional Extension Problems by the DeCART Direct Whole Core Calculation Code," *Prog. Nucl. Energy,* **48**, pp. 456-466 (2006).

[11] J.Y. Cho, K.S. Kim, C.C. Lee, S.Q. Zee, and H.G. Joo, "Axial SPN and Radial MOC Coupled Whole Core Transport Calculation," *J. Nuc. Sci. Tech.*, **44**, pp. 1156-1171 (2007).

[12] B. Kochunas, et al., "Overview of Development and Design of MPACT: Michigan Parallel Characteristics Transport Code," *Proc. M&C 2013*, Sun Valley, ID, USA, May 5-9 (2013).

[13] J. Askew, "A Characteristics Formulation of the Neutron Transport Equation in Complicated Geometries," Tech. Rep. AEEW-R-1108, United Kingdom Atomic Energy Authority (1972).

[14] M.J. Halsall, "CACTUS, A Characteristics Solution to the Neutron Transport Equations in Complicated Geometries," Tech. Rep. AEEW-R-1291, United Kingdom Atomic Energy Authority (1980).

[15] K.S. Smith, "Nodal Method Storage Reduction by Nonlinear Iteration," *Transactions of the American Nuclear Society*, **44**, 265 (1983).

[16] E.W. Larsen and B.W. Kelley, "CMFD and Coarse-Mesh DSA," *Proc. PHYSOR 2012*, Knoxville, Tennessee, April 15-20 (2012).

[17] B. Kochunas, Z. Liu, and T. Downar, "Parallel 3-D Method of Characteristics in MPACT," *Proc. M&C 2013*, Sun Valley, ID, USA, May 5-9 (2013).

[18] T.J. Trahan and E.W. Larsen, "An Asymptotic Homogenized Neutron Diffusion Approximation. I. Theory," *Proc. PHYSOR 2012*, Knoxville, TN, April 15-20 (2012).

[19] T.J. Trahan and E.W. Larsen, "An Asymptotic Homogenized Neutron Diffusion Approximation. II. Numerical Comparisons," *Proc. PHYSOR 2012*, Knoxville, TN, April 15-20 (2012).

[20] S. Stimpson, *An Azimuthal, Fourier Moment-Based Axial SN Solver for the 2D/1D Scheme* (Doctoral dissertation), University of Michigan, Ann Arbor Michigan, (2014).

[21] T. Takeda and H. Ikeda, "Final Report on the 3-D Neutron Transport Benchmarks," Tech. Rep. NEA/NEACRP/L(1990)330, Organisation for Economic Co-operation and Development Nuclear Energy Agency (1991).

[22] M.A. Smith, E.E. Lewis, and B.C. NA, "Benchmark on Deterministic Transport Calculations Without Spatial Homogenisation: A 2-D/3-D MOX Fuel Assembly Benchmark (C5G7 MOX Benchmark)," Tech. Rep. NEA/NSC/DOC(2003)16, Organisation for Economic Co-operation and Development Nuclear Energy Agency (2003).

[23] M.A. Smith, E.E. Lewis, and B.C. NA, "Benchmark on Deterministic Transport Calculations Without Spatial Homogenisation: MOX Fuel Assembly 3-D Extension Case," Tech. Rep NEA/NSC/DOC(2005)16, Organisation for Economic Co-operation and Development Nuclear Energy Agency (2005).

[24] A.T. Godfrey, "VERA Core Physics Benchmark Progression Problem Specifications (Rev. 4)," Tech. Rep. CASL-U-2012-0131-004, Oak Ridge National Laboratory, http://www.casl.gov/docs/CASL-U-2012-0131-004.pdf, (2014).

[25] Y. Liu, et al., "Resonance Self-Shielding Methodology in MPACT," *Proc. M&C 2013*, Sun Valley, ID, USA, May 5-9 (2013).